

Gutzwiller–RVB theory of high-temperature superconductivity: Results from renormalized mean-field theory and variational Monte Carlo calculations

B. Edegger , V. N. Muthukumar & C. Gros

To cite this article: B. Edegger , V. N. Muthukumar & C. Gros (2007) Gutzwiller–RVB theory of high-temperature superconductivity: Results from renormalized mean-field theory and variational Monte Carlo calculations, *Advances in Physics*, 56:6, 927-1033, DOI: [10.1080/00018730701627707](https://doi.org/10.1080/00018730701627707)

To link to this article: <https://doi.org/10.1080/00018730701627707>



Published online: 08 Oct 2007.



Submit your article to this journal [↗](#)



Article views: 809



View related articles [↗](#)



Citing articles: 123 View citing articles [↗](#)

Gutzwiller–RVB theory of high-temperature superconductivity: Results from renormalized mean-field theory and variational Monte Carlo calculations

B. EDEGGER^{*†}, V. N. MUTHUKUMAR[‡] and C. GROS[†]

[†]Institute for Theoretical Physics, Universität Frankfurt,
D-60438 Frankfurt, Germany

[‡]Department of Physics, Princeton University, Princeton, NJ 08544, USA

(Received 24 January 2007; in final form 2 July 2007)

We review the resonating valence bond (RVB) theory of high-temperature superconductivity using Gutzwiller projected wave functions that incorporate strong correlations. After a general overview of the phenomenon of high-temperature superconductivity, we discuss Anderson's RVB picture and its implementation by renormalized mean-field theory (RMFT) and variational Monte Carlo (VMC) techniques. We review RMFT and VMC results with an emphasis on recent developments in extending VMC and RMFT techniques to excited states. We compare results obtained from these methods with angle-resolved photoemission spectroscopy (ARPES) and scanning tunnelling microscopy (STM). We conclude by summarizing recent successes of this approach and discuss open problems that need to be solved for a consistent and complete description of high-temperature superconductivity using Gutzwiller projected wave functions.

	PAGE
1. Introduction	929
1.1. High-temperature superconductivity	930
1.2. A historical perspective	931
1.3. Experiments	932
1.3.1. ARPES	933
1.3.2. STM	938
1.4. Theories	939
1.4.1. Electronic models	940
1.4.2. RVB picture	940
1.4.3. Spin fluctuation models	940
1.4.4. Inhomogeneity-induced pairing	941
1.4.5. SO(5) theory	941
1.4.6. Cluster methods	941
1.4.7. Competing order	942
1.4.8. BCS–BEC crossover	942

^{*}Corresponding author. Email: gros07@itp.uni-frankfurt.de

2. RVB theories	943
2.1. The RVB state: basic ideas	943
2.1.1. RVB states in half-filled Mott–Hubbard insulators	943
2.1.2. RVB spin liquid at finite doping	945
2.2. Realizations and instabilities of the RVB state	945
2.3. Predictions of the RVB hypothesis for HTSCs	947
2.4. Transformation from the Hubbard to the t – J model	949
2.5. Implementations of the RVB concept	951
2.5.1. Gutzwiller projected wave functions	951
2.5.2. SBMFT and RVB gauge theories	952
2.5.3. The b-RVB theory	954
2.6. Variational approaches to correlated electron systems	955
2.6.1. Order parameters	955
2.6.2. Jastrow correlators	956
3. Gutzwiller approximation	957
3.1. Basic principles of the GA	957
3.1.1. Gutzwiller renormalization factors by counting arguments	958
3.1.2. Gutzwiller renormalization factors in infinite dimensions	962
3.2. GA in the canonical and the grand canonical scheme	964
3.2.1. Incorporation of a fugacity factor	964
3.2.2. Singular particle number renormalization close to half-filling	966
3.2.3. Gutzwiller renormalization factors in the canonical and the grand canonical ensemble	967
3.3. GA for partially projected states	969
3.3.1. Occupancy of the reservoir site	972
3.3.2. Renormalization of mixed hopping terms	972
3.3.3. Comparison of the GA for partially projected states with VMC calculations	974
4. RMFT: basic ideas and recent extensions	976
4.1. Overview on the RMFT method	976
4.2. Derivation of the RMFT gap equations	977
4.2.1. Derivation of the renormalized t – J Hamiltonian	978
4.2.2. Mean-field decoupling of the renormalized Hamiltonian	978
4.2.3. Solutions of the RMFT gap equations	979
4.2.4. Local SU(2) symmetry in the half-filled limit	981
4.3. RMFT for the Hubbard model and application to HTSCs	982
4.3.1. Generalized gap equations for the strong coupling limit	982
4.3.2. Results from the generalized gap equations	983
4.4. Possible extensions and further applications	987
4.4.1. Incorporation of antiferromagnetism	987
4.4.2. Applications to inhomogeneous systems	988
4.4.3. Gossamer superconductivity	989
4.4.4. Time-dependent GA	990
5. VMC calculations for HTSCs: an overview	990
5.1. Details of the VMC method	990
5.1.1. Real-space representation of the trial wave function	991
5.1.2. Implementation of the Monte Carlo simulation	992
5.2. Improvements of the trial wave function	994
5.2.1. Antiferromagnetism and flux states	995
5.2.2. Increasing the number of variational parameters	996
5.2.3. Investigation of the Pomeranchuk instability	997

5.3. Ground state properties: VMC results	999
5.3.1. Superconducting gap and order parameter	999
5.3.2. Derivation of spectral features from ground state properties	1000
6. QP states within RMFT	1003
6.1. Coherent and incoherent spectral weight	1004
6.1.1. Sum rules for the spectral weight	1004
6.1.2. Definition of coherent QP excitations	1005
6.1.3. Incoherent background of the spectral weight	1006
6.1.4. Divergent \mathbf{k} -dependent self-energy	1007
6.2. Calculation of the QP weight within RMFT	1007
6.3. QP weight for the Hubbard model in the strong coupling limit	1009
6.3.1. Non-monotonic behaviour of the QP weight at $(\pi, 0)$	1010
6.4. QP current renormalization	1011
6.5. Determining the underlying FS of strongly correlated superconductors	1014
6.5.1. Fermi versus Luttinger surface	1015
6.5.2. FS determination	1016
6.5.3. Renormalization of the FS towards perfect nesting	1017
7. QP states within the VMC scheme	1019
7.1. Direct calculation of the QP weight	1019
7.1.1. Momentum dependence of the QP weight	1020
7.1.2. Doping dependence of the mean QP weight	1022
7.2. VMC calculations for the QP energy	1023
8. Summary and outlook	1025
Acknowledgements	1027
References	1027

1. Introduction

In this paper we review developments in the use of Gutzwiller projected wave functions and the resonating valence bond (RVB) theory in the context of high-temperature superconductivity. We attempt to both review the general framework of the Gutzwiller–RVB theory comprehensively and to summarize several recent results in this field. Although many of these results were indeed motivated by the phenomenon of high-temperature superconductivity and the rich phase diagram of these compounds, it is not our intention to review high-temperature superconductivity *per se*. Nonetheless, it is well nigh impossible, if not meaningless, to attempt to write a review of this nature without discussing certain key experimental results. Our choice in this matter is dictated by the fact that most techniques used in the study of Gutzwiller projected wave functions address the calculation of single particle spectral features. Consequently, after discussing some basic facts and a historical perspective of the Gutzwiller–RVB concept, we present an overview of experimental results from angle-resolved photoemission spectroscopy (ARPES) and scanning tunneling microscopy (STM) within this introductory section. We also discuss briefly a few alternative theories based on repulsive electronic models, to illustrate the complexity of the subject.

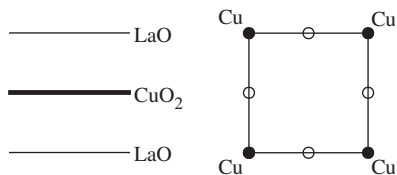


Figure 1. Crystal structure of La_2CuO_4 : (a) layer structure along the c -axis; (b) structure of the CuO_2 plane. From [2].

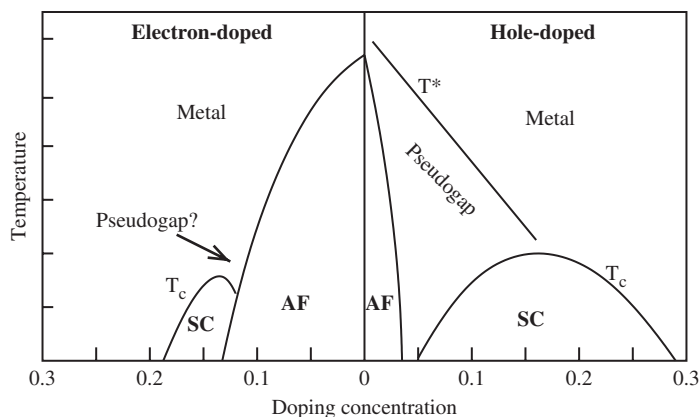


Figure 2. Generic phase diagram for the HTSCs (AF, antiferromagnetic region; SC, superconducting phase). The temperature below which superconductivity (a pseudogap) is observed is denoted by T_c (T^*). T^* is possibly a crossover temperature, although some experiments (cf. figure 7) indicate a relation to a mean-field like second-order transition.

1.1. High-temperature superconductivity

Around 20 years ago Bednorz and Müller [1] discovered high-temperature superconductivity in Sr-doped La_2CuO_4 . Subsequently high-temperature superconductivity was reported in many other cuprates. These compounds have a layered structure made up of one or more copper–oxygen planes (see figure 1). It was soon realized that many of the high-temperature superconductors (HTSCs) have an insulating antiferromagnetic parent compound that becomes superconducting when doped with holes or electrons. This is fundamentally different from, say, superconductivity in alkaline metals and clearly calls for a novel mechanism.

These unusual observations stimulated an enormous amount of experimental as well as theoretical works on HTSCs, which brought about numerous new insights into these fascinating compounds. The d -wave nature of the superconducting pairs [3] as well as the generic temperature-doping phase diagram (figure 2) are now well established. On the theoretical front, several approaches successfully describe at least some of the features of HTSCs. In addition, new sophisticated numerical techniques provide us with a better understanding of the strong correlation effects that are clearly present in HTSCs. Progress in the field of high-temperature superconductivity

has also influenced many other fields in condensed matter physics greatly. Research on HTSCs has a very fruitful history and continues to broaden our knowledge of strongly correlated electron systems.

Given the numerous theories advanced to explain the phenomenon of high-temperature superconductivity [4], it is important to examine carefully the strengths and weaknesses of any given theoretical approach and its relevance to experimental observations. In this review, we examine the RVB scenario which proposes a simple, yet non-trivial wave function to describe the ground state of Mott–Hubbard superconductors, i.e. superconductors that are obtained by doping a Mott–Hubbard insulator. We discuss various theoretical calculations based on the so called Gutzwiller–RVB wave function both in the context of our work [5–10] and other recent developments.

The Gutzwiller–RVB theory provides a direct description of strongly correlated superconductors. An advantage of this approach is that the theory can be studied by a variety of approximate analytical techniques as well as numerical methods. We discuss later how the theory yields many results that are in broad agreement with various key experimental facts. However, to obtain a more complete description of HTSCs, the Gutzwiller–RVB calculations need to be extended to be able to describe finite temperature and dynamic effects. This review should provide an adequate starting point for further extensions of this method as well as phenomenological calculations of various physical quantities that are relevant to the phenomenon of high-temperature superconductivity.

1.2. *A historical perspective*

The notion of RVBs was introduced by Pauling [11, 12] in the context of the Heitler–London approximation for certain types of non-classical molecular structures. Anderson and Fazekas [13, 14] then generalized this concept to the case of frustrated magnetism of localized spin- $\frac{1}{2}$ moments. The RVB theory came to a first full bloom with the discovery of high-temperature superconductivity when Anderson [15] suggested that a RVB state naturally leads to incipient superconductivity from preformed singlet pairs in the parent insulating state.

A detailed account of the progress made after Anderson’s seminal RVB proposal is presented in this review in subsequent sections. At this point we make a few comments regarding the general lines of development of the theory.

The core of the RVB concept is variational in nature; the RVB state may be regarded as an unstable fixed point leading to various instabilities, such as antiferromagnetic order, superconductivity, etc., very much like the Fermi-liquid state. However, in contrast to Fermi-liquid theory, there is no simple Hamiltonian known for which the RVB states discussed in this review are exact solutions. For this reason, the theory developed historically along several complementary lines. The first is the quantification of the variational approach by means of the variational Monte Carlo (VMC) method. This approach was initially hampered by the problem of implementing the numerical evaluation of a general RVB wave function algorithmically [16]. However, when this problem was solved [17], the method evolved quickly into a standard numerical technique.

Very early on it was realized [18], that essential aspects of the RVB concept could be formulated within a slave-boson approach, which led to the development of gauge theories for strongly correlated electronic systems in general, and high-temperature superconductivity in particular. This line of thought has been reviewed comprehensively by Lee *et al.* [19].

The superconducting state is an ordered state and this statement applies also to the case of the HTSCs. Where there is an order parameter, there is a mean field and it was felt early on that a suitable mean-field theory should be possible when formulated in the correct Hilbert space, using the appropriate order parameters. This line of thought led to the development of the renormalized mean-field theory (RMFT) [20]. This theory plays a prominent role in this review, as it allows for qualitative analytical predictions and, in some cases, also for quantitative evaluations of experimentally accessible response functions.

There is a certain historical oddity concerning the development of the RVB concept and of the theory. After an initial flurry, there was relatively little activity in the 1990s and the Gutzwiller–RVB approach returned to the centre of scientific interest only in the last decade with the evaluation of several new response functions [21], allowing for a detailed comparison with the (then) newly available experimental results. In retrospect, is not quite clear why this particular approach lay idle for nearly a decade. It is tempting to speculate that perhaps the concept was too successful initially, predicting *d*-wave superconductivity in the cuprates at a time when available experimental results favoured an *s*-wave.

1.3. Experiments

The discovery of high-temperature superconductivity stimulated the development of several new experimental techniques. Here, we mention some key experimental facts concerning the HTSCs and refer the reader to more detailed summaries of experimental results, available in the literature [2, 3, 19, 22–24].

An early and significant result was the realization that HTSCs are doped Mott insulators, as shown in the generic temperature-doping phase diagram (see figure 2). The figure shows the antiferromagnetic phase in the undoped (half-filled[†]) compound with a Neel temperature of about $T_N \approx 300$ K. Upon doping, antiferromagnetism is suppressed and superconductivity emerges. The behaviour of T_c with doping exhibits a characteristic ‘dome’. While electron- and hole-doped HTSCs share many common features, they do exhibit some significant differences, e.g. the antiferromagnetic region persists to much higher doping levels for electron-doped cuprates.

We restrict our attention to the hole-doped compounds, partly because they are better characterized and more extensively investigated, and also because the hole-doped HTSCs exhibit a so-called pseudogap phase (with a partially gapped excitation spectrum) above the superconducting dome. The onset temperature of

[†]The copper ion is in a d^9 configuration, with a single hole in the *d*-shell per unit cell. As shown by Zhang and Rice [25] this situation corresponds to a half-filled band in an effective single-band model.

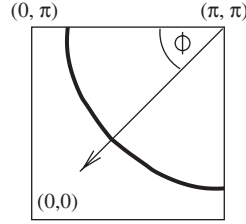


Figure 3. A schematic picture of the 2D FS (thick black line) of HTSCs in the first quadrant of the first Brillouin zone. The lattice constant a is set to unity. The ϕ defines the FS angle.

the pseudogap decreases linearly with doping and disappears in the overdoped[†] regime. The origin of the pseudogap is one of the most controversial topics in the high- T_c debate. The relationship between the pseudogap and other important features such as the presence of a Nernst phase [26, 27], charge inhomogeneities [28], the neutron scattering resonance [29], marginal Fermi liquid behaviour [30] or disorder [31]. For a detailed discussion of the pseudogap problem, we refer to a recent article by Norman *et al.* [22].

We now discuss some results from ARPES and STM, because they are immediately relevant to the theoretical considerations and results presented in the later sections. These two techniques have seen significant advances in recent years and provided us with new insights into the nature of the pseudogap, superconducting gap and quasiparticles (QPs) in the superconducting state. As we show in the following sections, many features reported by these experiments can be well understood within the framework of the Gutzwiller–RVB theory.

1.3.1. ARPES. By measuring the energy and momentum of photo-electrons, ARPES provides information about the single particle spectral function, $A(\mathbf{k}, \omega)$. The latter quantity is related to the electron Green's function by $A(\mathbf{k}, \omega) = -(1/\pi)\text{Im}G(\mathbf{k}, \omega)$ (see [32]). In this subsection, we summarize some key results from ARPES that any theory of HTSCs has to address. The reader is referred to the extensive ARPES reviews by Damascelli *et al.* [23] and Campuzano *et al.* [24] for a discussion on experimental detail.

In figure 3 we give a schematic illustration of the two-dimensional (2D) Fermi surface (FS) of HTSCs in the first quadrant of the first Brillouin zone. It can be obtained by ARPES scans along different angles ϕ . The FS for each ϕ is then determined in general (but not in the underdoped region [9]) by looking at the minimum energy of the photoelectron along this direction in momentum space. A typical energy distribution curve (EDC), i.e. photoemission intensity as a function of energy at fixed momentum, from an ARPES experiment is shown in figure 4. The figure shows the photoemission intensity at the $(\pi, 0)$ point of a photoelectron in the

[†]The superconducting phase is often divided into an optimal doped (doping level with highest T_c), an overdoped (doping level higher than optimal doped) and an underdoped (doping level lower than optimal doped) regime.

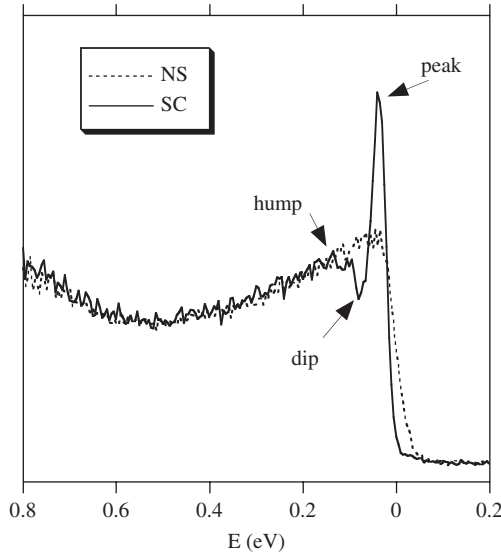


Figure 4. EDC at fixed momentum $\mathbf{k} = (\pi, 0)$ for an overdoped (87 K) $\text{Bi}_2\text{Sr}_2\text{CaCu}_2\text{O}_{8+\delta}$ (Bi2212) sample in the normal state (NS) and superconducting state (SC). From [2].

superconducting state ($T \ll T_c$) and in the normal state ($T_c > T$). In the superconducting state, one sees the characteristic peak–dip–hump structure; the peak can be associated with a coherent QP. Above T_c , coherence is lost and the sharp peak disappears.

In the early years following the discovery of high-temperature superconductivity, it was unclear whether the pairing symmetry was isotropic (s -wave like), as in conventional phonon-mediated superconductors, or anisotropic. Later experiments have consistently confirmed an anisotropic gap with d -wave symmetry [3]. The angular dependence of the gap function is nicely seen in ARPES measurements on HTSCs (figure 5), which accurately determine the superconducting gap $|\Delta_{\mathbf{k}}|$ at the FS. As illustrated in figure 5 for a $\text{Bi}_2\text{Sr}_2\text{CaCu}_2\text{O}_{8+\delta}$ (Bi2212) sample, the gap vanishes for $\phi = 45^\circ$. This direction is often referred to as the ‘nodal direction’, the point at the FS is then called the ‘nodal point’ or ‘Fermi point’. In contrast, the gap becomes maximal for $\phi = 0^\circ, 90^\circ$, i.e. at the ‘anti-nodal point’.

Another feature well established by ARPES is the doping dependence of the superconducting gap and the opening of the pseudogap at a temperature $T^* > T_c$. Unlike conventional superconductors, HTSCs exhibit a strong deviation from the Bardeen–Cooper–Shrieffer (BCS) ratio[†] of $2\Delta/(k_B T_c) \approx 4.3$ for superconductors with a d -wave gap function. In HTSCs, this ratio is strongly doping dependent and becomes quite large for underdoped samples, where the transition temperature T_c decreases, while the magnitude of the superconducting gap increases.

[†]The weak coupling BCS ratio for s -wave superconductors, $2\Delta/(k_B T_c) \approx 3.5$.

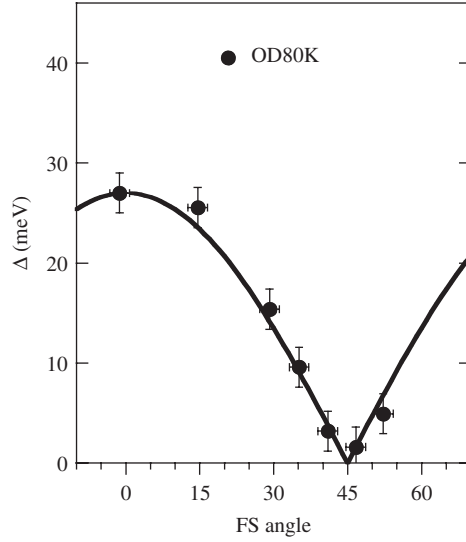


Figure 5. Momentum dependence of the spectral gap Δ at the FS in the superconducting state of an overdoped Bi2212 sample from ARPES. The black line is a fit to the data. For a definition of the FS angle ϕ see figure 3. Reprinted with permission from [33] © 1999 by the American Physical Society.

As illustrated in figure 6 for a Bi2212 sample, the binding energy of the peak at $(\pi, 0)$, i.e. the superconducting gap[†], increases linearly (with doping) while approaching the half-filled limit. Interestingly, the opening of the pseudogap at temperature T^* seems to be related to the magnitude of the gap. The modified ratio $2\Delta/(k_B T^*)$ is a constant for HTSCs at all doping levels and the constant is in agreement with the BCS ratio, 4.3 (see figure 7), with T_c substituted by T^* . This experimental result is as a remarkable confirmation of early predictions from Gutzwiller–RVB theory, as we discuss in further detail in latter sections. figure 6 also reveals that the hump feature (see the EDC in figure 4) scales with the binding energy of the peak at $(\pi, 0)$.

An additional doping-dependent feature extracted from ARPES data is the spectral weight of the coherent QP peak. Feng *et al.* [37] defined a superconducting peak ratio (SPR) by comparing the area under the coherent peak with that of the total spectral weight. Figure 8 depicts EDCs at several doping levels together with the computed SPR as a function of doping. The QP spectral weight strongly decreases with decreasing doping and finally vanishes [37, 38]. Such a behaviour is well understood by invoking the projected nature of the superconducting state as we discuss in the following sections.

As ARPES is both a momentum and energy resolved probe, it allows for the measurement of the dispersion of the coherent peak. Here, we concentrate on the nodal point, where the excitations are gapless even in the superconducting state, owing to the d -wave symmetry of the gap. The dispersion around the nodal point

[†]When speaking about (the magnitude of) the superconducting gap Δ in a d -wave state without specifying the momentum \mathbf{k} , we mean the size of the gap $|\Delta_{\mathbf{k}}|$ at $\mathbf{k} = (\pi, 0)$.

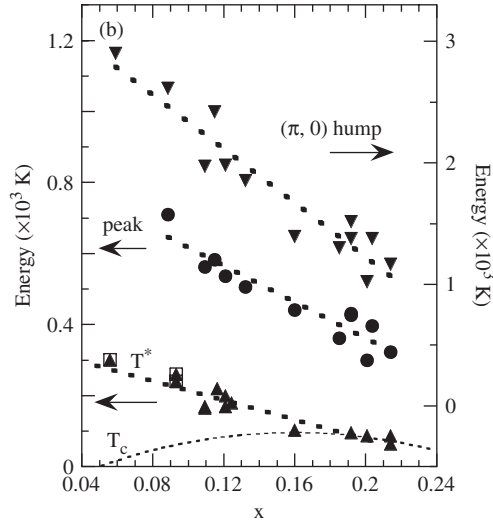


Figure 6. Doping dependence of T^* (the onset of the pseudogap, compare with figure 2) and of the peak and hump binding energies in the superconducting state (see figure 4). The empirical relation between T_c and doping x is given by $T_c/T_c^{\max} = 1 - 82.6(x - 0.16)^2$ with $T_c^{\max} 95$ K. Data for Bi2212, from [34].

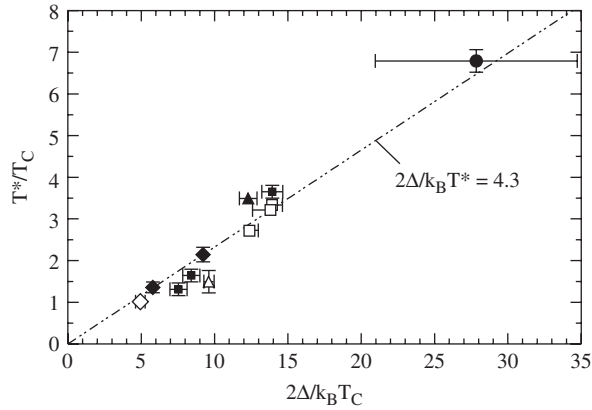


Figure 7. T^*/T_c versus $2\Delta/(k_B T_c)$ for various cuprates compared with the mean-field relation, $2\Delta/(k_B T^*) = 4.3$, valid for d -wave superconductivity [35], where T^* replaces T_c . Reprinted with permission from [36] © 2001 by the American Physical Society.

is well approximated by Dirac cones, whose shape is characterized by two velocities, v_F and v_Δ . The Fermi velocity v_F is determined by the slope of the dispersion along the nodal direction at the nodal point, whereas the gap velocity v_Δ is defined by the slope of the ‘dispersion’ perpendicular to the nodal direction at the nodal point. As all other \mathbf{k} -points are gapped, the shape of the Dirac-like dispersion around the nodal point is of particular importance for the description of any effect depending on low-lying excitations.

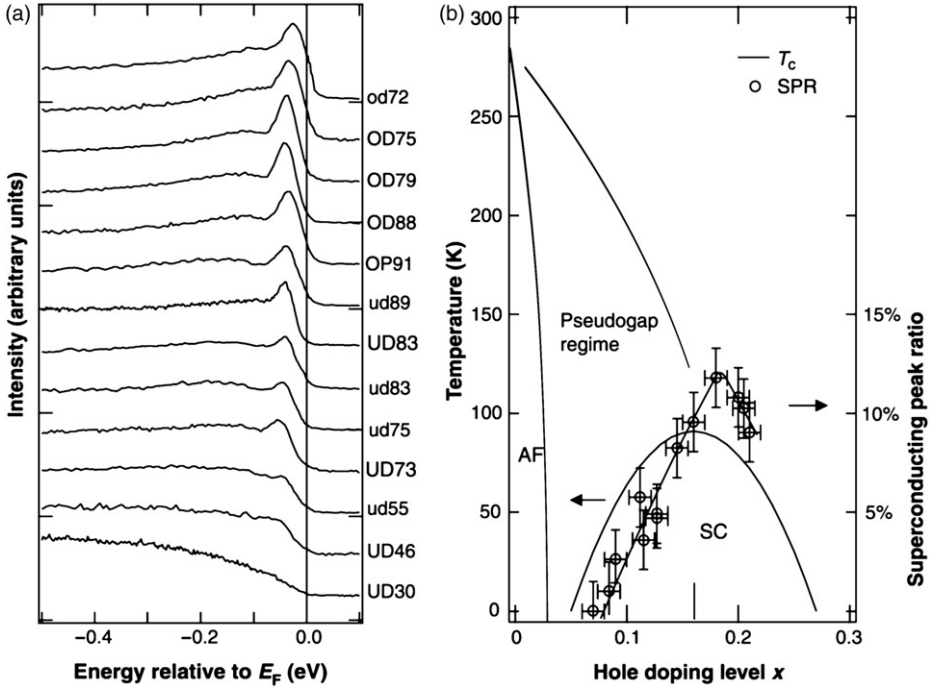


Figure 8. (a) Doping dependence of the superconducting state spectra in Bi2212 at $(\pi, 0)$ taken at $T \ll T_c$. The doping level is decreasing from the top curve downwards. Samples are denoted by OD (overdoped), OP (optimal doped) and UD (underdoped), together with their T_c in Kelvin, e.g. OD75 denotes an overdoped sample with $T_c = 75$ K. (b) The doping dependence of SPR (spectral weight of coherent peak with respect to the total spectral weight) is plotted over a typical Bi2212 phase diagram for the spectra in (a). AF, antiferromagnetic regime; SC, superconducting regime. Reprinted with permission from [37] © 2000 by the AAAS.

Figure 9(a) illustrates the slope of the dispersion along the nodal direction for $\text{La}_{2-x}\text{Sr}_x\text{CuO}_4$ (LSCO) samples at various dopings. The ARPES data reveals a significant splitting in high-energy and low-energy parts, whereas the low-energy part corresponds to the Fermi velocity v_F . Within ARPES data (see figure 9(a)) the Fermi velocity v_F is only weakly doping dependent. ARPES can also determine the gap velocity v_Δ by looking at the spectral gap along the FS as in figure 5. Together with the v_F , the v_Δ determines the shape of the Dirac cones, which, according to ARPES, is quite anisotropic ($v_F/v_\Delta \approx 20$ around optimal doping) [33]. This result is confirmed by thermal conductivity measurements [40], that yield similar asymmetries as in ARPES. Another generic feature of HTSCs is a kink seen in the ARPES nodal dispersion as shown in figure 9(a). This kink also effects the scattering rate of the coherent QPs as measured by the momentum distribution curves (MDCs) width, see figure 9(b) and [23, 24].

An interesting feature seen in ARPES is the shrinking of the FS when the pseudogap opens at T^* . With decreasing temperature, more and more states around the antinodal region become gapped and the FS becomes continuously smaller.

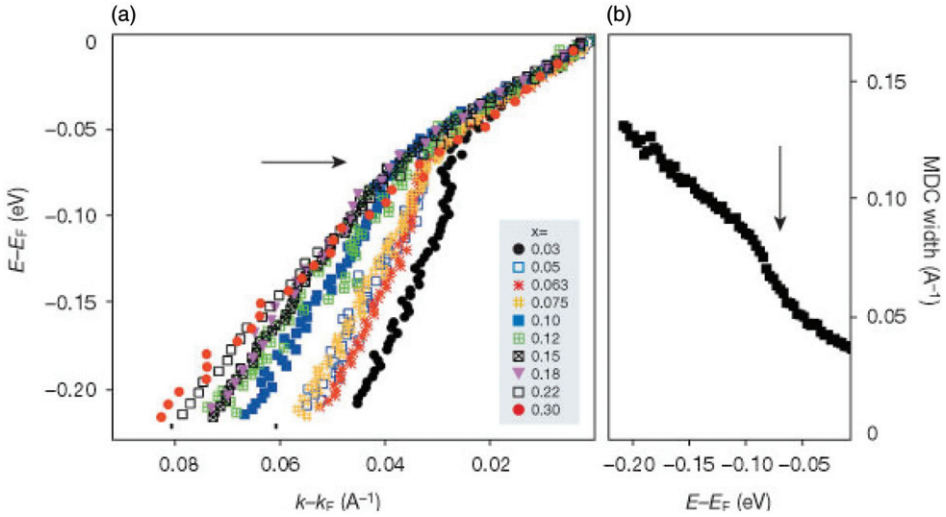


Figure 9. Electron dynamics in the $\text{La}_{2-x}\text{Sr}_x\text{CuO}_4$ (LSCO) system. (a) Dispersion energy, E , as a function of momentum, \mathbf{k} , of LSCO samples with various dopings measured along the nodal direction. The arrow indicates the position of the kink that separates the dispersion into high-energy and low-energy parts with different slopes. The Fermi energy and Fermi momentum are denoted by E_F and \mathbf{k}_F , respectively. (b) Scattering rate as measured by MDC width of the LSCO ($x = 0.063$). Reprinted with permission from [39] © 2003 Nature Publishing Group.

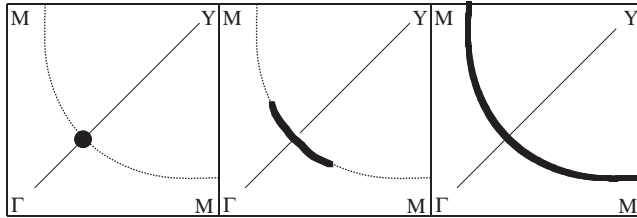


Figure 10. Schematic illustration of the temperature evolution of the FS in underdoped Cuprates as observed by ARPES. The d -wave node below T_c (left panel) becomes a gapless arc above T_c (middle panel), which expands with increasing T to form the full FS at T^* (right panel). From [41].

Instead of a full FS, the pseudogapped state exhibits Fermi arcs [41–45], that finally collapse to single nodal Fermi points at $T = T_c$ (see figure 10). For a detailed discussion on this and related ARPES observations, we refer the reader to the ARPES reviews in the literature [23, 24].

1.3.2. STM. In contrast to ARPES, STM is a momentum integrated probe. However, its ability to measure the local density of occupied as well as unoccupied states with a high-energy resolution gives very valuable insights into HTSCs. An example for a STM study of Bismuth-based HTSCs is shown in figure 11. The data

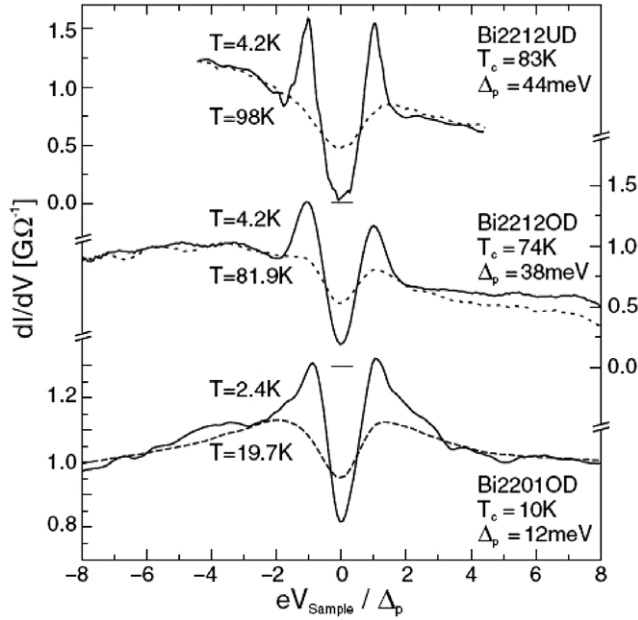


Figure 11. STM data for underdoped (UD) and overdoped (OD) Bi2212, and overdoped Bi2201; comparison between the pseudogap (dashed curve, $T > T_c$) and the gap in the superconducting state (solid curve, $T < T_c$). The underdoped data exhibits a significant asymmetry between positive and negative bias voltages. For an analysis of the temperature-dependent pseudogap, see figure 7. Reprinted with permission from [36] © 2001 by the American Physical Society.

in the superconducting state reveals a density of states, which is characteristic of a d -wave gap, i.e. there is no full gap in contrast to s -wave superconductivity. In the pseudogap state (above T_c) the density of states is still suppressed around $\omega = 0$ (zero voltage), however, the characteristic peaks disappear. Another interesting feature seen in figure 11 is the striking asymmetry between positive and negative voltages, which becomes more pronounced for the underdoped sample. A detailed explanation for this generic property of HTSCs is given in the following sections.

A key advantage of STM is the possibility to obtain spatial information. For example, STM experiments allow for the investigation of local electronic structure around impurities [46–48] and around vortex cores [49–51] in the superconducting state. Other interesting features recently reported by STM include a checkerboard-like charge density wave [52, 53] and the existence of spatial variations in the superconducting gaps [54]. The origin of these observations is currently being debated intensely.

1.4. Theories

It is beyond the scope of this article to provide an overview of various theories of high-temperature superconductivity that have been put forward in the literature. Owing to the enormous complexity of the experimentally observed features, it is

not easy to agree on the key ingredients necessary for setting up a comprehensive theory. Furthermore, the decision to trust new experimental results is often difficult, because the sample quality, experimental resolution and the way the data is extracted are often not completely clear. Not surprisingly perhaps, these circumstances have allowed for diverse theoretical approaches, motivated by distinct aspects of the HTSCs. In the following, we summarize a few theoretical approaches where the proximity of a superconducting phase to a Mott insulator and antiferromagnetism play important roles.

1.4.1. Electronic models. To find an appropriate microscopic reference model is the first step in formulating any theory. Such a model should be simple enough to be treated adequately, but should also be complex enough to explain the relevant properties. In the case of the HTSCs, it is widely accepted that strong correlations in the 2D layers play an essential role. The copper–oxygen layers are appropriately described by a three-band Hubbard model, which includes the Cu $d_{x^2-y^2}$ -orbital and the two O p -orbitals [55, 56]. Its simplified version is a one-band Hubbard model[†], where each site corresponds to a copper orbital with repulsive on-site interaction between electrons [25]. The derivation of this model Hamiltonian can be found in the reviews of Lee *et al.* [19] and Dagotto [57].

1.4.2. RVB picture. Soon after the discovery of high T_c superconductivity, Anderson [15] suggested the concept of a RVB state as relevant for the HTSCs. In this picture, the half-filled Hubbard model is a Mott insulator with one electron per site. The charged states, doublons and holons, form bound charge-neutral excitations in the Mott insulating state and lead to the vanishing of electrical conductivity. Equivalently one can talk of virtual hopping causing a superexchange interaction J between the electrons at the copper sites. Therefore, the half-filled systems can be viewed as Heisenberg antiferromagnets with a coupling constant J .

Anderson proposed that upon doping quantum fluctuations melt the antiferromagnetic Neel lattice and yield a spin liquid ground state (denoted as the RVB state) in which the magnetic singlet pairs of the insulator become the charged superconducting pairs. We show in the following sections that the RVB picture provides a natural explanation for several key features of the HTSCs such as the d -wave pairing symmetry, the shape of the superconducting dome, the existence of a pseudogap phase, the strong deviations from the BCS ratio and the singular \mathbf{k} -dependence of the one-particle self-energy when approaching half-filling.

1.4.3. Spin fluctuation models. While the RVB idea approaches the problem from the strong coupling limit, i.e. large on-site electron repulsion U , spin fluctuation models[‡] start from the weak coupling (small U) limit. The technique extends the Hartree–Fock random phase approximation and leads to a pairing state with d -wave symmetry. Within this picture, superconductivity is mediated by the exchange of antiferromagnetic spin fluctuations.

[†]Henceforth we refer to the one-band Hubbard model by the phrase ‘Hubbard model’.

[‡]For more details we refer the interested reader to the review articles by Moriya and Ueda [58], Yanase *et al.* [59] and Chubukov *et al.* [60].

Weak-coupling approaches such as spin fluctuation models essentially remain within the context of Landau theory of Fermi liquids for which the QP renormalization is $Z = m/m^*$, when the self-energy is not strongly \mathbf{k} -dependent. Here, $m^* \sim v_F^{-1}$ and m is the bare band mass. The Fermi liquid relation $Z \sim v_F$, however, is difficult to reconcile with experimental results for the HTSCs, as $Z \rightarrow 0$ and $v_F \rightarrow \text{constant}$ for doping $x \rightarrow 0$, as we discuss in more detail in section 6.1.4.

1.4.4. Inhomogeneity-induced pairing. Within this class of theories, the proximity of high-temperature superconductivity to a Mott insulator plays an important role. It is postulated that the superconducting pairing is closely connected to a spontaneous tendency of the doped Mott insulator to phase-separate into hole-rich and hole-poor regions at low doping. The repulsive interaction could then lead to a form of local superconductivity on certain mesoscale structures, ‘stripes’. Calculations show that the strength of the pairing tendency decreases as the size of the structures increases. The viewpoint of the theory is as follows. Below a critical temperature, the fluctuating mesoscale structures condense into a global phase-ordered superconducting state. Such a condensation would be facilitated if the system were more homogeneous, however, more homogeneity leads to larger mesoscale structures and thus weaker pairing. Therefore, the optimal T_c is obtained at an optimal inhomogeneity, where mesoscale structures are large enough to facilitate phase coherence, but also small enough to induce enough pairing. Within the phase-separation scenario spontaneous inhomogeneities tend to increase even in clean systems when approaching half-filling. In this framework, the pseudogap in the underdoped regime can be understood as a phase that is too granular to obtain phase coherence, but has strong local pairing surviving above T_c . These ideas are reviewed in detail by Kivelson and collaborators [28, 61, 62].

1.4.5. SO(5) theory. Motivated by the vicinity of antiferromagnetism and superconductivity in the phase diagram of the HTSCs, the SO(5) theory [63] attempts to unify these collective states of matter by a symmetry principle. In the SO(5) picture, the 5 stands for the five order parameters used to set up the theory; three degrees of freedom for antiferromagnetic state (N_x , N_y , N_z) and two degrees of freedom for the superconducting state (real and imaginary parts of the superconducting order parameter). The theory aims to describe the phase diagram of HTSCs with a single low-energy effective model. A so-called projected SO(5) theory has been proposed to incorporate strong correlation effects. Several studies have also examined the microscopic basis for the SO(5) theory (see the review by Demler *et al.* [63]).

1.4.6. Cluster methods. Although numerical methods such as Lanczos (exact diagonalization) and quantum Monte Carlo have been very popular [57], they are limited by the (small) cluster size. All statements concerning the thermodynamic limit become imprecise owing to significant finite size effects. The ‘quantum cluster’ method which aims to mitigate finite size effects in numerical methods, has been used by several groups to study strongly correlated electronic systems. These methods treat correlations within a single finite size cluster explicitly. Correlations at longer length scales are treated either perturbatively or within a mean-field

approximation [64]. In recent years, this method has been used in several studies to extract the ground state properties of the Hubbard model. They reproduce several features of the cuprate phase diagram and report d -wave pairing in the Hubbard model. However, even these sophisticated numerical methods are not accurate enough to determine the ground state of the Hubbard model unambiguously.

1.4.7. Competing order. In most of the theories outlined above, the pseudogap phase is characterized by the existence of preformed pairs. Hence, there are two relevant temperature scales in the underdoped regime. Pairs form at a (higher) temperature T^* , and the onset of phase coherence at T_c leads to superconductivity. However, there are other theories that take the opposing point of view; namely, the pseudogap and superconductivity are two phases that compete with each other. In these scenarios, the pseudogap is characterized by another order parameter, e.g. given by an orbital current state [65] or a d -density wave [66]. Thus, the pseudogap suppresses superconductivity in the underdoped regime, and can also partially survive in the superconducting state. These approaches predict that the pseudogap line ends in a quantum critical point inside the superconducting dome. These two scenarios are contrasted in figure 12.

1.4.8. BCS–BEC crossover. In this picture, the pseudogap is explained by a crossover from BCS to Bose–Einstein condensation (BEC) [67, 68]. While in the BCS limit the fermionic electrons condensate to a superconducting pair state, the BEC limit describes the condensation of already existing pairs. In the crossover regime, one expects a behaviour very similar to that observed in the pseudogap of HTSCs; the formation of pairs with a corresponding excitation gap occurs at a temperature T^* and the pairs condense at a lower temperature $T_c < T^*$. It is interesting to note that the physics behind this idea can be described by a generalization of the BCS ground state wave function, $|\Psi_0\rangle$, [68]. It is unclear, however, how to incorporate the anti-ferromagnetic Mott–Hubbard insulating state close to half-filling within a BCS–BEC crossover scenario.

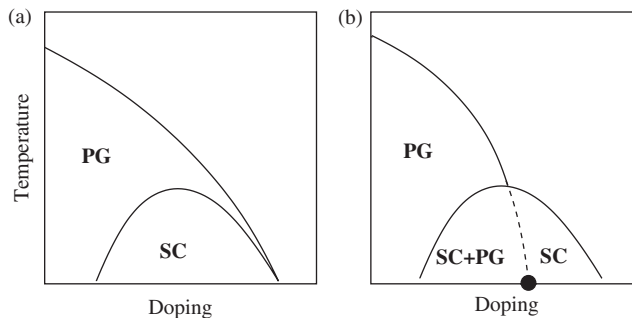


Figure 12. Two proposed theoretical phase diagrams for the cuprates. (a) RVB picture. (b) Competing order scenario: the pseudogap (PG) ends in a quantum critical point (black dot); the pseudogap and superconducting state (SC) can coexist (SC+PG).

2. RVB theories

The RVB state describes a liquid of spin singlets and was proposed originally as a variational ground state of the spin $S = \frac{1}{2}$ Heisenberg model (which describes the low-energy physics of the Hubbard model at half-filling). Anderson originally proposed that the magnetic singlets of the RVB liquid become mobile when the system is doped and form charged superconducting pairs. As we discuss in this section, this idea has led to a consistent theoretical framework to describe superconductivity in the proximity of a Mott transition. In this section, we discuss possible realizations of RVB superconductors along with the predictions of the theory. We also give an outlook on the implementations of the RVB picture by Gutzwiller projected wave functions, slave-boson mean-field theory (SBMFT) and the bosonic RVB (b-RVB) approach.

2.1. The RVB state: basic ideas

Within the RVB picture, strong electron correlations are essential for superconductivity in the cuprates. The Hubbard model is viewed as an appropriate microscopic basis and the corresponding many-body Hamiltonian is given by

$$H = - \sum_{\langle ij \rangle, \sigma} t_{ij} (c_{i\sigma}^\dagger c_{j\sigma} + c_{j\sigma}^\dagger c_{i\sigma}) + U \sum_i n_{i\uparrow} n_{i\downarrow}, \quad (1)$$

where c_i^\dagger creates and c_i annihilates an electron on site i . The hopping integrals, t_{ij} , connect sites i and j . We restrict our attention to nearest-neighbour hopping t for the moment and also discuss the influence of additional hopping terms subsequently. The operator $n_{i\sigma} \equiv c_{i\sigma}^\dagger c_{i\sigma}$ denotes the local density of spin $\sigma = \downarrow, \uparrow$ on site i . We consider an on-site repulsion $U \gg t$, i.e. we work in the strong coupling limit, which is a reasonable assumption for the HTSCs.

2.1.1. RVB states in half-filled Mott–Hubbard insulators. Let us first consider the half-filled case. As U is much larger than t the mean site occupancy is close to charge neutrality, namely one. It costs energy U for an electron to hop to a neighbouring site. This potential energy is much higher than the energy the electron can gain by the kinetic process. Thus, the motion of electrons is frozen and the half-filled lattice becomes a Mott–Hubbard insulator. However, there are virtual hopping processes, where an electron hops to its neighbouring site, builds a virtual doubly occupied site and hops back to the empty site. Such virtual hoppings lower the energy by an amount of the order $J = 4t^2/U$. The Pauli exclusion principle allows double occupancy only for electrons with opposite spin (see figure 13). Thus, virtual hopping favours antiparallel spins of neighbouring electrons and we obtain an effective antiferromagnetic Heisenberg Hamiltonian,

$$H = J \sum_{\langle ij \rangle} \mathbf{S}_i \cdot \mathbf{S}_j, \quad J > 0, \quad (2)$$

with an antiferromagnetic exchange constant $J = 4t^2/U$, the spin-operator \mathbf{S}_i on site i and $\langle ij \rangle$ denoting a sum over nearest-neighbour sites. At the level of mean-field theory, i.e. treating the spins semiclassically, the 2D Heisenberg model on a square lattice has an antiferromagnetic Neel ground state with long-range order and broken

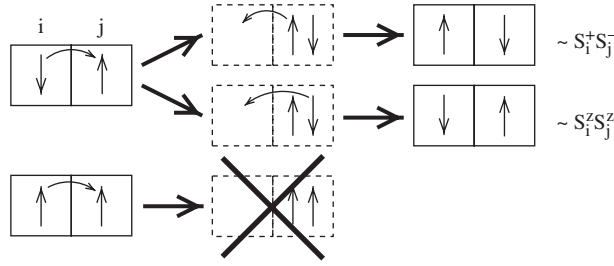


Figure 13. Hopping processes with a virtual doubly occupied site corresponding to the $S_i^z S_j^z$ and $S_i^+ S_j^-$ term of the Heisenberg Hamiltonian, respectively; virtual hopping is not possible in the case of parallel spins.

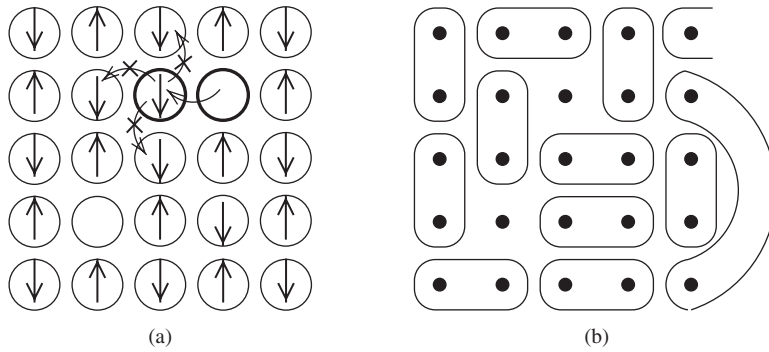


Figure 14. (a) Antiferromagnetic Neel lattice with some holes. The motion of a hole (see the bold circles) frustrates the antiferromagnetic order of the lattice. (b) Snapshot of the RVB state. A configuration of singlet pairs with some holes is shown. The RVB liquid is a linear superposition of such configurations.

symmetry (figure 14(a)). This molecular-field prediction is experimentally (by neutron scattering studies [69]) as well as theoretically (by a quantum non-linear σ model [70]) well established.

Anderson [15] suggested that a RVB liquid[†] is very close in energy to the Neel state for undoped cuprates. Instead of a Neel state with broken symmetry, a fluid of singlet pairs is proposed as the ground state, i.e. the ground state is described by a phase-coherent superposition of all possible spin singlet configurations (see figure 14(b)). For spin $S = \frac{1}{2}$, quantum fluctuations favour such singlets over classical spins with Neel order. To see this, consider a one-dimensional (1D) chain (see figure 15). In this case, a Neel state with $S_z = \pm \frac{1}{2}$ gives an energy of $-J/4$ per site. On the other hand, the ground state of two antiferromagnetic coupled spins $S = \frac{1}{2}$ is a spin singlet with $-S(S+1)J = -\frac{3}{4}J$. It follows that a chain of singlets

[†]Long before the discovery of HTSCs Anderson and Fazekas [13, 14] proposed the RVB liquid as a possible ground state for the Heisenberg model on a 2D triangular lattice.

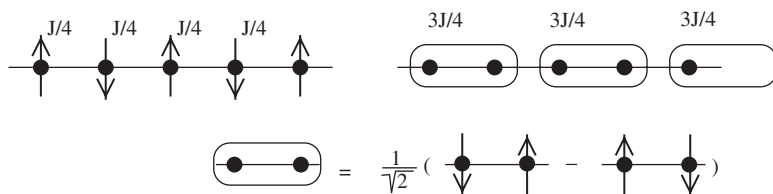


Figure 15. Neel state (left) and singlet state (right) for a 1D antiferromagnetic spin $S = \frac{1}{2}$ chain.

(see figure 15) has an energy of $-\frac{3}{8}J$ per site, much better than the Neel-ordered state. This simple variational argument shows that a singlet state is superior in one dimension. Similar considerations for the 2D Heisenberg model give the energies $-\frac{1}{2}J$ per site for the Neel lattice, the singlet state remains at $-\frac{3}{8}J$ per site. Following this reasoning we find that singlets become much worse than the Neel state in higher dimensions.

Liang *et al.* [71] showed that the singlet ‘valence bonds’ regain some of the lost antiferromagnetic exchange energy by resonating among many different singlet configurations and therefore become competitive with the Neel state in two dimensions. The resonating singlets are very similar to benzene rings with its fluctuating C–C links between a single and a double bond; an analogy that motivated the term ‘RVB’.

2.1.2. RVB spin liquid at finite doping. Though an antiferromagnetically long range ordered state is realized in the undoped insulator, the order melts with only a few percent of doped holes. To understand this, consider the example shown in figure 14(a), which shows that moving holes cause frustration in the antiferromagnetic but not the RVB state, figure 14(b). A single hole moving in the background of a Neel state was studied extensively by several authors[†], and analytical calculations showed that the coherent hole motion is strongly renormalized by the interactions with the spin excitations [72, 73]. When more holes are injected into the system, the interaction of the holes with the spin background completely destroys the antiferromagnetic Neel state and an RVB liquid (or spin liquid) state becomes superior in energy. Then the singlet pairs of the RVB liquid are charged and may condense to a superconducting ground state.

2.2. Realizations and instabilities of the RVB state

Whether there exist 2D models with an RVB ground state is still an open question. We may, however, regard the RVB state as an unstable fixpoint [74] prone to various instabilities. The situation is then analogous to that of the Fermi liquid, which becomes generically unstable in the low-temperature limit either towards superconductivity or various magnetic orderings. For instance, Lee and Feng [75] studied

[†]The single hole problem together with the corresponding literature is discussed in [19] in more detail.

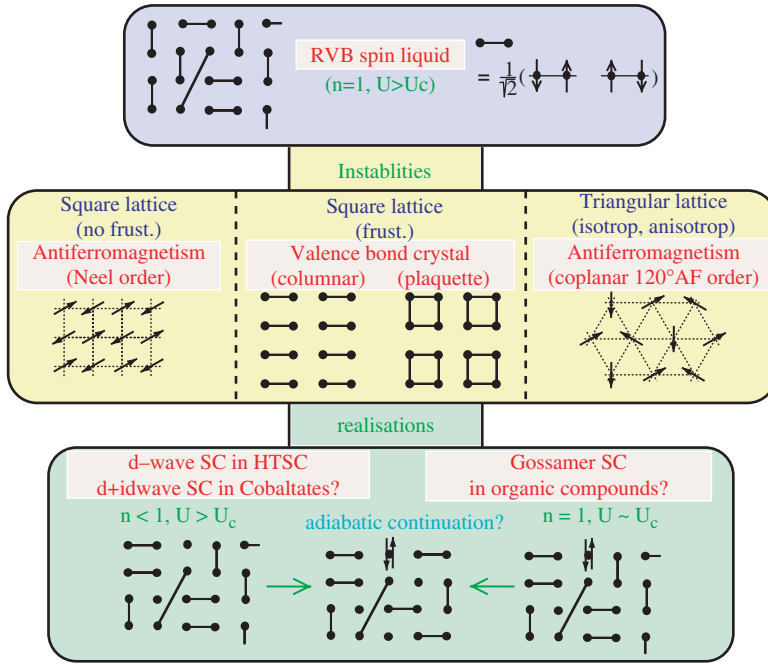


Figure 16. Schematic picture of instabilities and realizations of the RVB spin liquid state, namely of the RVB state as an unstable fixpoint. The top panel shows an RVB spin liquid at half-filling in the Mott–Hubbard insulating limit ($U > U_c$). The middle panel illustrates instabilities of the RVB liquid state in a square lattice, a frustrated square lattice and a triangular lattice in the half-filled limit. The lower panel shows realizations of the RVB liquid, which are realized at finite doping or close to the Mott–Hubbard transition ($U \sim U_c$).

numerically how a paramagnetic RVB state can be modified to become a long-range (antiferromagnetically) ordered state by introducing an additional variational parameter. In this view of antiferromagnetism, the ‘pseudo Fermi surface’ of the insulating RVB state undergoes a nesting instability to yield long-range antiferromagnetic order [76, 77]. In figure 16 we present an illustration of the concept of the RVB state as an unstable fixed point. In the following, we discuss this point further.

In addition to the square lattice with nearest-neighbour hopping, the RVB spin liquid was proposed as a ground state on a square lattice with further neighbour hopping as well as in a triangular lattice. Experiments [78] indicate that such a spin liquid state may be realized in the organic compound κ -(BEDT-TTF) $_2$ Cu $_2$ (CN) $_3$, which is an insulator in the proximity of a Mott transition. Trial spin liquid wave functions using Gutzwiller projected RVB states have been proposed in this context by Motrunich [79]. A U(1) gauge theory of the Hubbard model has also been invoked to study this system [80]. Although the simple Neel ordered state is destroyed owing to frustration in these cases, the RVB spin liquid (at $n=1$) does not become the ($T=0$) ground state, which is either a valence bond crystal state [81–85] or a coplanar 120° antiferromagnetic ordered state [86], respectively.

In addition, instabilities against inhomogeneous states such as stripes [28, 61, 62] are conceivable, and are not explicitly included in figure 16. A recent ARPES study on $\text{La}_{2-x}\text{Ba}_x\text{CuO}_4$ (see [87]), which exhibits static charge order and suppressed superconductivity around doping $x = \frac{1}{8}$, supports the idea that the superconducting RVB state can be continuously connected and unstable against a charge ordered state.

Nevertheless an RVB state can be realized if a finite number of holes are induced into the system, namely when the bosonic spin state realized at half-filling turns into a free fermionic state by the introduction of charge carriers. The hopping processes then destroy the above instabilities towards magnetic or valence bond crystal ordering and a superconducting RVB state can be stabilized. A schematic picture of this scenario is presented in figure 16.

In the case of HTSCs, holes are created by changing the doping concentration. A similar mechanism was proposed for superconductivity in the triangular lattice-based cobaltates [88, 89]. Within RMFT calculations such a triangular model would result in a $d + id$ -wave pairing state [90]. On the other hand, an RVB superconducting state at half-filling just below the Mott transition [91] was recently suggested for organic superconductors [92–94]. Here, the necessary holes could result from a finite number of conducting doubly occupied sites as illustrated in figure 16.

To summarize, an RVB superconductor could emerge by two different mechanisms starting from a Mott insulating system ($n = 1$ and $U > U_c$); either upon doping ($n \neq 1$) or from self-doping a half-filled system close to the Mott–Hubbard transition ($U \sim U_c$). In this review, we focus our attention on the former possibility, i.e. the occurrence of an RVB superconductor in a doped Mott–Hubbard insulator.

2.3. Predictions of the RVB hypothesis for HTSCs

In this subsection we discuss some predictions from RVB theory, which agree well with experimental observations. As we will show in the following sections, the arguments we present here are substantiated by more detailed microscopic calculations.

Within the RVB picture, a possible explanation for the temperature-doping phase diagram is obtained by considering two temperature scales (figure 17). The singlets of the RVB liquid form at temperature T^* , a temperature scale which decreases away from half-filling [95] owing to the presence of doped and mobile holes. Holes, on the other hand, allow for particle number fluctuations, which are fully suppressed at half-filling, and thus enhance the stability of the superconducting state against thermal fluctuations. This results in a second temperature, T_{coh} , which increases with doping and below which the superconducting carriers become phase coherent. The superconducting transition temperature T_c is therefore determined by the minimum of T^* and T_{coh} as shown in figure 17 (see also [95]).

It is evident from the above picture that a pseudogap forms for $T_{\text{coh}} < T < T^*$, i.e. for underdoped samples. In this state, although phase coherence is lost, the RVB singlet pairs still exist. Therefore, we have to break a pair to remove an electron from the copper–oxygen layers within the pseudogap regime. The resulting excitation gap manifests itself, e.g., in the c -axis conductivity or in ARPES measurements.

These schematic explanations are confirmed to a certain extent by analytical as well as numerical calculations (at zero temperature). RMFT and VMC methods show an increase of the superconducting gap, but a vanishing superconducting

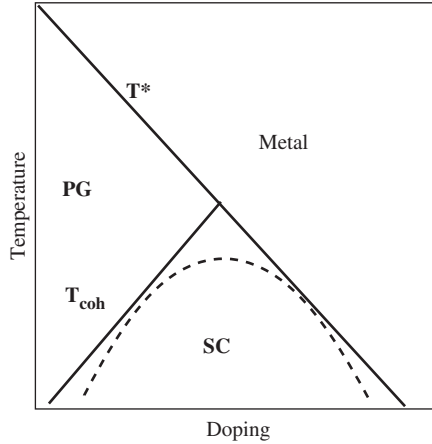


Figure 17. RVB phase diagram with singlet pairing temperature T^* and phase-coherence temperature T_{coh} (SC, superconducting state; PG, pseudogap).

order parameter, when approaching half-filling. This behaviour is in complete agreement with the $T \rightarrow 0$ observations in experiments. It also explains the strong deviation from the BCS ratio in the underdoped regime of the HTSCs, if the superconducting order parameter is related to T_c . On the other hand, the doping dependence of the onset temperature of the pseudogap T^* can be related to the magnitude of the gap at $T=0$ (in agreement with experiments, see figure 7).

Perhaps the most remarkable prediction of the RVB theory was the d -wave nature of the superconducting state. A d -wave superconducting state was predicted by RVB-based studies as early as in 1988 [17, 18, 20, 96, 97], long before the pairing symmetry was experimentally established. These early calculations also correctly described the vanishing of superconductivity above about 30% doping.

Implementing the RVB idea by projected wave functions, one finds a natural explanation of the suppression of the Drude weight and of the superfluid density in the underdoped regime as well as the particle-hole asymmetry in the density of single particle states. Further successes of the RVB theory are calculations that predict a weakly doping-dependent nodal Fermi velocity, but a strongly doping-dependent QP weight: the QP weight decreases with doping x in agreement with ARPES experiments. These effects can be understood by a decrease in the density of freely moving carriers at low doping, which results in a dispersion mainly determined by virtual hopping processes (proportional to the superexchange J). In the half-filled limit, this behaviour results in a divergence of the \mathbf{k} -dependence of the electron's self-energy, $\lim_{\omega \rightarrow 0} \partial \Sigma(\omega, \mathbf{k} = \mathbf{k}_F) / \partial \omega \sim 1/x \rightarrow \infty$, which transcends the nature of orthodox Fermi liquids. These are discussed in more detail in sections 6 and 7.

In addition to the above key features of HTSCs, RVB theory has also been successfully applied to several other phenomena such as charge density patterns [98–101], the interplay between superconductivity and antiferromagnetism [102–107], impurity problems [108–110] and vortex cores [111, 112].

In conclusion, analytical and numerical results provide significant support to the RVB concept. However, most RVB studies are restricted to zero temperature[†], making the finite-temperature picture detailed above somewhat speculative. Extending the calculations to finite temperature is an important and open problem in the theory of RVB superconductivity. A related issue is the destruction of superconductivity in the underdoped samples where we expect phase fluctuations to play an increasingly important role at low temperatures [114, 115] because particle number fluctuations are frozen in the proximity of the Mott insulator. It is presently an unsettled question as to what extent this picture is equivalent to alternative formulations, such as an increase of inhomogeneities (as in the ‘inhomogeneity-induced pairing’ picture [28, 61, 62]) or a destruction of the superfluid density owing to nodal QP excitations (see section 6.4), which were also proposed to describe the transition from the superconducting state to the pseudogap state in the underdoped regime. Further work is necessary to clarify this point.

2.4. Transformation from the Hubbard to the t - J model

The RVB scenario is based on the existence of a strong antiferromagnetic superexchange, J . The superexchange process by means of virtual hopping processes results in an effective Heisenberg Hamiltonian as discussed earlier (see figure 13). We now present a more formal and systematic derivation of a low-energy theory starting from the Hubbard Hamiltonian in the strong coupling limit ($U \gg t$). The basic idea is to make the theory ‘block diagonal’, i.e. subdivide the Hamiltonian matrix elements into processes that preserve the local number (diagonal processes) and those that do not (off-diagonal) by a unitary transform. As we are interested in the strong coupling limit, off-diagonal processes will be removed as such (high-energy) configurations are not allowed in the Hilbert space of the effective (low-energy) theory.

The unitary transformation, e^{-iS} to lowest order in t/U [116, 117] can be obtained as follows. First we assume that S is of the order $\mathcal{O}(t/U)$ and expand the transformed Hamiltonian,

$$H^{(\text{eff})} = e^{iS} H e^{-iS} = e^{iS} (\hat{T} + \hat{U}) e^{-iS} \quad (3a)$$

$$= \hat{T} + \hat{U} + i[S, \hat{T} + \hat{U}] + \frac{i^2}{2}[S, [S, \hat{T} + \hat{U}]] + \dots \quad (3b)$$

$$= \hat{U} + \underbrace{\hat{T} + i[S, \hat{U}]}_{\mathcal{O}(t)} + \underbrace{i[S, \hat{T}] + \frac{i^2}{2}[S, [S, \hat{U}]]}_{\mathcal{O}(t^2/U)} + \underbrace{\dots}_{\mathcal{O}(t^3/U^2)}. \quad (3c)$$

Here, we split the Hubbard Hamiltonian H into the kinetic energy part \hat{T} , the first term of (1), and the potential energy part \hat{U} , the second term of (1) (which includes the parameter U). In (3c) we have ordered the terms in powers of t/U . For a block

[†]A possible ansatz for finite temperatures was recently proposed by Anderson [113]. He suggests a spin-charge locking mechanism within the Gutzwiller–RVB theory to describe the pseudogap phase in the underdoped cuprates as a vortex liquid state.

diagonal Hamiltonian $H^{(\text{eff})}$ to order $\mathcal{O}(t/U)$, the term $\hat{T} + i[S, \hat{U}]$ in (3c) may not contain any (real) hopping processes changing the total number of doubly occupied sites. An appropriate choice for S is given by,

$$S = -i \sum_{\langle ij \rangle, \sigma} \frac{t_{(i,j)}}{U} \left(a_{i,\sigma}^\dagger d_{j,\sigma} + a_{j,\sigma}^\dagger d_{i,\sigma} - \text{h.c.} \right), \quad (4)$$

because

$$\hat{T} + i[S, \hat{U}] = - \sum_{\langle ij \rangle, \sigma} t_{(ij)} \left(a_{i\sigma}^\dagger a_{j\sigma} + d_{i\sigma}^\dagger d_{j\sigma} + \text{h.c.} \right), \quad (5)$$

does not involve hopping processes changing the number of double occupancies. Here, we used the operators $a_{i,\sigma}^\dagger \equiv (1 - n_{i,-\sigma})c_{i,\sigma}^\dagger$ and $d_{i,\sigma}^\dagger \equiv n_{i,-\sigma}c_{i,\sigma}^\dagger$. Equation (5) is block diagonal and verifies the choice of S in (4).

The full form of $H^{(\text{eff})}$ is now obtained by evaluating all $\mathcal{O}(t^2/U)$ terms in (3c) with S from (4). By restricting ourselves to the subspace of no double occupancies (the low-energy subspace or the lower Hubbard band (LHB)), we find the t - J Hamiltonian,

$$H_{t-J} \equiv P_G H^{(\text{eff})} P_G = P_G (T + H_J + H_3) P_G, \quad (6)$$

where

$$P_G = \sum_i (1 - n_{i\uparrow} n_{i\downarrow}), \quad (7)$$

is the Gutzwiller projection operator that projects out all doubly occupied sites. The terms of the Hamiltonian are given by,

$$T = - \sum_{\langle i,j \rangle, \sigma} t_{(i,j)} \left(c_{i,\sigma}^\dagger c_{j,\sigma} + c_{j,\sigma}^\dagger c_{i,\sigma} \right), \quad (8)$$

$$H_J = \sum_{\langle i,j \rangle} J_{(i,j)} \left(\mathbf{S}_i \mathbf{S}_j - \frac{1}{4} n_i n_j \right), \quad (9)$$

$$\begin{aligned} H_3 = & - \sum_{i, \tau_1 \neq \tau_2, \sigma} \frac{J_{(i+\tau_1, i, i+\tau_2)}}{4} c_{i+\tau_1, \sigma}^\dagger c_{i, -\sigma}^\dagger c_{i, -\sigma} c_{i+\tau_2, \sigma} \\ & + \sum_{i, \tau_1 \neq \tau_2, \sigma} \frac{J_{(i+\tau_1, i, i+\tau_2)}}{4} c_{i+\tau_1, -\sigma}^\dagger c_{i, \sigma}^\dagger c_{i, -\sigma} c_{i+\tau_2, \sigma}, \end{aligned} \quad (10)$$

where $J_{(i,j)} = 4t_{(i,j)}^2/U$ and $J_{(i,j,l)} = 4t_{(i,j)}t_{(j,l)}/U$. $\langle i,j \rangle$ are pairs of neighbour sites and $i + \tau_{(1,2)}$ denotes a neighbour site of i . Equation (6), together with (8)–(10), gives the full form of t - J Hamiltonian. However, the so-called correlated hopping or three-site term H_3 is often ignored because its expectation value is proportional both to t^2/U and the doping level x . Further, the density–density contribution $n_i n_j$ is sometimes neglected within the superexchange term H_J , as it is a constant at half-filling. Note that (8) is equivalent to (5) owing to the projection operators P_G occurring in the definition (6) of the t - J Hamiltonian.

The unitary transformation illustrates the relationship between superexchange and the physics of the (strong coupling) Hubbard model. We see that as a result of the unitary transform, the low-energy model is given by the t - J Hamiltonian (6)

which does not allow for double occupancies. At half-filling, each site is singly occupied and the hopping of electrons is frozen because real hopping now leads to states in the upper Hubbard band. As a result, the kinetic energy term in the Hamiltonian vanishes, and the t – J Hamiltonian reduces to an antiferromagnetic Heisenberg model (2).

The original Hamiltonian relevant for the cuprates contains three bands per unit cell, one copper band and two oxygen-derived bands. One band only crosses the FS with a single effective degree of freedom per unit cell, the Zhang–Rice singlet [25], corresponding to an empty site in t – J terminology. Using this venue, the hopping matrix elements and the superexchange parameters relevant for the t – J model could be derived directly. The Hubbard- U entering the relations derived above then takes the role of an effective modelling parameter.

2.5. Implementations of the RVB concept

The t – J Hamiltonian (6) is more suitable than the Hubbard model for studying RVB superconductivity, because it includes the superexchange term explicitly, and it is this term which is responsible for the formation of singlets. However, for exact numerical methods, the t – J Hamiltonian provides only a minor simplification over the Hubbard Hamiltonian, and one must turn to approximate schemes for any calculations on sufficiently large clusters. In the following, we start with the t – J Hamiltonian as an appropriate microscopic model for HTSCs, and briefly discuss three schemes that allow for systematic calculations of the RVB state.

2.5.1. Gutzwiller projected wave functions. Anderson [15] proposed projected BCS wave functions as possible RVB trial states for the t – J model. These states provide a suggestive way to describe an RVB liquid in an elegant and compact form[†],

$$|\Psi_{\text{RVB}}\rangle = P_N P_G |\text{BCS}\rangle, \quad (11)$$

with the BCS wave function

$$|\text{BCS}\rangle = \prod_{\mathbf{k}} \left(u_{\mathbf{k}} + v_{\mathbf{k}} c_{\mathbf{k}\uparrow}^\dagger c_{-\mathbf{k}\downarrow}^\dagger \right) |0\rangle, \quad (12)$$

which constitutes a singlet pairing state. Here, the operator P_G (Gutzwiller projection operator) projects out double occupancies and the P_N fixes the particle number to N ; $u_{\mathbf{k}}$ and $v_{\mathbf{k}}$ are the variational parameters with the constraint, $u_{\mathbf{k}}^2 + v_{\mathbf{k}}^2 \equiv 1$. The form of $|\Psi_{\text{RVB}}\rangle$ provides a unified description of the Mott insulating phase and the doped conductor. It immediately suggests the presence of singlet correlations in the undoped correlations and relates them to a superconducting state away from half-filling.

Projected wave functions were originally proposed by Gutzwiller in 1963 to study the effect of correlations presumed to induce ferromagnetism in transition metal compounds [118]. In subsequent years, these wave functions were applied to study the Mott–Hubbard metal insulator transition [119] and for a description of liquid

[†]For a real space representation of equation (11) we refer to section 5.1.1.

^3He as an almost localized Fermi liquid [116, 120, 121], etc. However, these early studies considered only a projected Fermi sea,

$$P_G|\Psi_{\text{FS}}\rangle = P_G \prod_{\mathbf{k} < \mathbf{k}_F} c_{\mathbf{k}\uparrow}^\dagger c_{\mathbf{k}\downarrow}^\dagger |0\rangle, \quad (13)$$

in the Hubbard model, whereas Anderson [15] suggested a projected BCS paired wave function for the t - J model.

To calculate the variational energy of a projected state $|\Psi\rangle \equiv P_G|\Psi_0\rangle$, expectation values of the form

$$\frac{\langle\Psi_0|P_G\hat{O}P_G|\Psi_0\rangle}{\langle\Psi_0|P_GP_G|\Psi_0\rangle} \quad (14)$$

must be considered, where \hat{O} is the appropriate operator. Here, $|\Psi_0\rangle$ can be any wave function with no restriction in the number of double occupancies, namely, it lives in the so-called ‘pre-projected’ space. The choice of $|\Psi_0\rangle$ In our case we concentrate on $|\Psi_0\rangle = |\text{BCS}\rangle$. In section 2.6 we review a few other types of trial wave functions used to study correlated electron systems. The exact evaluation of (14) is quite sophisticated and requires VMC techniques that are discussed in section 5. However, approximate analytical calculations can be performed with a renormalization scheme based on the Gutzwiller approximation (GA). The GA is outlined in the sections 3 and 4. Within this approximation, the effects of projection on the state $|\Psi_0\rangle$ are approximated by a classical statistical weight factor multiplying the expectation value with the unprojected wave function [120], i.e.

$$\frac{\langle\Psi_0|P_G\hat{O}P_G|\Psi_0\rangle}{\langle\Psi_0|P_GP_G|\Psi_0\rangle} \approx g_O \frac{\langle\Psi_0|\hat{O}|\Psi_0\rangle}{\langle\Psi_0|\Psi_0\rangle}. \quad (15)$$

The so-called Gutzwiller renormalization factor g_O only depends on the local densities and is derived by Hilbert space counting arguments [20, 120, 122] or by considering the limit of infinite dimensions ($d = \infty$) [123–126]. The GA shows good agreement with VMC results (see [20]) and is discussed detailed in section 3.

Gutzwiller projected wave functions thus have the advantage that they can be studied both analytically (using the GA and extensions thereof) and numerically (using VMC techniques and exact diagonalization). As these wave functions provide a simple way to study correlations such as pairing correlations, magnetic correlations, etc., in the presence of a large Hubbard repulsive interaction, they have been used extensively in the literature. As we show in the following sections, the Gutzwiller–RVB theory of superconductivity explains several key features of the HTSCs. More generally, we believe this approach is sufficiently broad that it could be used to study a wide range of physical phenomena in the proximity of a Mott transition.

2.5.2. SBMFT and RVB gauge theories. Another representation of the t - J Hamiltonian, equation (6), is obtained by removing the projection operators P_G , and replacing the creation and annihilation operators by

$$c_{i,\sigma}^\dagger \rightarrow \tilde{c}_{i,\sigma}^\dagger c_{i,\sigma}^\dagger (1 - n_{i,-\sigma}), \quad (16a)$$

$$c_{i,\sigma} \rightarrow \tilde{c}_{i,\sigma} = c_{i,\sigma} (1 - n_{i,-\sigma}), \quad (16b)$$

with $\sigma = \uparrow, \downarrow$ and $-\sigma$ denoting the opposite spin of σ . In this form the restriction to no double occupation is fulfilled by the projected operators $\tilde{c}_{i,\sigma}^\dagger$ and $\tilde{c}_{i,\sigma}$. Thus, only empty and singly occupied sites are possible, which can be expressed by the local inequality

$$\sum_{\sigma} \langle \tilde{c}_{i,\sigma}^\dagger \tilde{c}_{i,\sigma} \rangle \leq 1. \quad (17)$$

However, the new operators do not satisfy the fermion commutation relations, which makes an analytical treatment difficult. The slave-boson method [127–129] handles this problem by decomposing $\tilde{c}_{i,\sigma}^\dagger$ into a fermion operator $f_{i,\sigma}^\dagger$ and a boson operator b_i by means of

$$\tilde{c}_{i\sigma}^\dagger = f_{i,\sigma}^\dagger b_i. \quad (18)$$

The physical meaning of $f_{i,\sigma}^\dagger$ ($f_{i,\sigma}$) is to create (annihilate) a singly occupied site with spin σ , those of b_i (b_i^\dagger) to annihilate (create) an empty site. As every site can either be singly occupied by an \uparrow electron, singly occupied by a \downarrow electron or empty, the new operators must fulfill the condition

$$f_{i\uparrow}^\dagger f_{i\uparrow} + f_{i\downarrow}^\dagger f_{i\downarrow} + b_i^\dagger b_i = 1. \quad (19)$$

When writing the Hamiltonian in terms of the slave fermion and boson operators the constraint (19) is implemented by a Lagrangian multiplier λ_i . In the slave-boson representation, the t – J model is thus written as

$$\begin{aligned} H_{t-J} = & - \sum_{\langle i,j \rangle, \sigma} t_{(i,j)} \left(f_{i,\sigma}^\dagger b_i b_j^\dagger f_{j,\sigma} + f_{j,\sigma}^\dagger b_j b_i^\dagger f_{i,\sigma} \right) \\ & - \sum_{\langle i,j \rangle} J_{(i,j)} \left(f_{i\uparrow}^\dagger f_{j\downarrow}^\dagger - f_{i\downarrow}^\dagger f_{j\uparrow}^\dagger \right) (f_{i\downarrow} f_{j\uparrow} - f_{i\uparrow} f_{j\downarrow}) \\ & - \mu_0 \sum_{i,\sigma} f_{i,\sigma}^\dagger f_{i,\sigma} + \sum_i \lambda_i \left(f_{i\uparrow}^\dagger f_{i\uparrow} + f_{i\downarrow}^\dagger f_{i\downarrow} + b_i^\dagger b_i - 1 \right), \end{aligned} \quad (20)$$

where the Heisenberg exchange term

$$\mathbf{S}_i \mathbf{S}_j - \frac{1}{4} n_i n_j = - \left(f_{i\uparrow}^\dagger f_{j\downarrow}^\dagger - f_{i\downarrow}^\dagger f_{j\uparrow}^\dagger \right) (f_{i\downarrow} f_{j\uparrow} - f_{i\uparrow} f_{j\downarrow}),$$

is a function of fermion operators only, because superexchange does not lead to charge fluctuations [95]. Furthermore, a chemical potential term, $-\mu_0 \sum_{i,\sigma} f_{i,\sigma}^\dagger f_{i,\sigma}$, is included within the grand canonical ensemble.

The advantage of this representation is that the operators ($f_{i\sigma}, b_i$) obey standard algebra and can thus be treated using field theoretical methods. The partition function Z of (20) can be written as a functional integral over coherent Bose and Fermi fields, allowing observables to be calculated in the original Hilbert space. The Fermi fields can be integrated out using standard Grassmann variables. Then carrying out a saddle-point approximation for the Bose fields reproduces the mean-field level. The incorporation of Gaussian fluctuations around the saddle point approximation provides a possibility for systematic extensions of the SBMFT. One way to implement the constraint of single occupancy is to formulate the problem as a gauge theory.

The development of RVB correlations and a superconducting phase in a lattice model as a gauge theory was first studied by Baskaran and Anderson [130]. These authors noted that the Heisenberg Hamiltonian has a local $U(1)$ gauge symmetry, which arises precisely because of the constraint of single occupancy. One may then develop an effective action which obeys this local symmetry and use it to calculate various averages. As the free energy exhibits the underlying gauge symmetry, it is possible to go beyond mean-field theory when calculating averages of physical quantities. Doping turns the local gauge symmetry into a (weaker) global $U(1)$ symmetry which can be broken spontaneously, leading to superconductivity. Subsequently, Wen and Lee introduced an $SU(2)$ gauge theory which leads to RVB correlations and superconductivity in a doped Mott insulator [131]. These approaches are reviewed in a recent work by Lee *et al.* [19]. It should be noted that the GA and the SBMFT (which is the mean-field solution about which gauge theories are constructed) are similar in the sense that both model the doped Mott insulator. In particular, real kinetic energy is frozen as one approaches half-filling and enhanced RVB correlations. In general, the results from SBMFT are quite similar to those from RMFT, e.g. the early prediction of d -wave superconductivity in the t - J model rests on very similar gap equations in both schemes. The SBMFT result showing d -wave pairing by Kotliar and Liu [18] and by Suzumura *et al.* [96] nearly simultaneously appeared with the respective RMFT study by Zhang *et al.* [20]. These studies followed an earlier work of Baskaran *et al.* [95], who initially developed a slave-boson theory for the t - J model. For a more detailed review on SBMFT we refer the interested reader to [19]. The SBMFT and Gutzwiller approaches differ in the way the local constraint is treated and, consequently, there are quantitative discrepancies between these approaches. Some of these are highlighted in subsequent sections of this review.

2.5.3. The b-RVB theory. As the name indicates, this approach is based on a bosonic description of the t - J model. The advantage of this method is that it accounts well for the antiferromagnetic correlations of the Heisenberg model at half-filling as well as of the hole doped t - J model. At half filling, the ground state of the b-RVB theory is related to the RVB wave function of Liang *et al.* [71] which is the best variational wave function available for the Heisenberg model. The basic premise of the b-RVB theory is that hole doping of an insulator with antiferromagnetic correlations (not necessarily long ranged) leads to a singular effect called the ‘phase string’ effect [132]. A hole moving slowly in a closed path acquires a non-trivial Berry’s phase. As this effect is singular at the length scales of a lattice constant, its topological effect can be lost in conventional mean-field theories. So, the theory proposes to take this effect into account explicitly before invoking mean-field-like approximations. The electron operator is expressed in terms of bosonic spinon and holon operators, and a topological vortex operator, as

$$c_{i\sigma} = h_i^\dagger b_{i\sigma} e^{i\hat{\Theta}_{i\sigma}}.$$

The phase operator $\hat{\Theta}_{i\sigma}$ is the most important ingredient of the theory and reflects the topological effect of adding a hole to an antiferromagnetic background. The effective theory is described by holons and spinons coupled to each other by link fields.

Away from half-filling, the ground state of the b-RVB theory is described by a holon condensate and an RVB paired state of spinons. The superconducting order parameter is characterized by phase vortices that describe spinon excitations and the superconducting transition occurs as a binding/unbinding transition of such vortices [133]. The theory leads naturally to a vortex state above T_c of such spinon vortices [134]. Bare spinon and holon states are confined in the superconducting state and nodal (fermionic) QPs are obtained as composite objects [135].

The b-RVB theory realizes, transparently, the original idea of Anderson of holes moving in a prepaired RVB state. As mentioned above, the theory leads to definite and verifiable consequences such as a vortex state of spinons above T_c and spinon excitations trapped in vortex cores. However, the exact relationship between the b-RVB ground state and the simple Gutzwiller projected BCS wave function has not yet been clarified [136].

2.6. Variational approaches to correlated electron systems

In this section, we briefly discuss how projected states,

$$|\Psi\rangle = P_G |\Psi_0\rangle, \quad (21)$$

can be extended to study a wide variety of strongly correlated systems. Apart from the HTSCs, these wave functions have been used in the description of Mott insulators [137], superconductivity in organic compounds [94, 138] or Luttinger liquid behaviour in the t - J model [139, 140].

2.6.1. Order parameters. A simple extension of the trial state (21) is to allow for additional order parameters in the mean-field wave function $|\Psi_0\rangle$. In section 2.5.1, we restricted ourselves to a superconducting BCS wave function $|\Psi_0\rangle = |\text{BCS}\rangle$. However, antiferromagnetic [75, 102–105], π -flux [105, 141, 142] or charge-ordered [98–101] mean-field wave functions can also be used for $|\Psi_0\rangle$. In addition, a combination of different kinds of orders is possible. As an example, consider the trial wave function,

$$|\Psi_0\rangle = \prod_{\mathbf{k}} \left(u_{\mathbf{k}} + v_{\mathbf{k}} b_{\mathbf{k}\uparrow}^\dagger b_{-\mathbf{k}\downarrow}^\dagger \right) |0\rangle, \quad (22)$$

with

$$b_{\mathbf{k}\sigma} = \alpha_{\mathbf{k}} c_{\mathbf{k}\sigma} + \sigma \beta_{\mathbf{k}} c_{\mathbf{k}+\mathbf{Q}\sigma}. \quad (23)$$

Equation (22) includes finite superconducting as well as antiferromagnetic order [103]. Here, $b_{\mathbf{k}}$ is the Hartree–Fock spin-wave destruction operator with $\mathbf{Q} = (\pi, \pi)$ as required for a commensurate antiferromagnet. The parameters $\alpha_{\mathbf{k}}$ and $\beta_{\mathbf{k}}$ are related to the antiferromagnetic order parameter Δ_{AF} by usual mean-field relations; similarly, the superconducting order parameter determines the values of $v_{\mathbf{k}}$ and $u_{\mathbf{k}}$. In sections 4 and 5, we discuss applications of the above wave function for the HTSCs.

We note that $|\Psi_0\rangle$ is applicable to all lattice geometries. It has been used, for instance, to study superconductivity in triangular lattice-based cobaltates [86, 88–90] and organic compounds [92–94, 138]. Recent calculations show that projected states also provide a competitive energy on more exotic models such as a spin- $\frac{1}{2}$ Heisenberg model on a Kagome lattice [143].

2.6.2. Jastrow correlators. The incorporation of the Jastrow correlator \mathcal{J} [144] provides an additional powerful way to extend the class of (projected) trial wave functions. In (21), the original Gutzwiller projector P_G can be viewed as the simplest form of a Jastrow correlator,

$$P_G = \mathcal{J}_g = g^{\sum_i n_{i,\uparrow} n_{i,\downarrow}} = \prod_i (1 - (1 - g) n_{i,\uparrow} n_{i,\downarrow}). \quad (24)$$

So far we have only considered P_G in the fully projected limit, which corresponds to $g \rightarrow 0$ in J_g . However, when using (24) in the Hubbard model, g becomes a variational parameter that determines the number of doubly occupied sites.

The variational freedom of the trial wave function can be increased by including further Jastrow correlators,

$$|\Psi\rangle = \mathcal{J}_s \mathcal{J}_{\text{hd}} \mathcal{J}_d P_G |\Psi_0\rangle = \mathcal{J}_s \mathcal{J}_{\text{hd}} \mathcal{J}_d \mathcal{J}_g |\Psi_0\rangle. \quad (25)$$

Popular choices of Jastrow correlators are the density–density correlator \mathcal{J}_d ,

$$\mathcal{J}_d = \exp\left(-\sum_{(i,j)} v_{ij}(1 - n_i)(1 - n_j)\right), \quad (26)$$

the holon–doublon correlator \mathcal{J}_{hd} ,

$$\mathcal{J}_{\text{hd}} = \exp\left(-\sum_{(i,j)} w_{ij}(h_i d_j + d_i h_j)\right), \quad (27)$$

with $h_i = (1 - n_{i\uparrow})(1 - n_{i\downarrow})$ and $d_i = n_{i\uparrow} n_{i\downarrow}$, and the spin–spin correlator \mathcal{J}_s ,

$$\mathcal{J}_s = \exp\left(-\sum_{(i,j)} u_{ij} S_i^z S_j^z\right). \quad (28)$$

The corresponding variational parameter are given by v_{ij} , w_{ij} and u_{ij} , respectively.

As the generalized trial wave function (25) includes a very high number of variational parameters, one invariably chooses a small set depending on the problem at hand. In the case of the t – J model the situation is slightly simplified, because double occupancies are forbidden and thus $g \rightarrow 0$ and $w_{ij} = 0$.

We now discuss the properties of the density–density correlator in (26) and assume $u_{ij} = w_{ij} = 0$ for a moment. A positive v_{ij} implies density–density repulsion, a negative v_{ij} means attraction and may lead to phase separation. Several studies indicate the importance of long-range density–density Jastrow correlators for improving the variational energy. Hellberg and Mele [139] showed that the 1D t – J model can be accurately described when $v_{i,j} \sim \log|i - j|$, i.e. when the Jastrow correlator is scale invariant. The incorporation of long-ranged density–density correlations induces Luttinger liquid-like behaviour in the t – J model [139, 140]. In the 1D Hubbard model an appropriate choice of the density–density correlator in momentum space allows one to distinguish between metallic and insulating behaviour [137]. In the 2D t – J model, \mathcal{J}_d is often used to improve the variational energy of a projected superconducting state [145, 146] as we discuss in section 5.2.

The holon–doublon Jastrow correlator \mathcal{J}_{hd} is important for studying the repulsive Hubbard model on a variational basis. A negative $w_{i,j} < 0$ implies attraction of empty and doubly occupied sites which ultimately may lead to a Mott–Hubbard

insulating state (the Mott transition) [94, 138]. In two dimensions, a negative nearest neighbour, $w_{i,j} \sim -\delta_{\langle ij \rangle}$, substantially decreases the variational energy [94, 138], because these states occur as intermediate states during the superexchange process (cf. figure 13). Combining these effects with a superconducting wave function $|\Psi_0\rangle = |\text{BCS}\rangle$ then explains key aspects of superconductivity in organic compounds near the Mott–Hubbard transition [94, 138]. The w_{ij} seems to be less important for one dimension, and is likely to be a consequence of the very good spin–spin correlation energy of the Gutzwiller wave function in one dimension [116, 147].

The spin–spin Jastrow correlator \mathcal{J}_s is not used as often as the density–density and the holon–doublon Jastrow correlators (\mathcal{J}_d and \mathcal{J}_{hd}). However, recent studies show that the inclusion of \mathcal{J}_s is important when considering charge fluctuations within the 2D t – J model [148]. An appropriate spin–spin Jastrow correlator \mathcal{J}_s can also create antiferromagnetic order in a non-magnetic wave function, an example for the ability of Jastrow correlators to induce a new long-range order not manifest in the unprojected wave function.

3. Gutzwiller approximation

The GA is a straightforward method to handle Gutzwiller projected wave functions, which incorporate strong electron correlations by prohibiting doubly occupied sites. Within the GA, the effects of projection are absorbed by statistical weight factors (Gutzwiller renormalization factors), which then allow for an analytical treatment of strongly correlated Gutzwiller wave functions.

In this section, we present the derivation of the Gutzwiller factors by Hilbert space counting argument as well as considering the limit of infinite dimensions. Further, we discuss the importance of fugacity factors in the GA when comparing analytical results with VMC calculations in the canonical and grand canonical scheme, respectively. As we show in the last part of this section, the GA can also be extended to the case of partially projected wave functions, where the projection operator does not act on a single ‘reservoir’ site in the system.

3.1 Basic principles of the GA

The GA (or Gutzwiller renormalization scheme) constitutes the basis of the RMFT and is a successful method to treat Hilbert space restrictions owing to strong electron correlations. It was applied originally [118, 119] to calculate the variational energy of the projected Fermi sea, $P_G|FS\rangle$, in Hubbard-like models. In these and other early papers, the projection operator[†], $P_G = \prod_i (1 - \alpha \hat{n}_{i\uparrow} \hat{n}_{i\downarrow})$, was generalized to partial projection with the parameter α determined by optimizing the energy. Partially projected states were used successfully in modelling normal liquid ³He [120, 149] and heavy fermion systems [150, 151].

Here, we focus on the t – J model (i.e. the large U limit of the Hubbard model). Consequently, we mainly discuss the fully projected case, i.e. $\alpha = 1$. We derive the

[†]To avoid confusion, in this section we denote density operators with a ‘hat’ and write, e.g., $\hat{n}_{i\sigma} = c_{i\sigma}^\dagger c_{i\sigma}$.

corresponding renormalization factors (Gutzwiller renormalization factors) in this limit and do not discuss the generalization to finite double occupancy. The latter case is obtained easily following the same reasoning. The GA

$$\frac{\langle \Psi_0 | P_G \hat{O} P_G | \Psi_0 \rangle}{\langle \Psi_0 | P_G P_G | \Psi_0 \rangle} \approx g_O \frac{\langle \Psi_0 | \hat{O} | \Psi_0 \rangle}{\langle \Psi_0 | \Psi_0 \rangle}, \quad (29)$$

approximates the expectation value within the projected state $P_G |\Psi_0\rangle$ by a corresponding statistical weight g_O multiplying the matrix element within the unprojected wave function $|\Psi_0\rangle$. To determine the Gutzwiller renormalization factor g_O we can either invoke Hilbert space counting arguments [20, 120, 122] or consider the limit of infinite dimensions ($d = \infty$) [123–126]. In the following, we review both techniques and compare the respective results.

3.1.1. Gutzwiller renormalization factors by counting arguments. Hilbert space counting arguments enable us to derive the renormalization factor g_O through simple physical reasoning. We may use

$$g_O \approx \frac{\langle \hat{O} \rangle_\Psi}{\langle \hat{O} \rangle_{\Psi_0}} \quad (30)$$

with $|\Psi\rangle \equiv P_G |\Psi_0\rangle$, as defining the factor g_O ; $\langle \cdots \rangle_\Psi$ denotes the expectation value with respect to the (projected) wave function $|\Psi\rangle$. In the GA, the ratio in (30) is determined by neglecting correlations in the wave functions $|\Psi\rangle$ and $|\Psi_0\rangle$. The physical quantity which determines the theory is the occupancy at any site i . Thus, one calculates the probabilities for a site i to be empty, singly occupied with spin σ and doubly occupied, respectively. These probabilities are obtained by considering the Hilbert space restrictions and are summarized for $|\Psi\rangle$ and $|\Psi_0\rangle$ in table 1. In this context, we should note that the densities before projection (n_i^0 , $n_{i\downarrow}^0$ and $n_{i\uparrow}^0$) and after projection (n_i , $n_{i\downarrow}$ and $n_{i\uparrow}$) may differ. This is due to the projection operator, $P_G = \prod_i (1 - \hat{n}_{i\downarrow} \hat{n}_{i\uparrow})$, which can, e.g., remove more terms with an \uparrow electron than a \downarrow electron on site i . Such effects become of importance for Gutzwiller projection in antiferromagnetic, charge ordered or grand-canonical states. Keeping this caveat in mind, the expectation values in (30) can be calculated approximately by considering the probability amplitudes of ‘bra’ and ‘ket’ configurations that contribute. We obtain the Gutzwiller renormalization factor by calculating the ratio between these

Table 1. Probability for different occupancies on site i in $|\Psi\rangle$ and $|\Psi_0\rangle$. We distinguish between the densities before projection (n_i^0 , $n_{i\downarrow}^0$ and $n_{i\uparrow}^0$) and after projection (n_i , $n_{i\downarrow}$ and $n_{i\uparrow}$).

Occupancy on site i	Probabilities	
	In $ \Psi\rangle$	In $ \Psi_0\rangle$
$\langle (1 - \hat{n}_{i\downarrow})(1 - \hat{n}_{i\uparrow}) \rangle$	$1 - n_i$	$(1 - n_{i\downarrow}^0)(1 - n_{i\uparrow}^0)$
$\langle \hat{n}_{i\downarrow}(1 - \hat{n}_{i\uparrow}) \rangle$	$n_{i\downarrow}$	$n_{i\downarrow}^0(1 - n_{i\uparrow}^0)$
$\langle \hat{n}_{i\uparrow}(1 - \hat{n}_{i\downarrow}) \rangle$	$n_{i\uparrow}$	$n_{i\uparrow}^0(1 - n_{i\downarrow}^0)$
$\langle \hat{n}_{i\downarrow} \hat{n}_{i\uparrow} \rangle$	0	$n_{i\downarrow}^0 n_{i\uparrow}^0$

approximate expectation values. Although we neglect any off-site correlations in the derivation of the Gutzwiller renormalization factor, the GA itself (29) incorporates additional correlations by the expectation value of \hat{O} in $|\Psi_0\rangle$. Extensions of the GA, which incorporate more correlation effects, were proposed by Ogata and Himeda [107] (see also section 4.4.1) and Hsu [152].

To illustrate the above scheme, we consider the expectation value of the hopping element, $\langle c_{i\uparrow}^\dagger c_{j\uparrow} \rangle$. For a projected state, $|\Psi\rangle = P_G |\Psi_0\rangle$, we can write

$$\langle c_{i\uparrow}^\dagger c_{j\uparrow} \rangle_\Psi = \langle (1 - \hat{n}_{i\downarrow}) c_{i\uparrow}^\dagger (1 - \hat{n}_{j\downarrow}) c_{j\uparrow} \rangle_\Psi. \quad (31)$$

We then perform the GA for the right-hand side of (31), which is written in terms of projected operators $(1 - \hat{n}_{i\downarrow}) c_{i\uparrow}^\dagger$ and $(1 - \hat{n}_{j\downarrow}) c_{j\uparrow}$. It is convenient to rewrite the matrix elements in this manner before performing the GA, because it guarantees agreement with the infinite dimensions approach. Next we consider the probability for $\langle (1 - \hat{n}_{i\downarrow}) c_{i\uparrow}^\dagger (1 - \hat{n}_{j\downarrow}) c_{j\uparrow} \rangle$ in $|\Psi\rangle$ and $|\Psi_0\rangle$. Configurations can only contribute if the bra vector has a single \uparrow electron on site i and a vacancy on site j . For the ket vector the interchanged occupancies are necessary, i.e. a single \uparrow electron on site j and a vacancy on site i . The corresponding hopping process is illustrated in figure 18. With the help of table 1 we find the amplitudes of the bra and ket contribution and the product gives the probability in $|\Psi\rangle$,

$$[n_{i\uparrow}(1 - n_j)]^{1/2} \cdot [n_{j\uparrow}(1 - n_i)]^{1/2}, \quad (32)$$

and in $|\Psi_0\rangle$,

$$[n_{i\uparrow}^0(1 - n_{i\downarrow}^0)(1 - n_{j\downarrow}^0)(1 - n_{j\uparrow}^0)]^{1/2} \cdot [n_{j\uparrow}^0(1 - n_{j\downarrow}^0)(1 - n_{i\downarrow}^0)(1 - n_{i\uparrow}^0)]^{1/2}. \quad (33)$$

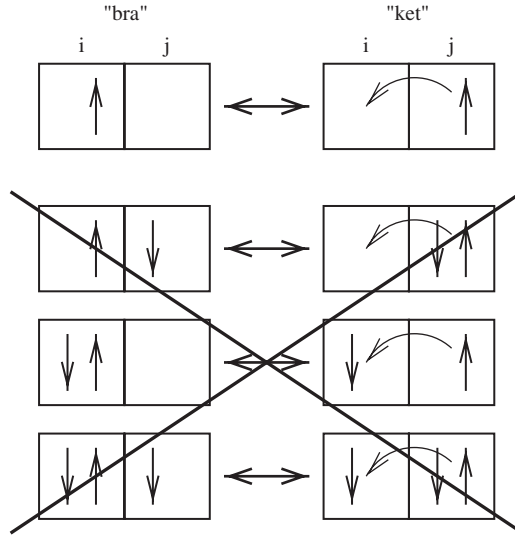


Figure 18. Required bra and ket configurations, so that $\langle (1 - \hat{n}_{i\downarrow}) c_{i\uparrow}^\dagger (1 - \hat{n}_{j\downarrow}) c_{j\uparrow} \rangle$ contributes in $|\Psi\rangle$ and $|\Psi_0\rangle$. Configurations that do not contribute to $\langle (1 - \hat{n}_{i\downarrow}) c_{i\uparrow}^\dagger (1 - \hat{n}_{j\downarrow}) c_{j\uparrow} \rangle$ are crossed out.

The square roots stem from the fact that both bra and ket vectors only provide amplitudes; the probability is obtained by a product of two amplitudes.

Combining (32) and (33) yields

$$\frac{\langle (1 - \hat{n}_{i\downarrow})c_{i\uparrow}^\dagger (1 - \hat{n}_{j\downarrow})c_{j\uparrow} \rangle_{|\Psi\rangle}}{\langle (1 - \hat{n}_{i\downarrow})c_{i\uparrow}^\dagger (1 - \hat{n}_{j\downarrow})c_{j\uparrow} \rangle_{|\Psi_0\rangle}} \approx \tilde{g}_t = \frac{1}{(1 - n_{i\downarrow}^0)(1 - n_{j\downarrow}^0)} \cdot \frac{[n_{i\uparrow}(1 - n_j)n_{j\uparrow}(1 - n_i)]^{1/2}}{[n_{i\uparrow}^0(1 - n_{j\uparrow}^0)n_{j\uparrow}^0(1 - n_{i\uparrow}^0)]^{1/2}}. \quad (34)$$

The expectation value in $|\Psi\rangle$ is now obtained by renormalizing the unprojected value by (34),

$$\langle c_{i\uparrow}^\dagger c_{j\uparrow} \rangle_\Psi = \langle (1 - \hat{n}_{i\downarrow})c_{i\uparrow}^\dagger (1 - \hat{n}_{j\downarrow})c_{j\uparrow} \rangle_\Psi \quad (35a)$$

$$\approx \tilde{g}_t \langle (1 - \hat{n}_{i\downarrow})c_{i\uparrow}^\dagger (1 - \hat{n}_{j\downarrow})c_{j\uparrow} \rangle_{\Psi_0} \quad (35b)$$

$$\approx \underbrace{\tilde{g}_t (1 - n_{i\downarrow}^0)(1 - n_{j\downarrow}^0)}_{=g_t} \langle c_{i\uparrow}^\dagger c_{j\uparrow} \rangle_{\Psi_0}. \quad (35c)$$

In the last row of (35) we decoupled the densities in $|\Psi_0\rangle$. The Gutzwiller renormalization factor is then

$$g_t = \frac{[n_{i\uparrow}(1 - n_j)n_{j\uparrow}(1 - n_i)]^{1/2}}{[n_{i\uparrow}^0(1 - n_{j\uparrow}^0)n_{j\uparrow}^0(1 - n_{i\uparrow}^0)]^{1/2}}. \quad (36)$$

We emphasize that the decoupling in (35c) is controlled in the limit of infinite dimensions, namely, all neglected decouplings yield off-site correlations of higher order[†] and thus vanish for $d = \infty$. Violating this rule causes deviations from the mathematical thoroughness of the infinite-dimension scheme.

For the full determination of the Gutzwiller renormalization factor in (36), it is necessary to evaluate the dependence of the densities after projection relative to the densities prior to projection. The situation is particularly simple for a homogeneous wave functions with fixed particle number and spin symmetry, where $n_{i\uparrow}^0 = n_{i\downarrow}^0 = n_i^0/2 = n/2$ on each site i . Then, $n_{i\uparrow} = n_{i\downarrow} = n/2$ and the Gutzwiller factor simplifies to the well-known result,

$$g_t = \frac{1 - n}{1 - n/2}, \quad (37)$$

which incorporates the fact that the kinetic energy in $|\Psi\rangle$ is connected to the motion of holes, vanishing in the undoped case.

However, the relation of the $n_{i\sigma}$ with respect to the $n_{i\sigma}^0$ become more subtle, if we consider, e.g., an antiferromagnet with sublattice magnetization m , where $n_{A\sigma}^0 = n/2 \pm m$ and $n_{B\sigma}^0 = n_{B-\sigma}^0$ (sublattices A and B , $\sigma = \uparrow, \downarrow$). In this case, $n_{i\sigma} \neq n_{i\sigma}^0$ and we must invoke counting arguments to determine $n_{i\sigma}$. We consider a canonical ensemble, where the overall particle density is the same before and after projection ($n_i = n_{i\uparrow} + n_{i\downarrow} = n_{i\uparrow}^0 + n_{i\downarrow}^0 = n_i^0 = n$). Furthermore, the density $n_{i\sigma}$

[†]Strictly speaking, we violate this rule by neglecting decouplings which include on-site pairing, $\langle c_{i\uparrow}^\dagger c_{i\downarrow}^\dagger \rangle$. However, we work in the fully projected limit, i.e. $|\Psi\rangle$ does not allow for on-site pairing. It is thus reasonable to prohibit on-site pairing in $|\Psi_0\rangle$ as well and to set $\langle c_{i\uparrow}^\dagger c_{i\downarrow}^\dagger \rangle \equiv 0$.

is necessarily related to the probability of finding a single σ electron at site i in $|\Psi_0\rangle$. Thus, $n_{i\sigma} \propto n_{i\sigma}^0(1 - n_{i-\sigma}^0)$. Owing to the conserved particle density,

$$n_{i\uparrow} + n_{i\downarrow} = n = n^0 \quad (38)$$

and so

$$n_{i\sigma} = n_{i\sigma}^0(1 - n_{i-\sigma}^0) \frac{n}{n - 2n_{i\uparrow}^0 n_{i\downarrow}^0}. \quad (39)$$

Inserting this expression in the numerator of (36) gives the Gutzwiller renormalization factor,

$$g_t = \frac{1 - n}{1 - 2n_{i\uparrow}^0 n_{i\downarrow}^0 / n}, \quad (40)$$

where $n_{i\uparrow}^0$ and $n_{i\downarrow}^0$ are from the same site. We note that (39) is valid for sites i and j on the same as well as on different sublattices as one can show easily and reduces to $g_t = (1 - n)/(1 - n/2)$ in the non-magnetic limit, $n_{i\sigma}^0 = n/2$.

The situation becomes yet more complicated if we consider states with an inhomogeneous particle density, where it is difficult to determine n_i , $n_{i\downarrow}$ and $n_{i\uparrow}$. Therefore, most authors assume $n_i = n_i^0$. However, this assumption is incorrect, because the operator $P_G = \sum_i (1 - \hat{n}_{i\uparrow} \hat{n}_{i\downarrow})$ allows for changes in the local particle density. An elegant solution is to redefine the operator P_G , so that $n_i = n_i^0$ or even $n_{i\sigma} = n_{i\sigma}^0$. This conservation of local particle densities can be achieved by incorporating appropriate fugacity factors (that describe the local chemical potential) into a new operator \tilde{P}_G (Gutzwiller correlator), which is then no longer a projection operator. The redefined operator \tilde{P}_G still allows us to present any projected wave function as $|\Psi\rangle = \tilde{P}_G |\tilde{\Psi}_0\rangle$, however, the unprojected wave function $|\tilde{\Psi}_0\rangle$ will generally differ from $|\Psi_0\rangle$ defined by $|\Psi\rangle = P_G |\Psi_0\rangle$. The use of \tilde{P}_G instead of P_G is often not explicitly stated in literature, although the assumed conservation of densities is only valid for a generalized Gutzwiller correlator \tilde{P}_G . Such a clear distinction between \tilde{P}_G and P_G becomes particularly important when results from the GA are compared with VMC calculations that implement the original Gutzwiller projector P_G . The non-conservation of local particle densities by the operator P_G also explains discrepancies between VMC calculations in the canonical and the grand canonical scheme [5]. This is discussed in more detail in section 3.2.

Before turning to the $d = \infty$ scheme, let us discuss the Gutzwiller renormalization factor g_S for the superexchange interaction, defined by

$$\langle \mathbf{S}_i \mathbf{S}_j \rangle_\Psi = g_S \langle \mathbf{S}_i \mathbf{S}_j \rangle_{\Psi_0}. \quad (41)$$

We first consider the GA for the contribution $\langle S_i^+ S_j^- \rangle$, i.e.

$$\langle S_i^+ S_j^- \rangle_\Psi = g_S^\pm \langle S_i^+ S_j^- \rangle_{\Psi_0}. \quad (42)$$

The procedure resembles the derivation of g_t . We note that the process $S_i^+ S_j^-$ requires an \uparrow spin on site i and a \downarrow spin on site j in the bra vector, and the reverse in the ket vector. Therefore, the probability becomes

$$(n_{i\uparrow} n_{j\downarrow} n_{i\downarrow} n_{j\uparrow})^{1/2} \quad (43)$$

in the state $|\Psi\rangle$, while it is

$$[n_{i\uparrow}^0(1 - n_{i\downarrow}^0)n_{j\downarrow}^0(1 - n_{j\uparrow}^0)n_{i\downarrow}^0(1 - n_{i\uparrow}^0)n_{j\uparrow}^0(1 - n_{j\downarrow}^0)]^{1/2} \quad (44)$$

in the state $|\Psi_0\rangle$. Using $n_{i,\sigma}$ from (39) yields

$$g_S^\pm = \frac{1}{(1 - 2n_\uparrow^0 n_\downarrow^0/n)^2}. \quad (45)$$

One can show again that the above formula also results for the case of sites belonging to the same sublattice.

Next we evaluate the GA for the diagonal contribution to the superexchange,

$$\langle S_i^z S_j^z \rangle_\Psi = g_S^z \langle S_i^z S_j^z \rangle_{\Psi_0}. \quad (46)$$

Here, we use $S_i^z = 1/2(\hat{n}_{i\uparrow} - \hat{n}_{i\downarrow})$ and write

$$4\langle S_i^z S_j^z \rangle = \langle \hat{n}_{i\uparrow}(1 - \hat{n}_{i\downarrow})\hat{n}_{j\uparrow}(1 - \hat{n}_{j\downarrow}) \rangle + \langle \hat{n}_{i\downarrow}(1 - \hat{n}_{i\uparrow})\hat{n}_{j\downarrow}(1 - \hat{n}_{j\uparrow}) \rangle \\ - \langle \hat{n}_{i\uparrow}(1 - \hat{n}_{i\downarrow})\hat{n}_{j\downarrow}(1 - \hat{n}_{j\uparrow}) \rangle - \langle \hat{n}_{i\downarrow}(1 - \hat{n}_{i\uparrow})\hat{n}_{j\uparrow}(1 - \hat{n}_{j\downarrow}) \rangle, \quad (47)$$

which is valid for any wave function. The GAs of the terms in (47) give a common renormalization factor,

$$g_S^z = \frac{1}{(1 - 2n_\uparrow^0 n_\downarrow^0/n)^2}. \quad (48)$$

This is seen by considering the term $\langle \hat{n}_{i\uparrow}(1 - \hat{n}_{i\downarrow})\hat{n}_{j\uparrow}(1 - \hat{n}_{j\downarrow}) \rangle$ in (47), as an example. By applying the probabilities from table 1, we obtain,

$$\frac{\langle \hat{n}_{i\uparrow}(1 - \hat{n}_{i\downarrow})\hat{n}_{j\uparrow}(1 - \hat{n}_{j\downarrow}) \rangle_\Psi}{\langle \hat{n}_{i\uparrow}(1 - \hat{n}_{i\downarrow})\hat{n}_{j\uparrow}(1 - \hat{n}_{j\downarrow}) \rangle_{\Psi_0}} \approx \frac{n_{i\uparrow}n_{j\uparrow}}{n_{i\uparrow}^0(1 - n_{i\downarrow}^0)n_{j\uparrow}^0(1 - n_{j\downarrow}^0)} \equiv g_S^z, \quad (49)$$

where using (39) for $n_{i\uparrow}n_{j\uparrow}$ directly confirms (48). As all density terms of (47) renormalize in exact the same manner, g^{z-S} gives the correct renormalization factor for $\langle S_i^z S_j^z \rangle_\Psi$ in (46).

From (45) and (48), we find a common Gutzwiller renormalization factor, $g_S = g_S^\pm = g_S^z$, for (41), which simplifies to

$$g_S = \frac{1}{(1 - n/2)^2}, \quad (50)$$

in the non-magnetic limit, $n_\sigma^0 = n/2$. At half-filling, $n=1$ and $g_S \rightarrow 4$, the magnetic correlations are four times as pronounced in $|\Psi\rangle$ than in $|\Psi_0\rangle$. We note that GAs for other quantities are easily obtained by following the same reasoning as for g_t and g_S .

3.1.2. Gutzwiller renormalization factors in infinite dimensions. The effects of the Gutzwiller correlator can be evaluated exactly in the limit of infinite dimensions [123, 124]. Gebhard [124] showed that a simple diagrammatic evaluation is possible for $d = \infty$. Using the Gutzwiller renormalization factors from $d = \infty$ for finite dimensions corresponds to a mean-field approximation. Thus, the $d = \infty$ approach provides a systematic way to calculate Gutzwiller factors. Typically, one is interested in the doping dependence of such factors and, here, the results from $d = \infty$ are in qualitative agreement with Gutzwiller factors calculated using counting arguments.

Discrepancies between the two methods are merely quantitative. Here, we summarize the calculation of Gutzwiller factors in the limit $d = \infty$, for fully projected states. The reader is referred to recent works of Bünemann *et al.* [125, 126] for a detailed account.

To simplify calculations, the Gutzwiller projector P_G is reformulated as a Gutzwiller correlator \tilde{P}_G within the $d = \infty$ scheme. This redefinition agrees with that discussed earlier and ensures that local densities are conserved, namely, $n_{i\sigma} = n_{i\sigma}^0$. The Gutzwiller correlator, $\tilde{P}_G = \prod_i \tilde{P}_{G,i}$, is written as a product of local correlators,

$$\tilde{P}_{G,i} = \lambda_i^0 (1 - \hat{n}_{i\downarrow})(1 - \hat{n}_{i\uparrow}) + \lambda_i^\uparrow \hat{n}_{i\uparrow}(1 - \hat{n}_{i\downarrow}) + \lambda_i^\downarrow \hat{n}_{i\downarrow}(1 - \hat{n}_{i\uparrow}). \quad (51)$$

Physically, the parameters λ_i^0 and λ_i^σ allow us to weight locally the probabilities to find empty sites and sites occupied with a spin σ , respectively. The λ_i^0 , λ_i^\uparrow and λ_i^\downarrow are determined by the constraints

$$\langle \tilde{P}_{G,i}^2 \rangle_{\tilde{\Psi}_0} \equiv 1, \quad (52)$$

$$\langle \tilde{P}_{G,i} \hat{n}_{i\sigma} \tilde{P}_{G,i} \rangle_{\tilde{\Psi}_0} = \langle \hat{n}_{i\sigma} \rangle_{\tilde{\Psi}_0} = n_{i\sigma}^0. \quad (53)$$

Equation (52) guarantees the normalization, $\langle \Psi | \Psi \rangle = \langle \Psi_0 | \tilde{P}_G \tilde{P}_G | \Psi_0 \rangle = 1$, of the projected wave function and equation (53) provides the conservation of local densities. Evaluating these equations, we find

$$\lambda_i^0 = \sqrt{\frac{1 - n_i}{(1 - n_{i\downarrow})(1 - n_{i\uparrow})}}, \quad (54)$$

$$\lambda_i^\sigma = \sqrt{\frac{1}{(1 - n_{i-\sigma})}}. \quad (55)$$

Using these parameters in the Gutzwiller correlator \tilde{P}_G guarantees by means of (52) a conserved norm and by means of (53) conserved spin densities for any projected wave function, $|\Psi\rangle \equiv \tilde{P}_G |\tilde{\Psi}_0\rangle$. The GA for an operator \hat{O}_{ij} acting on the sites i and j is now obtained by neglecting all correlations except those between sites i and j . This procedure becomes exact in infinite dimensions and is written as

$$\langle \tilde{\Psi}_0 | \tilde{P}_G \hat{O}_{ij} \tilde{P}_G | \tilde{\Psi}_0 \rangle = \langle \tilde{\Psi}_0 | \tilde{P}_{G,i} \tilde{P}_{G,j} \hat{O}_{ij} \tilde{P}_{G,i} \tilde{P}_{G,j} | \tilde{\Psi}_0 \rangle. \quad (56)$$

Decoupling the right-hand site and neglecting all off-site correlations of higher order, provides the exact solution for $d = \infty$, which agrees with the results from counting arguments presented in section 3.1.1.

As an example, we consider the hopping process, $\langle c_{i\uparrow}^\dagger c_{j\uparrow} \rangle_{\tilde{P}_G |\tilde{\Psi}_0\rangle}$. Using (56), we find

$$\langle \tilde{\Psi}_0 | \tilde{P}_G c_{i\uparrow}^\dagger c_{j\uparrow} \tilde{P}_G | \tilde{\Psi}_0 \rangle = \langle \tilde{\Psi}_0 | \tilde{P}_{G,i} c_{i\uparrow}^\dagger \tilde{P}_{G,i} \tilde{P}_{G,j} c_{j\uparrow} \tilde{P}_{G,j} | \tilde{\Psi}_0 \rangle \quad (57a)$$

$$= \lambda_i^\uparrow \lambda_j^0 \lambda_j^\uparrow \langle \tilde{\Psi}_0 | (1 - \hat{n}_{i\downarrow}) c_{i\uparrow}^\dagger (1 - \hat{n}_{j\downarrow}) c_{j\uparrow} | \tilde{\Psi}_0 \rangle \quad (57b)$$

$$= \underbrace{\lambda_i^\uparrow \lambda_j^0 \lambda_j^\uparrow}_{=g_t} (1 - n_{i\downarrow})(1 - n_{j\downarrow}) \langle \tilde{\Psi}_0 | c_{i\uparrow}^\dagger c_{j\uparrow} | \tilde{\Psi}_0 \rangle, \quad (57c)$$

where we decoupled the densities in the last row as already done in the discussion using counting arguments. Equation (57) is exact in infinite dimensions and gives the Gutzwiller renormalization factor

$$g_t = \sqrt{\frac{(1 - n_j)(1 - n_i)}{(1 - n_{j\uparrow})(1 - n_{i\uparrow})}}, \quad (58)$$

which agrees with (36) if we assume locally conserved densities. However, we note that this result differs from (40), which incorporates the changed spin densities due to the projection operator P_G . The scheme presented above is applicable to any kind of operator and gives the exact result for $d = \infty$. It provides a useful check for results derived from counting arguments. Nevertheless we must keep in mind that results may differ depending on our choice of P_G and $P_G|\Psi_0\rangle$ or \tilde{P}_G and $\tilde{P}_G|\tilde{\Psi}_0\rangle$ in the counting arguments leading to the derivation of the Gutzwiller renormalization factors.

3.2 GA in the canonical and the grand canonical scheme

In this section we follow Edegger *et al.* [5] and study the effects of projection on superconducting BCS wave functions,

$$|\Psi_0\rangle = |\text{BCS}\rangle \equiv \prod_{\mathbf{k}} (u_{\mathbf{k}} + v_{\mathbf{k}} c_{\mathbf{k}\uparrow}^\dagger c_{-\mathbf{k}\downarrow}^\dagger) |0\rangle. \quad (59)$$

As $|\Psi_0\rangle = |\text{BCS}\rangle$ exhibits particle number fluctuations, the projection operator P_G can change the average particle number N of the wave function, i.e. in general,

$$\frac{\langle \Psi_0 | \hat{N} | \Psi_0 \rangle}{\langle \Psi_0 | \Psi_0 \rangle} \neq \frac{\langle \Psi_0 | P_G \hat{N} P_G | \Psi_0 \rangle}{\langle \Psi_0 | P_G^2 | \Psi_0 \rangle}. \quad (60)$$

In the above equation, the equality between the left- and right-hand sides could be recovered by replacing the Gutzwiller projector P_G by a Gutzwiller correlator \tilde{P}_G which conserves local densities as discussed in the previous section. Here, we follow a different route to compensate for the effects of projection by using a fugacity factor in the wave function. This ansatz explains the differences observed between VMC calculations in the canonical framework (fixed particle number) and the grand canonical ensemble (fluctuating particle number) using the corresponding GA.

3.2.1. Incorporation of a fugacity factor. We first examine the particle number distributions to illustrate the effect of the projection operator P_G in the projected Hilbert space. Towards this end, we write the average numbers, $\bar{N}^{(0)}(\bar{N})$ in the unprojected (projected) Hilbert space, as

$$\bar{N}^{(0)} = \sum_N N \rho_N^{(0)}, \quad \bar{N} = \sum_N N \rho_N, \quad (61)$$

where

$$\rho_N^{(0)} = \frac{\langle \Psi_0 | P_N | \Psi_0 \rangle}{\langle \Psi_0 | \Psi_0 \rangle}, \quad \rho_N = \frac{\langle \Psi_0 | P_G P_N P_G | \Psi_0 \rangle}{\langle \Psi_0 | P_G P_G | \Psi_0 \rangle}, \quad (62)$$

are the particle number distributions in the unprojected and projected BCS wave functions, respectively. Here, the operator P_N describes the projection onto terms with particle number N . As discussed in [5], we can relate the particle number distributions before and after projection by

$$\underbrace{\frac{\langle \Psi_0 | P_G P_N P_G | \Psi_0 \rangle}{\langle \Psi_0 | P_G P_G | \Psi_0 \rangle}}_{\rho_N} = g_N \underbrace{\frac{\langle \Psi_0 | P_N | \Psi_0 \rangle}{\langle \Psi_0 | \Psi_0 \rangle}}_{\rho_N^{(0)}}, \quad (63)$$

with

$$g_N = \frac{\langle \Psi_0 | \Psi_0 \rangle}{\underbrace{\langle \Psi_0 | P_G P_G | \Psi_0 \rangle}_{=C(=\text{const})}} \frac{\langle \Psi_0 | P_G P_N P_G | \Psi_0 \rangle}{\langle \Psi_0 | P_N | \Psi_0 \rangle}. \quad (64)$$

The above equation (63) describes the GA for the projection operator P_N with the corresponding renormalization factor g_N . The parameter C is an irrelevant constant, which does not depend on N . It follows that if we were to impose the condition that the average particle numbers before and after projection be identical, a factor g_N^{-1} needs to be included in (61). Then, from (61) and (63), we obtain the particle number after projection \bar{N}_{new} ,

$$\bar{N}_{\text{new}} \equiv \sum_N N \frac{1}{g_N} \rho_N = \sum_N N \frac{g_N \rho_N^{(0)}}{g_N} = \bar{N}^{(0)}, \quad (65)$$

which is the desired result.

This procedure can be implemented for the wave function $|\Psi_0\rangle$. As the BCS wave function is a linear superposition of states with particle numbers $\dots, N-2, N, N+2, \dots$, we consider the effect of projection on two states whose particle numbers differ by two. Then, the ratio is

$$f^2 \equiv \frac{g_{N+2}}{g_N} \approx \left(\frac{L-N}{L-N/2} \right)^2 \rightarrow \left(\frac{1-n}{1-n/2} \right)^2 = g_t^2 \quad (66)$$

where the factors g_N were evaluated combinatorially in the thermodynamic limit [5]. We note that the fugacity factor f is equal to g_t , the Gutzwiller renormalization factor for the hopping term (see also section 3.1). Equation (66) shows that the projection operator acts unequally on the N and $N+2$ particle states; the renormalization of the weight of the $N+2$ particle states g_{N+2} , is g_t^2 times the weight of the N particle states, g_N . This effect can be rectified as in (65) by multiplying every Cooper pair $c_{\mathbf{k}\uparrow}^\dagger c_{-\mathbf{k}\downarrow}^\dagger$ by a amplitude $\frac{1}{g_t}$ in the BCS wave function. Alternatively (following Anderson and Ong [153]), we can multiply every empty state by the factor g_t , and write

$$|\Psi_0^{(f)}\rangle = \prod_{\mathbf{k}} \frac{(g_t u_{\mathbf{k}} + v_{\mathbf{k}} c_{\mathbf{k}\uparrow}^\dagger c_{-\mathbf{k}\downarrow}^\dagger)}{\sqrt{g_t^2 |u_{\mathbf{k}}|^2 + |v_{\mathbf{k}}|^2}} |0\rangle. \quad (67)$$

Then again by construction, the fugacity factor $f=g_t$ in (67) ensures that the projected wave function $P_G |\Psi_0^{(f)}\rangle$ and the unprojected wave function $|\Psi_0\rangle$ without fugacity factor have the same particle number. The denominator in (67) is the new normalization factor. Two points deserve further attention. The first is that a relative

phase factor between N and $N + 2$ particle states in the projected BCS wave function can be absorbed into the definition of the fugacity factor. The second point is that our ansatz for the fugacity factor assumes that the effects of the projection operator are independent of k , i.e. the fugacity factor we obtain is independent of k . We do not see *a priori* why the fugacity factor cannot depend on k . This is an interesting line of investigation because a k -dependent fugacity factor in the Gutzwiller–BCS wave function would lead to (experimentally) verifiable consequences.

3.2.2. Singular particle number renormalization close to half-filling. We saw that the inclusion of the fugacity factor is necessary for the average particle number in a BCS wave function to remain unchanged when projecting out all doubly occupied sites. Alternatively, one might ask what is the effect of the projection operator on a BCS wave function if projection changes the mean particle number, because no fugacity factor is introduced.

In this situation, as shown by Edegger *et al.* [5], the particle density after projection is determined by the self-consistent equation,

$$\bar{N}_{\text{after}} \equiv \frac{\langle \Psi_0 | P_G \hat{N} P_G | \Psi_0 \rangle}{\langle \Psi_0 | P_G | \Psi_0 \rangle} \approx 2 \sum_{\mathbf{k}} \frac{g_t^2 |v_{\mathbf{k}}|^2}{|u_{\mathbf{k}}|^2 + g_t^2 |v_{\mathbf{k}}|^2}, \quad (68)$$

which can be solved iteratively with g_t specified by the particle number in \bar{N}_{after} . As the particle density in the state $|\Psi_0\rangle$ before projection is given by

$$\bar{n}_{\text{before}} \equiv \frac{\bar{N}_{\text{before}}}{L} = \frac{2}{L} \sum_{\mathbf{k}} |v_{\mathbf{k}}|^2, \quad (69)$$

equation (68) provides a way to calculate the particle number in the state $P_G |\Psi_0\rangle$ after projection, whenever the particle number in the state $|\Psi_0\rangle$ before projection is known as a function of the identical factors $u_{\mathbf{k}}$ and $v_{\mathbf{k}}$.

In the following, we discuss numerical solutions of (68), where we use the standard BCS expressions for a d -wave superconductor,

$$v_{\mathbf{k}}^2 = \frac{1}{2} \left(1 - \frac{\xi_{\mathbf{k}}}{E_{\mathbf{k}}} \right), \quad u_{\mathbf{k}}^2 = \frac{1}{2} \left(1 + \frac{\xi_{\mathbf{k}}}{E_{\mathbf{k}}} \right), \quad (70)$$

with,

$$E_{\mathbf{k}} = \sqrt{\Delta_{\mathbf{k}}^2 + \xi_{\mathbf{k}}^2}, \quad (71a)$$

$$\Delta_{\mathbf{k}} = \Delta(\cos k_x - \cos k_y), \quad (71b)$$

$$\xi_{\mathbf{k}} = -2(\cos k_x + \cos k_y) - \mu. \quad (71c)$$

Therefore, the only free parameters, which must be specified within the calculations, are the chemical potential μ and the order parameter Δ .

The particle numbers (before and after projection) for fixed values of the order parameter Δ can now be determined as a function of the chemical potential. The results for the particle densities are shown in figure 19. The results clearly show that the particle density before projection attains its maximal value ($n_{\text{before}} = 2$), when $n_{\text{after}} = 1$ (half-filling). This result holds for any finite value of the order parameter Δ . The case of half-filling, $n_{\text{after}} \rightarrow 1$, is therefore singular in the grand canonical scheme

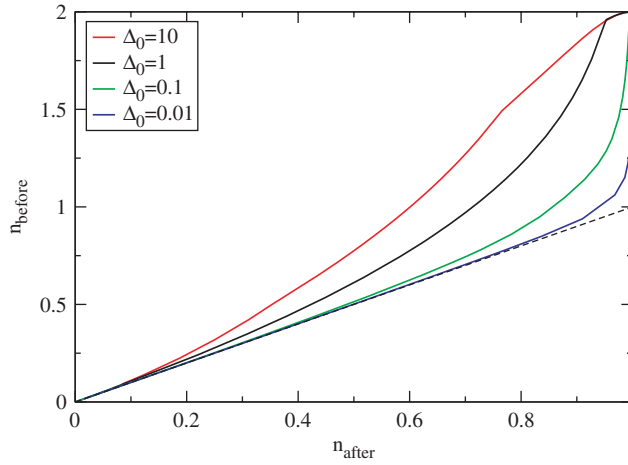


Figure 19. Particle density before projection n_{before} (equation (69)) as a function of the particle density after projection n_{after} (equation (68)) for different d -wave order parameters Δ . The dashed line indicates the Fermi liquid result $n_{\text{before}} = n_{\text{after}}$. Reprinted with permission from [5] © 2005 by the American Physical Society.

and large deviations with respect to the canonical framework can be expected. In the opposite limit, namely low densities of electrons, n_{before} converges to the value of n_{after} as expected. As illustrated by the results in figure 19, the size of the intermediate region depends on the magnitude of the order parameter Δ , i.e. the effects of projection are largest for wave functions with a large Δ and consequently large particle number fluctuations.

To check the accuracy of equation (68) we compare it with VMC calculations of Yokoyama and Shiba [97], who numerically studied a projected BCS wave functions with fluctuating particle number (but without a fugacity factor). Yokoyama and Shiba determined the particle density of the projected d -wave state $P_G|\Psi_0\rangle$ as a function of the parameter Δ for various fixed chemical potentials μ within a grand canonical scheme (see VMC data in figure 20). As the unprojected wave function $|\Psi_0\rangle$ was specified through (70)–(71) in the VMC calculation, we can also determine the relation between n_{after} and Δ by (68). As shown in figure 20, the results from (68) are in good qualitative agreement with the VMC data of Yokoyama and Shiba. Small discrepancies are mostly explained by finite size corrections in the VMC calculation (VMC calculations are only given for 6×6 and 8×8 lattices). figure 20 clearly reveals the singular effect of the projection near the insulating phase (half-filling), where the chemical potential diverges to infinity.

3.2.3. Gutzwiller renormalization factors in the canonical and the grand canonical ensemble. Next we discuss the differences between the GA in the canonical and grand canonical scheme. The validity of the analytical expressions derived in this section can be confirmed [5] by a comparison with numerically exact VMC calculations [17, 97].

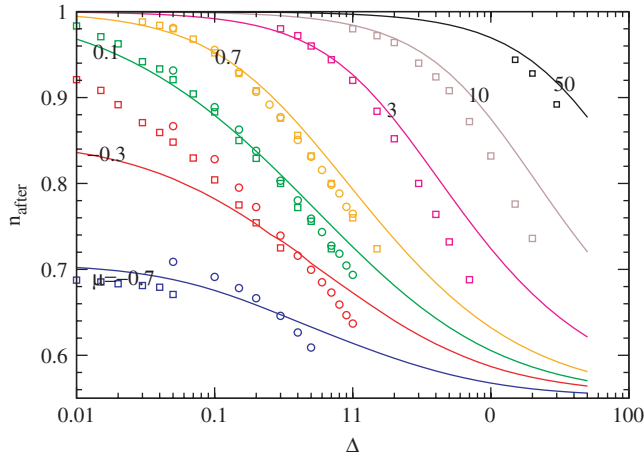


Figure 20. The particle density after projection n_{after} as a function of the parameter Δ for a d -wave BCS state at various chemical potentials μ . A comparison between results from equation (68) (solid curves) and the VMC results of Yokoyama and Shiba [97] (for 6×6 (circles) and 8×8 lattices (squares)) is shown. Numbers in the figure denote the chemical potentials of the corresponding curves. Reprinted with permission from [5] © 2005 by the American Physical Society.

We first consider the canonical case, where we are interested in the expectation value of an operator \hat{O} calculated within a projected wave function $P_N P_G |\Psi_0\rangle$ with fixed particle number. The GA corresponding to the operator \hat{O} is given by

$$\frac{\langle \Psi_0 | P_G P_N \hat{O} P_N P_G | \Psi_0 \rangle}{\langle \Psi_0 | P_G P_N P_G | \Psi_0 \rangle} \quad (72a)$$

$$\approx g_O \frac{\langle \Psi_0 | P_N \hat{O} P_N | \Psi_0 \rangle}{\langle \Psi_0 | P_N | \Psi_0 \rangle} \quad (72b)$$

$$= g_O \frac{\langle \Psi_0 | \hat{O} | \Psi_0 \rangle}{\langle \Psi_0 | \Psi_0 \rangle}, \quad (72c)$$

with the Gutzwiller renormalization factor g_O and the projector P_N onto terms with particle number N . The term (72a) represents a quantity which can be calculated exactly by the VMC scheme with fixed particle number [17, 21]. As the particle number is fixed, the usual GA can be invoked, leading to (72b). The equality to the last row is guaranteed only when N is equal to the average particle number of $|\Psi_0\rangle$ ($N = \bar{N}$). Under this condition a transformation from a canonical to a grand canonical ensemble is valid in the pre-projected Hilbert space.

In the grand canonical scheme the expectation value of \hat{O} is calculated with a particle number non-conserving wave function. Therefore, this scheme must be modified as follows,

$$\frac{\langle \Psi_0^{(f)} | P_G \hat{O} P_G | \Psi_0^{(f)} \rangle}{\langle \Psi_0^{(f)} | P_G P_G | \Psi_0^{(f)} \rangle} \approx g_O \frac{\langle \Psi_0 | \hat{O} | \Psi_0 \rangle}{\langle \Psi_0 | \Psi_0 \rangle}, \quad (73)$$

where $P_G|\Psi_0^{(f)}\rangle$ is the projected d -wave state including a fugacity factor (67). This correction is essential to guarantee the validity of the GA, because without it, the left-hand side and the right-hand side of (73) would correspond to states with different mean particle numbers. Equation (73) shows that a fugacity factor must be included in wave functions with particle number fluctuations when used for a GA.

A comparison of (72) and (73) gives an important result,

$$\frac{\langle\Psi_0|P_GP_N\hat{O}P_NP_G|\Psi_0\rangle}{\langle\Psi_0|P_GP_NP_G|\Psi_0\rangle}\approx\frac{\langle\Psi_0^{(f)}|P_G\hat{O}P_G|\Psi_0^{(f)}\rangle}{\langle\Psi_0^{(f)}|P_G^2|\Psi_0^{(f)}\rangle}. \quad (74)$$

This equation shows that to obtain identical results in the grand canonical (right-hand side) and canonical (left-hand side) scheme, one has to use different wave functions. The wave function $|\Psi_0^{(f)}\rangle$ is a d -wave state including a fugacity factor, whereas $|\Psi_0\rangle$ is a pure d -wave state.

The arguments leading up to (73) and (74) can be verified by a comparison with VMC studies. In figure 21, we show GAs from Edegger *et al.* [5] together with the corresponding VMC calculations, i.e. fixed particle number VMC [17] for the canonical scheme and particle number non-conserving VMC [97] for the grand canonical scheme. The figure shows that canonical and grand canonical approaches yield different energies; however, the GA qualitatively matches the corresponding VMC results. The differences in the two schemes are due to the projection operator P_G , which changes the particle number in a grand canonical wave function. For these two methods to yield the same results, a fugacity factor must be incorporated into the wave function when working in a grand canonical ensemble. We note that the discrepancies between the canonical and the grand canonical scheme increase significantly towards half-filling as illustrated in figure 22. This effect is due to the strong renormalization of the particle density in this limit (see figure 19).

3.3 GA for partially projected states

Thus far, we discussed the Gutzwiller renormalization scheme for fully projected wave functions. It is sometimes necessary, however, to consider partially projected states of the form

$$|\Psi'_l\rangle = P'_l|\Psi_0\rangle, \quad P'_l = \prod_{i \neq l} (1 - \hat{n}_{i\uparrow}\hat{n}_{i\downarrow}). \quad (75)$$

The wave function $|\Psi'_l\rangle$ describes a state where double occupancies are projected out on all sites except the site l , which we call the ‘reservoir’ site. The reason for the appearance of reservoir sites can be seen as follows. Consider, for example, the operator $P_G c_{l\uparrow}$, which can be rewritten as $c_{l\uparrow} P'_l$. Such commutations become necessary, e.g., for the calculation of the QP weight (discussed in section 6), where partially projected states arise inevitably.

Before discussing $|\Psi'_l\rangle$ in more detail, we remark that the notation ‘partially projected’ is also used for a projection operator

$$P_\alpha = \prod_i (1 - \alpha \hat{n}_{i\uparrow} \hat{n}_{i\downarrow}), \quad (76)$$

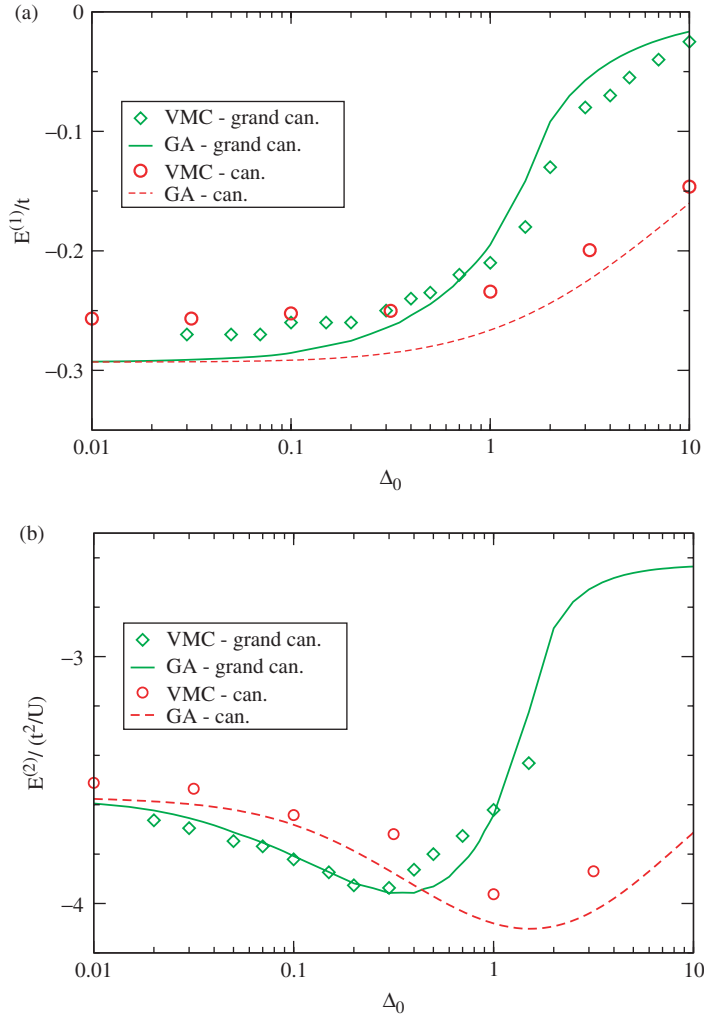


Figure 21. (a) The kinetic energy $E^{(1)}$ and (b) the energy of the remaining terms $E^{(2)}$ per site of the t - J model as a function of Δ for the d -wave state at a filling $n=0.9$. Fixed particle (canonical, circles) VMC data [17] and grand canonical (grand canonical, squares) VMC data [97] are compared. The dashed/solid curves represent the corresponding GA. Reprinted with permission from [5] © 2005 by the American Physical Society.

with $\alpha \in [0, 1]$. The operator P_α is used for studying Hubbard-like model with ‘partially projected’ wave functions $P_\alpha|\Psi_0\rangle$ (see also section 3.1). Here, the parameter α controls the total number of double occupancies, whereas P'_i in (75) yields a fully projected state with only a single unprojected reservoir site i . We emphasize that the respective GAs for these two projection operators are fundamentally different.

Below we follow the work of Fukushima *et al.* [6], who developed an analytical method to calculate expectation values for partially projected states (as defined

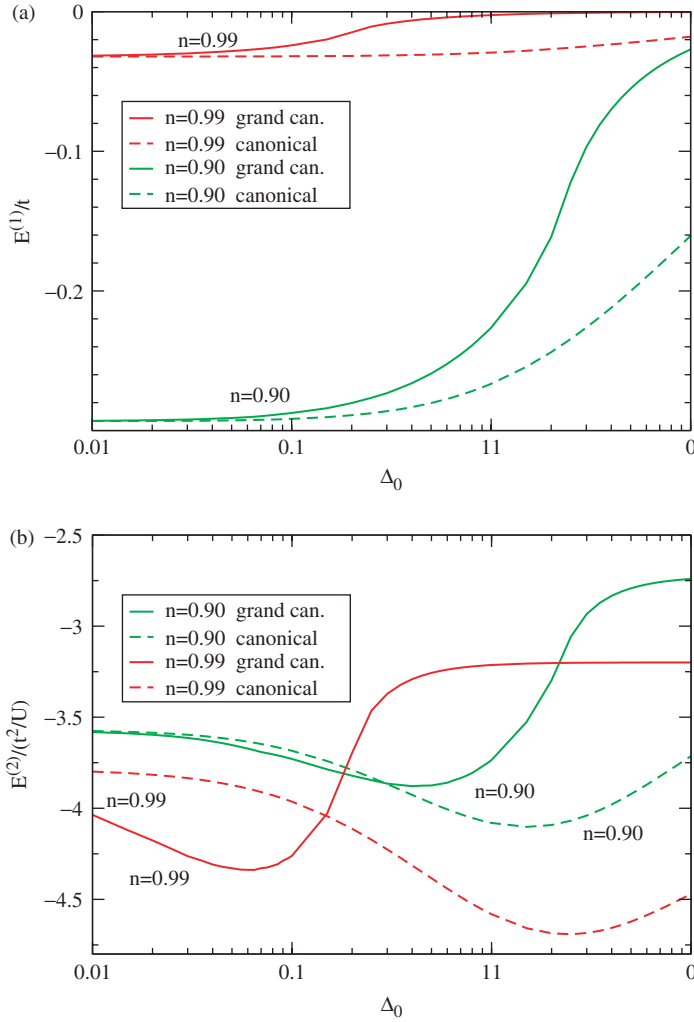


Figure 22. Comparison of the canonical and grand canonical scheme at filling (dashed curves) $n=0.9$ and (solid curves) $n=0.99$. (a) The kinetic energy $E^{(1)}$ and (b) the energy of the remaining terms $E^{(2)}$ per site of the t - J model are shown as a function of Δ for the d -wave state. The results are obtained by GAs, i.e. by means of (72) and (73) for the canonical and the grand canonical scheme, respectively. The calculations for the grand canonical scheme follow the steps given by [5].

in (75)). The calculations rest on counting arguments; however, in principle, similar results can be obtained within the infinite dimensions approach. We first determine the local occupancy of the reservoir site, which is then used to derive the Gutzwiller renormalization factors of specific expectation values. We also provide a comparison with VMC calculations to test the validity of the approximation and determine its limitations.

We are interested in expectation values such as

$$\frac{\langle \Psi'_l | \hat{O} | \Psi'_l \rangle}{\langle \Psi'_l | \Psi'_l \rangle} = g'_O \frac{\langle \Psi_0 | \hat{O} | \Psi_0 \rangle}{\langle \Psi_0 | \Psi_0 \rangle}, \quad (77)$$

that generalize the GA to partially projected wave functions. Note that the reservoir site does not have a special role in the unprojected wave function $|\Psi_0\rangle$. This is in contrast to the impurity problem, where an impurity site would break the translational invariance of both the unprojected and of the projected wave function.

3.3.1. Occupancy of the reservoir site. The GA in (77) can be performed by counting arguments as in the fully projected case (see section 3.1.1). However, the occupancy of the reservoir will differ from the occupancy of a fully projected site, an effect that must be considered when deriving Gutzwiller renormalization factors.

Fukushima *et al.* [6] showed that the probabilities for the reservoir site to be empty, singly occupied or doubly occupied are

$$\langle (1 - \hat{n}_{l\uparrow})(1 - \hat{n}_{l\downarrow}) \rangle_{\Psi'_l} = X(1 - n) \approx \frac{(1 - n)^2}{(1 - n_\uparrow)(1 - n_\downarrow)}, \quad (78)$$

$$\langle \hat{n}_{l\sigma}(1 - \hat{n}_{l-\sigma}) \rangle_{\Psi'_l} = Xn_\sigma \approx \frac{(1 - n)n_\sigma}{(1 - n_\uparrow)(1 - n_\downarrow)}, \quad (79)$$

$$\langle d \rangle_{\Psi'_l} \equiv \langle \hat{n}_{l\uparrow}\hat{n}_{l\downarrow} \rangle_{\Psi'_l} = 1 - X \approx \frac{n_\uparrow n_\downarrow}{(1 - n_\uparrow)(1 - n_\downarrow)}, \quad (80)$$

respectively. Here

$$X = \frac{\langle \Psi_0 | P_G P_G | \Psi_0 \rangle}{\langle \Psi_0 | P'_l P'_l | \Psi_0 \rangle} = \frac{\langle \Psi | \Psi \rangle}{\langle \Psi'_l | \Psi'_l \rangle} \quad (81)$$

is defined as the ratio between the normalizations $\langle \Psi | \Psi \rangle$ and $\langle \Psi'_l | \Psi'_l \rangle$. This ratio can be estimated by a GA [6] and becomes

$$X \approx \frac{1 - n}{(1 - n_\uparrow)(1 - n_\downarrow)} \quad (82)$$

in the thermodynamic limit, where $n_\sigma = N_\sigma/L$ ($\sigma = \uparrow, \downarrow$) and $n = n_\uparrow + n_\downarrow$ are the respective particle densities. We note that X vanishes at half-filling. Consequently the reservoir becomes exactly doubly occupied, i.e. $\lim_{n \rightarrow 1} \langle d \rangle_{\Psi'_l} = 1$.

3.3.2. Renormalization of mixed hopping terms. The occupancies of the reservoir site, (78)–(80), directly enter the respective Gutzwiller renormalization factor g'_O . We consider here, as an example, the mixed hopping term,

$$\frac{\langle \Psi_0 | P'_l c_{l\sigma}^\dagger c_{m\sigma} P'_l | \Psi_0 \rangle}{\langle \Psi_0 | P'_l P'_l | \Psi_0 \rangle} \approx g'_t \frac{\langle \Psi_0 | c_{l\sigma}^\dagger c_{m\sigma} | \Psi_0 \rangle}{\langle \Psi_0 | \Psi_0 \rangle}. \quad (83)$$

where l denotes the reservoir site and $m \neq l$ is a fully projected site. Following the arguments leading to (31), we rewrite

$$\langle c_{l\uparrow}^\dagger c_{m\uparrow} \rangle_{\Psi_l} = \langle c_{l\uparrow}^\dagger (1 - \hat{n}_{m\downarrow}) c_{m\uparrow} \rangle_{\Psi_l} \quad (84a)$$

$$\approx \tilde{g}'_l \langle c_{l\uparrow}^\dagger (1 - \hat{n}_{m\downarrow}) c_{m\uparrow} \rangle_{\Psi_0} \quad (84b)$$

$$\approx \underbrace{\tilde{g}'_l (1 - n_{m\downarrow})}_{=g'_l} \langle c_{l\uparrow}^\dagger c_{m\uparrow} \rangle_{\Psi_0}. \quad (84c)$$

As for (31), we perform the GA for the right-hand side of (84a) to guarantee agreement with the infinite dimensions approach. However, the decoupling of $(1 - n_{m\downarrow})$ in (84c) becomes exact in infinite dimensions and we can recover the GA of (83).

In analogy with the calculations in section 3.1, we consider the probability for $\langle c_{l\uparrow}^\dagger (1 - \hat{n}_{m\downarrow}) c_{m\uparrow} \rangle$ in $|\Psi_l\rangle$ to determine the corresponding Gutzwiller renormalization factor \tilde{g}'_l entering in (84c). We illustrate the two configurations that can contribute, together with the resulting probability from combining the bra and ket vectors, in figure 23. Using (78)–(80) for the partially projected site (grey boxes in figure 23), we find the probability

$$\begin{aligned} & ([Xn_{l\uparrow}X(1 - n_l)]^{1/2} + [(1 - X)Xn_{l\downarrow}]^{1/2}) \cdot [(1 - n_m)n_{m\uparrow}]^{1/2} \\ &= X \left([n_{l\uparrow}(1 - n_l)]^{1/2} + \left[\frac{1 - X}{X} n_{l\downarrow} \right]^{1/2} \right) \cdot [(1 - n_m)n_{m\uparrow}]^{1/2}, \end{aligned} \quad (85)$$

in $|\Psi_l\rangle$. With $n_{l\sigma} = n_{m\sigma} = n_\sigma$ and (82), the above expression simplifies to

$$X[n_\sigma(1 - n) + n_\sigma^2] = Xn_\sigma(1 - n_\sigma). \quad (86)$$

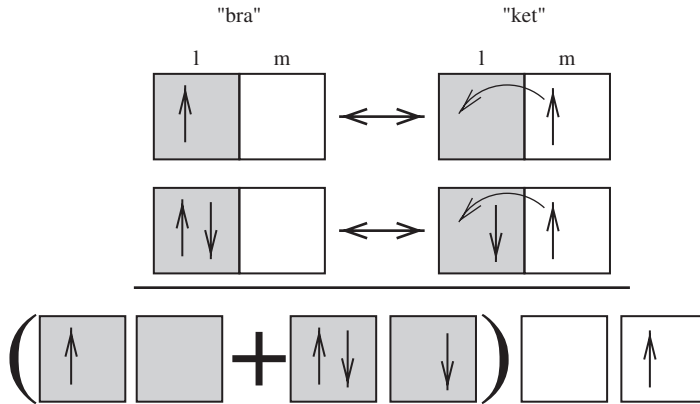


Figure 23. Required bra and ket configurations, so that $\langle c_{l\uparrow}^\dagger (1 - \hat{n}_{m\downarrow}) c_{m\uparrow} \rangle$ contribute in $|\Psi_l\rangle$ when l is a reservoir site (indicated by a shaded background). The last row presents the sum from the two possible contributions as used in (85). Boxes with white backgrounds indicate the fully projected site m .

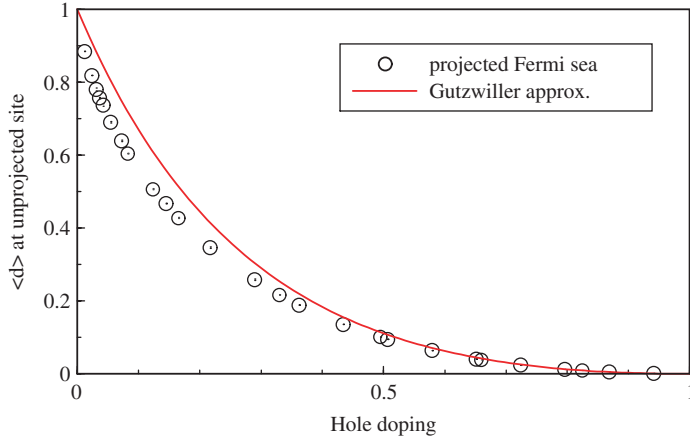


Figure 24. Double occupancy of the reservoir site $\langle d \rangle_{\Psi_i} = \langle \hat{n}_{I\uparrow} \hat{n}_{I\downarrow} \rangle_{\Psi_i}$ as a function of doping, for the partially projected Fermi sea. Note the good agreement between the Gutzwiller result (solid curve), equation (80), and the VMC results for the projected Fermi sea (open circles). Statistical errors and finite-size corrections are estimated to be smaller than the symbols. From [6].

For the respective probabilities in $|\Psi_0\rangle$, we use table 1 and obtain

$$[n_{I\uparrow}^0(1 - n_{I\downarrow}^0)]^{1/2} \cdot [n_{m\uparrow}^0(1 - n_{m\downarrow}^0)(1 - n_{m\downarrow}^0)(1 - n_{m\uparrow}^0)]^{1/2}. \quad (87)$$

As pointed out in section 3.1, $n_{I\sigma}^0 = n_{m\sigma}^0 = n_\sigma$, for non-magnetic wave functions. We then obtain the renormalization factor \tilde{g}'_t from the ratio of (86) and (87), i.e.

$$\tilde{g}'_t = \frac{X}{1 - n_\sigma}. \quad (88)$$

Together with (84c), we obtain the renormalization factor,

$$g'_t = (1 - n_\sigma)\tilde{g}'_t = X = \frac{1 - n}{(1 - n_\uparrow)(1 - n_\downarrow)}, \quad (89)$$

for the GA in (83). Other expectation values in partially projected states can be calculated similarly. In section 6, we use the same scheme in calculating the QP weight.

3.3.3. Comparison of the GA for partially projected states with VMC calculations. Before concluding this section, we illustrate a comparison between (80) and VMC results for $\langle d \rangle_{\Psi_i} = \langle \hat{n}_{I\uparrow} \hat{n}_{I\downarrow} \rangle_{\Psi_i} = 1 - X$. Fukushima *et al.* [6] found that the results obtained by a generalized GA are in excellent qualitative agreement with the VMC results for a partially projected Fermi sea as shown in figure 24. We also used VMC to obtain the same quantity using projected *s/d*-wave BCS states[†] as

[†]The BCS states are defined by $|v_{\mathbf{k}}|^2 = \frac{1}{2}(1 - \xi_{\mathbf{k}}/E_{\mathbf{k}})$ and $u_{\mathbf{k}}v_{\mathbf{k}}^* = \Delta_{\mathbf{k}}/(2E_{\mathbf{k}})$, where $\xi_{\mathbf{k}} = -2(\cos k_x + \cos k_y) - \mu$ and $E_{\mathbf{k}} = \sqrt{|\Delta_{\mathbf{k}}|^2 + \xi_{\mathbf{k}}^2}$ (*s*-wave, $\Delta_{\mathbf{k}} = \Delta$; *d*-wave, $\Delta_{\mathbf{k}} = \Delta(\cos k_x - \cos k_y)$).

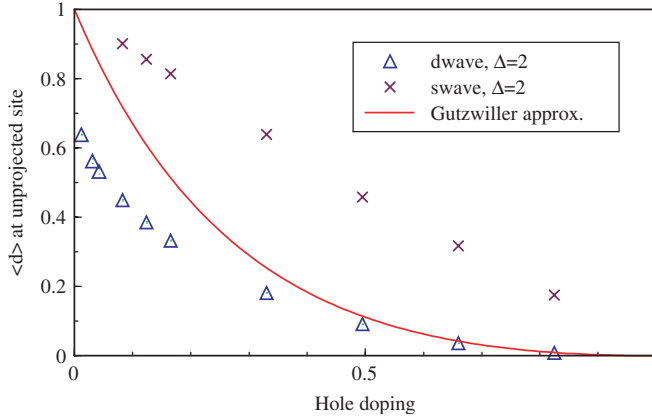


Figure 25. Double occupancy of the reservoir site $\langle d \rangle_{\Psi_I} = \langle \hat{n}_I \hat{n}_{I+1} \rangle_{\Psi_I}$ as a function of doping, for the partially projected BCS wave function. The solid curve is the GA result from (80). The parameterization follows [147]. Statistical errors and finite-size corrections for the VMC results are estimated to be smaller than the symbols. Reprinted with permission from [6] © 2005 by the American Physical Society.

variational states in the simulation. The results for $\langle d \rangle_{\Psi_I}$ in BCS states are shown in figure 25. In contrast to the projected Fermi sea, a clear deviation from the GA is seen. This underscores the importance of pairing correlations in the unprojected wave function that are not completely taken into account by the GA scheme. It also explains, to a certain extent, the discrepancies between the VMC calculations and the GA for the QP weight as we discuss in section 7.

To clarify the limitations of the GA for projected superconducting states in more detail, VMC can be used to calculate the hole density in the vicinity of the reservoir site. In the half-filled limit the reservoir site is doubly occupied and therefore a single hole is distributed among the remaining fully projected sites. The VMC calculations of Fukushima *et al.* [6] show very different density oscillations for the projected Fermi sea and the projected *d*-wave state.

Figure 26 shows VMC results for the hole density

$$n_h(m) = \langle 1 - n_m \rangle_{\Psi_I},$$

in the partially projected state $|\Psi_I\rangle$. The sites m are distinct from the reservoir site l (marked by a cross in the figure). All results shown correspond to half-filling, namely, $n_\uparrow = n_\downarrow = 0.5$. We choose $\Delta = 1$ for the projected BCS *d*-wave state. For the Fermi sea, we see that the hole is distributed more uniformly than in the *d*-wave case even though the diagonal direction has a larger probability of being occupied by a hole. The *d*-wave has a quasi-checkerboard pattern where only one of four sites is black, and the hole tends to be near the reservoir site. The VMC results for the projected BCS wave functions are strikingly different in that the hole density is *not* uniform. On the other hand, the GA would be exact if all states in the Hilbert space contribute equally to the wave function. That would correspond to a uniform density of holes. Clearly, some limitations in the GA show up when treating projected superconducting wave functions. This is in agreement with our previous

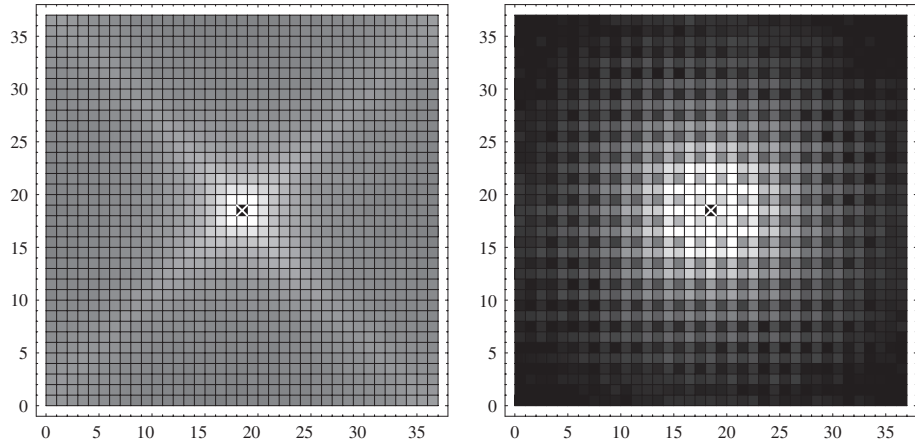


Figure 26. VMC results for the hole density $n_h(m) = \langle (1 - n_m) \rangle_{\Psi_l}$ (white/black corresponds to high/low values of $n_h(m)$) in the partially projected state $|\Psi_l\rangle$, for sites m other than the reservoir site l (marked by the cross). (a) Fermi sea. (b) d -wave state. Reprinted with permission from [6] © 2005 by the American Physical Society.

considerations, where we found that the functional form of X (equation (82), derived using GA) agrees well with the VMC calculations only for the projected Fermi sea, but not for the projected BCS state (see figures 24 and 25).

4. RMFT: basic ideas and recent extensions

On the basis of the GA, Zhang *et al.* [20] derived a RMFT for the t - J model. In this section, we present an overview on this approach, which plays a central role within Gutzwiller–RVB theory. We illustrate successes and recent extensions of the RMFT for the HTSCs, derive the RMFT gap equation and review its applications to the Hubbard model in the strong coupling limit. Further extensions to antiferromagnetic and inhomogeneous phases provide a quantitative description of the cuprate phase diagram.

4.1. Overview on the RMFT method

We start with an overview and discuss how RMFT allows for a systematic treatment of the Hubbard Hamiltonian in the strong coupling limit. We present the basic concepts in this section, and the method itself is discussed in detail in the following sections. Figure 27 summarizes the main steps necessary for the strong coupling treatment of the Hubbard model within the RMFT. In the following we refer to the individual steps illustrated in figure 27.

As shown in figure 27, the first step is to apply a canonical transformation e^{-iS} to the Hubbard Hamiltonian removing hopping processes that change the number of doubly occupied sites. In doing so, we obtain the t - J Hamiltonian, which is defined in the subspace excluding double occupancy. The t - J Hamiltonian provides an effective low-energy Hamiltonian for the Hubbard model in the strong coupling limit as already discussed in detail in section 2.4.

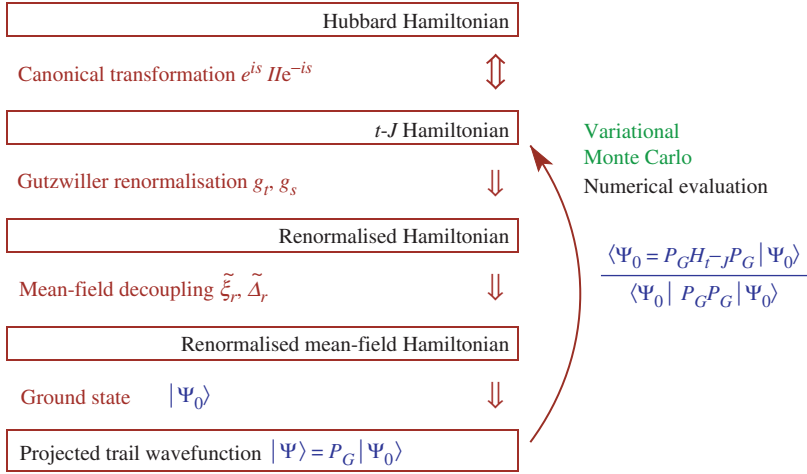


Figure 27. Schematic illustration of the RMFT method; see the text for a detailed description.

Next we invoke the GA to remove the restriction to projected states within the t - J Hamiltonian. As we discuss in section 4.2.1, this procedure results in a renormalized Hamiltonian with terms weighted by the corresponding doping-dependent Gutzwiller renormalization factors (see also section 3.1).

We then perform a mean-field decoupling for the renormalized Hamiltonian, focusing on hopping amplitudes $\tilde{\xi}_r \equiv \sum_{\sigma} \langle c_{i\sigma}^{\dagger} c_{i+r\sigma} \rangle_{\Psi_0}$ and pairing amplitudes $\tilde{\Delta}_r \equiv \langle c_{i\uparrow}^{\dagger} c_{i+r\downarrow}^{\dagger} - c_{i\downarrow}^{\dagger} c_{i+r\uparrow}^{\dagger} \rangle_{\Psi_0}$. In this way, we find self-consistent gap equations for the mean-field amplitudes (see section 4.2.2).

Solving the gap equations provides us with the mean-field ground state $|\Psi_0\rangle$ of the renormalized t - J Hamiltonian in the ‘pre-projected’ Hilbert space. Once $|\Psi_0\rangle$ is known, we can construct the Gutzwiller projected state $|\Psi\rangle = P_G |\Psi_0\rangle$, which then provides an approximate wave function for ground state of the projected t - J Hamiltonian. We can control the RMFT by using $|\Psi\rangle$ as a projected trial wave function within the VMC technique (see section 5). Thus, the above scheme provides a consistent framework to study Gutzwiller projected wave functions by a combination of RMFT and VMC methods.

The projected wave function $|\Psi\rangle$ allows for the calculation of relevant physical quantities as well as for the definition of excited states within the t - J model. To determine observables within the Hubbard Hamiltonian, we can employ the re-transformed wave function $e^{-iS} |\Psi\rangle$ for the calculation of expectation values. We discuss this approach in section 4.3.

4.2. Derivation of the RMFT gap equations

In this section we review the work of Zhang *et al.* [20] and develop a RMFT for the t - J model based on the Gutzwiller renormalization scheme ($\hat{=}$ GA, see

section 3.1). To illustrate the RMFT, we start with the simplest form of the t - J Hamiltonian,

$$H_{t-J} = P_G \left[-t \sum_{\langle i,j \rangle, \sigma} (c_{i,\sigma}^\dagger c_{j,\sigma} + c_{j,\sigma}^\dagger c_{i,\sigma}) + J \sum_{\langle i,j \rangle} \mathbf{S}_i \mathbf{S}_j \right] P_G. \quad (90)$$

We restrict ourselves to nearest-neighbour hopping t and a superexchange interaction J . We neglect any further hopping parameters as well as additional contributions in the Hamiltonian such as the density–density term and the correlated hopping terms, see equation (6). The effects of such extensions are discussed in section 4.3, where we consider an RMFT for the Hubbard model, including next-nearest-neighbour hopping matrix elements.

4.2.1. Derivation of the renormalized t - J Hamiltonian. Two steps are necessary to obtain explicit analytic expressions for the ground state of the t - J model (90) for various doping levels x , where $x = 1 - n$. The first is the GA, where the effects of the projection P_G are taken into account by appropriate renormalization factors. We search for a Gutzwiller projected state $P_G|\Psi_0\rangle$ that minimizes the energy expectation value,

$$\begin{aligned} E_0 &= \frac{\langle \Psi_0 | P_G H_{t-J} P_G | \Psi_0 \rangle}{\langle \Psi_0 | P_G P_G | \Psi_0 \rangle} \\ &= -t \sum_{\langle i,j \rangle, \sigma} \frac{\langle \Psi_0 | P_G (c_{i,\sigma}^\dagger c_{j,\sigma} + c_{j,\sigma}^\dagger c_{i,\sigma}) P_G | \Psi_0 \rangle}{\langle \Psi_0 | P_G P_G | \Psi_0 \rangle} + J \sum_{\langle i,j \rangle} \frac{\langle \Psi_0 | P_G \mathbf{S}_i \mathbf{S}_j P_G | \Psi_0 \rangle}{\langle \Psi_0 | P_G P_G | \Psi_0 \rangle}. \end{aligned} \quad (91)$$

By invoking a GA for (91), we get rid of the projection operator P_G and obtain

$$E_0 \approx -g_t t \sum_{\langle i,j \rangle, \sigma} \frac{\langle \Psi_0 | (c_{i,\sigma}^\dagger c_{j,\sigma} + c_{j,\sigma}^\dagger c_{i,\sigma}) | \Psi_0 \rangle}{\langle \Psi_0 | \Psi_0 \rangle} + g_S J \sum_{\langle i,j \rangle} \frac{\langle \Psi_0 | \mathbf{S}_i \mathbf{S}_j | \Psi_0 \rangle}{\langle \Psi_0 | \Psi_0 \rangle}. \quad (92)$$

The GA for the hopping term (the first term in (92)) has a renormalization factor, $g_t = (1 - n)/(1 - n/2)$, which was derived in the previous section, see equation (37). For the superexchange term (the second term in (92)), the renormalization factor is $g_S = 1/(1 - n/2)^2$, where we assume a homogeneous state without any sublattice magnetization, see (50).

We may now determine the variational ground state by searching for the state $|\Psi_0\rangle$ that minimizes the renormalized t - J Hamiltonian, \tilde{H}_{t-J} , defined as

$$\tilde{H}_{t-J} = -g_t t \sum_{\langle i,j \rangle, \sigma} (c_{i,\sigma}^\dagger c_{j,\sigma} + c_{j,\sigma}^\dagger c_{i,\sigma}) + g_S J \sum_{\langle i,j \rangle} \mathbf{S}_i \mathbf{S}_j. \quad (93)$$

Once $|\Psi_0\rangle$ is known, we may consider the projected state, $P_G|\Psi_0\rangle$, as a trial ground state of H_{t-J} .

4.2.2. Mean-field decoupling of the renormalized Hamiltonian. The next step in the derivation of the RMFT (see section 4.1) is the realization that \tilde{H}_{t-J} allows for several types of molecular fields [7, 20]: for purposes of simplification, we only concentrate on the singlet pairing amplitude,

$$\tilde{\Delta}_r \equiv \langle c_{i\uparrow}^\dagger c_{i+r\downarrow}^\dagger - c_{i\downarrow}^\dagger c_{i+r\uparrow}^\dagger \rangle_{\Psi_0}, \quad (94)$$

and the hopping amplitude,

$$\tilde{\xi}_r \equiv \sum_{\sigma} \langle c_{i\sigma}^{\dagger} c_{i+r\sigma} \rangle_{\Psi_0}, \quad (95)$$

where $r = \hat{x}, \hat{y} \hat{=} (1, 0), (0, 1)$ connects nearest-neighbour sites. This decoupling scheme of the renormalized Hamiltonian leads to a BCS ground state

$$|\Psi_0\rangle = \prod_{\mathbf{k}} (u_{\mathbf{k}} + v_{\mathbf{k}} c_{\mathbf{k}\uparrow}^{\dagger} c_{-\mathbf{k}\downarrow}^{\dagger}) |0\rangle, \quad (96)$$

with

$$v_{\mathbf{k}}^2 = \frac{1}{2} \left(1 - \frac{\xi_{\mathbf{k}}}{E_{\mathbf{k}}} \right), \quad (97)$$

and $u_{\mathbf{k}}^2 = 1 - v_{\mathbf{k}}^2$. The resulting gap equations are

$$\tilde{\Delta}_r = 1/L \sum_{\mathbf{k}} \cos(\mathbf{k} r) \Delta_{\mathbf{k}} / E_{\mathbf{k}}, \quad (98)$$

$$\tilde{\xi}_r = -1/L \sum_{\mathbf{k}} \cos(\mathbf{k} r) \xi_{\mathbf{k}} / E_{\mathbf{k}}, \quad (99)$$

together with the condition, $x = 1/L \sum_{\mathbf{k}} \xi_{\mathbf{k}} / E_{\mathbf{k}}$, for the hole-doping concentration. The dispersion of the mean-field excitations is given by $E_{\mathbf{k}} = \sqrt{\tilde{\xi}_{\mathbf{k}}^2 + \tilde{\Delta}_{\mathbf{k}}^2}$, where

$$\Delta_{\mathbf{k}} = \frac{3g_S J}{4} (\tilde{\Delta}_x \cos k_x + \tilde{\Delta}_y \cos k_y), \quad (100)$$

$$\xi_{\mathbf{k}} = - \left(2g_I t + \frac{3g_S J}{4} \tilde{\xi}_x \right) \cos k_x - \left(2g_I t + \frac{3g_S J}{4} \tilde{\xi}_y \right) \cos k_y - \mu. \quad (101)$$

Equation (98) resembles the usual BCS gap equation, except that we consider independent pairing along the x and the y directions. Together with (99), we have four coupled gap equations (for $\tilde{\Delta}_x$, $\tilde{\Delta}_y$, $\tilde{\xi}_x$, $\tilde{\xi}_y$), which must be solved self-consistently. The $\Delta_{\mathbf{k}}$ is obviously related to pairing in the state $|\Psi_0\rangle$; however, it is not identical to the superconducting order parameter in $P_G |\Psi_0\rangle$ as shown below. The $\xi_{\mathbf{k}}$ becomes the renormalized dispersion in the absence of pairing and includes a chemical potential μ to regulate the particle density.

4.2.3. Solutions of the RMFT gap equations. The gap equation can be solved numerically. We present results obtained for $J/t = \frac{1}{3}$, which is a reasonable choice for HTSCs. However, we emphasize that the results presented below are not sensitive to this particular choice of J , i.e the results stay quite similar for $J/t = 0.2$ – 0.5 . We find that a d -wave pairing state is stable for $x \leq 0.35$. In this case, $\tilde{\Delta} \equiv |\tilde{\Delta}_x| = |\tilde{\Delta}_y|$ with $\tilde{\Delta}_x = -\tilde{\Delta}_y$ and $\tilde{\xi} \equiv \tilde{\xi}_x = \tilde{\xi}_y$. We illustrate the doping dependence of these quantities in figure 28. The superconducting order parameter,

$$\Phi \equiv |\langle c_{i\uparrow}^{\dagger} c_{i+\tau\downarrow}^{\dagger} - c_{i\downarrow}^{\dagger} c_{i+\tau\uparrow}^{\dagger} \rangle_{\Psi}|, \quad (102)$$

is an expectation value in the projected ground states, $|\Psi\rangle \equiv P_G |\Psi_0\rangle$, where τ is a neighbouring site. Evaluating Φ by the GA (section 3.1) one finds that Φ is renormalized as the hopping amplitude by g_I , namely $\Phi \approx g_I \tilde{\Delta}$. As illustrated in figure 28, Φ vanishes linearly near $x=0$, while $\tilde{\Delta}$ continuously increases towards half-filling.

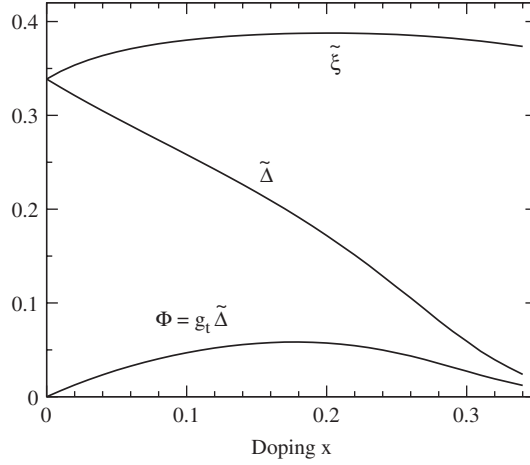


Figure 28. Doping dependence of the d -wave pairing amplitude $\tilde{\Delta}$, the hopping amplitude $\tilde{\xi}$ and the superconducting order parameter Φ (see (102)) in the d -wave ground state for the t - J model (90) with $J = t/3$. The results were obtained self-consistently by solving the RMFT gap equations.

These results are in good agreement with VMC results [21, 117, 147] and the experimentally observed T_c for the d -wave pairing in the HTSCs.

For the renormalized Hamiltonian, the $E_{\mathbf{k}}$ corresponds to the dispersion of the Bogoliubov QPs, $|\Psi_{\mathbf{k},0}^\sigma\rangle \equiv \gamma_{\mathbf{k}\sigma}^\dagger |\Psi_0\rangle$, with $\sigma = \uparrow, \downarrow$, where the corresponding Bogoliubov operators are defined by $\gamma_{-\mathbf{k}\downarrow}^\dagger \equiv u_{\mathbf{k}} c_{-\mathbf{k}\downarrow}^\dagger + v_{\mathbf{k}} c_{\mathbf{k}\uparrow}$ and $\gamma_{\mathbf{k}\uparrow}^\dagger \equiv u_{\mathbf{k}} c_{\mathbf{k}\uparrow}^\dagger - v_{\mathbf{k}} c_{-\mathbf{k}\downarrow}$, respectively. However, $E_{\mathbf{k}}$ also describes the excitation energy of the corresponding projected Gutzwiller-Bogoliubov QPs,

$$|\Psi_{\mathbf{k}\sigma}\rangle \equiv P_G |\Psi_{\mathbf{k},0}^\sigma\rangle = P_G \gamma_{\mathbf{k}\sigma}^\dagger |\Psi_0\rangle. \quad (103)$$

To see why, one evaluates the expectation value of the t - J Hamiltonian with respect to $|\Psi_{\mathbf{k}\sigma}\rangle$. As $|\Psi_{\mathbf{k}\sigma}\rangle = P_G |\Psi_{\mathbf{k},0}^\sigma\rangle$ is renormalized exactly as $|\Psi\rangle = P_G |\Psi_0\rangle$, we recover the renormalized Hamiltonian \tilde{H}_{t-J} , equation (93), by invoking a GA. The state $|\Psi_{\mathbf{k},0}^\sigma\rangle$ is now acting onto \tilde{H}_{t-J} , yielding in mean-field decoupling a Bogoliubov QP with excitation energy $E_{\mathbf{k}}$. Therefore, the gap $\Delta_{\mathbf{k}}$ in $E_{\mathbf{k}} = \sqrt{\xi_{\mathbf{k}}^2 + \Delta_{\mathbf{k}}^2}$ corresponds to the QP gap in the projected superconducting state and is directly proportional to the mean-field amplitude $\tilde{\Delta}$ in figure 28. We note that RMFT [20] correctly reported the doping dependence of the d -wave gap, i.e. an increasing gap with decreasing doping, well before this behaviour was experimentally established.

The above calculations follow the original work of Zhang *et al.* [20] Note that the results are restricted to a homogeneous and non-magnetic phase. Therefore, the results cannot adequately describe the antiferromagnetic region of the phase diagram near half-filling as well as inhomogeneous phases observed in HTSCs. However, we emphasize that as the Gutzwiller-RVB is a variational mean-field theory, it can be extended to study such phases as well. In the following sections, we describe some attempts made in this direction that provide a more detailed description of the phase diagram of the HTSCs.

Table 2. Examples of degenerate states of the renormalized mean-field Hamiltonian at half-filling, see also [20]. The general constant $C=0.479$ is determined by the RMFT gap equations (98) and (99).

d -wave pairing	$\tilde{\Delta}_x = -\tilde{\Delta}_y = \tilde{\xi}_x = \tilde{\xi}_y = C/\sqrt{2}$
d -wave density matrix*	$\tilde{\Delta}_x = \tilde{\Delta}_y = \tilde{\xi}_x = -\tilde{\xi}_y = C/\sqrt{2}$
Chiral state	$\tilde{\Delta}_x = -i\tilde{\Delta}_y = C, \tilde{\xi}_x = \tilde{\xi}_y = 0$
Anisotropic state	$\tilde{\Delta}_x = \tilde{\xi}_y = C, \tilde{\Delta}_y = \tilde{\xi}_x = 0$

*Note that the d -wave density matrix is not the d -density wave order discussed in [66].

4.2.4. Local SU(2) symmetry in the half-filled limit. In the limit of half-filling, the kinetic energy renormalizes to zero, because $g_t \rightarrow 0$ as $x \rightarrow 0$. The t - J model reduces to the antiferromagnetic Heisenberg model, which is conserved under local SU(2) gauge transformations [20, 154],

$$c_{i\uparrow}^\dagger \rightarrow \alpha_i c_{i\uparrow}^\dagger + \beta_i c_{i\downarrow}, \quad c_{i\downarrow} \rightarrow -\beta_i^* c_{i\uparrow}^\dagger + \alpha_i^* c_{i\downarrow}, \quad (104)$$

where $\alpha_i \alpha_i^* + \beta_i \beta_i^* = 1$. The invariance of the Hamiltonian is due the spin operator S_i , which is invariant under SU(2) transformations, as can be proved by applying (104) to the operators S_i^\pm and S_i^z . For S_i^+ , we find

$$\begin{aligned} S_i^+ = c_{i\uparrow}^\dagger c_{i\downarrow} &\rightarrow (\alpha_i c_{i\uparrow}^\dagger + \beta_i c_{i\downarrow})(-\beta_i^* c_{i\uparrow}^\dagger + \alpha_i^* c_{i\downarrow}) \\ &\rightarrow \alpha_i \alpha_i^* S_i^+ + \beta_i \beta_i^* S_i^+ = S_i^+. \end{aligned} \quad (105)$$

The invariance of S_i^- and S_i^z under (104) can be shown analogously.

Owing to the local SU(2) gauge symmetry, the renormalized mean-field Hamiltonian has a large degeneracy in the representation of ground states at half-filling, as may be seen by transforming the mean-field amplitudes $\tilde{\Delta}_r$ and $\tilde{\xi}_r$, (94) and (95), under (104). Some of the resulting (degenerate) states, which are related to each other by SU(2) transformations, are summarized in table 2. Another example among the degenerate states in the SU(2) manifold is the staggered π -flux state [154],

$$\xi_{ij} = |\xi_0|^2 \exp\left(i(-1)^{i_x+i_y} \frac{\pi}{4}\right), \quad (106)$$

with a complex hopping amplitude $\xi_{ij} \equiv \langle c_{i\sigma}^\dagger c_{j\sigma} \rangle_0$, but a vanishing pairing amplitude $\Delta_{ij} \equiv \langle c_{i\uparrow}^\dagger c_{i\downarrow} \rangle_0 = 0$.

It is important to note that above degeneracy is not true in terms of the projected wave function, as it only results from using an under-determined representation. In other words, the states that are degenerate are the unprojected states $|\Psi_0\rangle$, but not the physical states $P_G|\Psi_0\rangle$ (see [20]). Therefore, the entire set of degenerate ground states in the renormalized mean-field Hamiltonian correspond (modulo a trivial phase factor) to a single projected state; for a proof see [20].

All states listed in the table 2 and (106) have the same superexchange energy, even at finite doping, owing to the SU(2) invariance of this term. However, the kinetic energy T (see (8)) and the three-site term H_3 (see (10)), which only vanish at half-filling, are not invariant under the SU(2) transformation (104). Therefore, the

degeneracy in $|\Psi_0\rangle$ is lifted at finite doping, where the d -wave pairing state is selected owing to its lower kinetic energy.

The SU(2) gauge symmetry of the superexchange term led to the speculation that at finite doping, when the degeneracy is lifted, some among the ‘degenerate’ states may compete with the d -wave state (also one of the degenerated states at half-filling). In particular, it was argued that staggered flux states could serve as a ‘competing’ or as a ‘normal’ states in the underdoped regime of the HTSCs [19, 142]. In addition to this competing order scenario, a spin-charge locking mechanism [113] resting on the presence of the SU(2) gauge symmetry at half-filling was suggested. The consequence of the degeneracy in the unprojected mean-field ground states at half-filling and its possible relationship with competing or coexisting order are not yet fully understood.

4.3. RMFT for the Hubbard model and application to HTSCs

The RMFT presented so far can be improved by considering all terms contributing to the t - J Hamiltonian (6), i.e. including the density–density term (9) as well as the correlated hopping terms (10). The inclusion of these terms is also necessary if one were to use RMFT for the Hubbard Hamiltonian, because the unitary transformation $H_{t-J} = P_G e^{iS} H e^{-iS} P_G$ (discussed in section 2.4) between the Hubbard and t - J Hamiltonians lead to these terms. Physical quantities for the Hubbard model can be evaluated by considering expectation values in the re-transformed wave function $e^{-iS} P_G |\Psi_0\rangle$ [7]. In the following we use this ansatz to study the superconducting order parameter. We include next-nearest-neighbour hopping (t') in the Hubbard Hamiltonian in order to allow for quantitative comparison with experimental data for the HTSCs.

4.3.1. Generalized gap equations for the strong coupling limit. We obtain the RMFT gap equations for the Hubbard model in the strong coupling limit by considering the corresponding effective Hamiltonian, i.e. the full t - J Hamiltonian. The gap equations for this t - J Hamiltonian, which includes all terms from equation (6), can then be derived in the same way as described in the previous section.

First we invoke the GA to obtain the renormalized Hamiltonian for (6). We note that all (nearest as well as further neighbours) hopping terms are renormalized by $g_t = (1-n)/(1-n/2)$ and all superexchange terms by $g_S = 1/(1-n/2)^2$. As the density–density term commutes with the projection operator P_G , it does not pick up any Gutzwiller renormalization factor. The new correlated hopping terms, equation (10), are of the following form

$$\begin{aligned} \langle c_{i+\tau_1, \uparrow}^\dagger c_{i, \downarrow}^\dagger c_{i, \downarrow} c_{i+\tau_2, \uparrow} \rangle_{P_G \Psi_0} &\approx g_3 \langle c_{i+\tau_1, \uparrow}^\dagger n_{i, \downarrow} (1 - n_{i, \uparrow}) c_{i+\tau_2, \uparrow} \rangle_{\Psi_0}, \\ \langle c_{i+\tau_1, \downarrow}^\dagger c_{i, \uparrow}^\dagger c_{i, \downarrow} c_{i+\tau_2, \uparrow} \rangle_{P_G \Psi_0} &\approx g_3 \langle c_{i+\tau_1, \downarrow}^\dagger c_{i, \uparrow}^\dagger c_{i, \downarrow} c_{i+\tau_2, \uparrow} \rangle_{\Psi_0}, \end{aligned} \quad (107)$$

involve three sites (i , $i+\tau_1$ and $i+\tau_2$) and are renormalized by a factor $g_3 = (1-n)/(1-n/2)^2$. For a derivation of the GA for the correlated hopping terms we refer to the appendix of [5].

Next we decouple the resulting renormalized Hamiltonian by the same scheme discussed in the previous section, obtaining therefore the same gap equations, (98) and (99), as before. However, the dispersion relation, $E_{\mathbf{k}} = \sqrt{\xi_{\mathbf{k}}^2 + \Delta_{\mathbf{k}}^2}$, with [7],

$$\begin{aligned} \xi_{\mathbf{k}} = & - \left(2g_t t + J \frac{\tilde{\xi}}{4} x_1 + J_3 \frac{\tilde{\xi}}{4} x_2 \right) (\cos k_x + \cos k_y) \\ & - \left(2g_t t' + J' \frac{\tilde{\xi}}{4} x_1 + J_3 \frac{\tilde{\xi}}{4} x_2 \right) 2 \cos k_x \cos k_y \\ & - x_D \sum_{\tau_1 \neq \tau_2} \frac{t_{\tau_1} t_{\tau_2}}{4U} \cos[\mathbf{k}(\tau_1 - \tau_2)] - \mu, \end{aligned} \quad (108)$$

$$\Delta_{\mathbf{k}} = J \frac{\tilde{\Delta}}{4} [3g_s + 1 - (3+x)g_3] (\cos k_x - \cos k_y), \quad (109)$$

incorporates the effects of further neighbour hopping and correlated hopping terms. These expressions for $\xi_{\mathbf{k}}$ and $\Delta_{\mathbf{k}}$ are valid for $\tilde{\Delta} \equiv |\tilde{\Delta}_x| = |\tilde{\Delta}_y|$, $\tilde{\Delta}_x = -\tilde{\Delta}_y$, $\tilde{\xi} \equiv \tilde{\xi}_x = \tilde{\xi}_y$, i.e. for the d -wave pairing state, which is the most stable solution of the gap equations (98) and (99). Note that we defined new hopping amplitudes for next nearest neighbours, $\tilde{\xi} \equiv \tilde{\xi}_{x+y} = \tilde{\xi}_{x-y}$. The last sum in (108) is a sum over all pairs of non-identical neighbouring sites τ_1 and τ_2 , where t_{τ_1} and t_{τ_2} are nearest- and next-nearest-neighbour hopping terms. We defined, $J = 4t^2/U$, $J_3 = 4t't/U$ and $J' = 4t'^2/U$ and abbreviated $x_1 = 3g_s - 1 + 3(3-x)g_3$, $x_2 = 4(3-x)g_3$ and $x_D = (1-x^2)g_3$ in (108).

As in section 4.2, the ground state $|\Psi_0\rangle$ of the renormalized t - J Hamiltonian results from above equations. By including a projection operator P_G in the wave function we obtain $P_G|\Psi_0\rangle$, which corresponds to a variational wave function for the ground state of the t - J Hamiltonian in the fully projected Hilbert space. Invoking the canonical transformation e^{-iS} then provides an approximate ground state $e^{-iS}P_G|\Psi_0\rangle$ for the Hubbard model.

4.3.2. Results from the generalized gap equations. For a comparison with experiments, we follow [7] and consider a ratio $t'/t = -\frac{1}{4}$ between next-nearest- and nearest-neighbour hopping amplitudes, a value used widely in the modelling of the band structure of various HTSCs [57]. Furthermore, we choose an on-site repulsion $U = 12t$, i.e. we work in the strong coupling regime $U \gg t, t'$, where the transformation from the Hubbard to the t - J model is valid approximately. The above choice of the model parameters reduces the number of free parameters to one energy scale, $t \approx 300$ – 500 meV, for the HTSCs.

In figure 29 we show the doping dependence of the superconducting gap, $|\Delta_{\mathbf{k}}|$ at $\mathbf{k} = (\pi, 0)$, within RMFT, which resembles experimental observations quite well. However, the magnitude of the gap is overestimated by a factor of about two (see scaling factor $\alpha = \frac{1}{2}$ in figure 29) within mean-field theory. This overall mismatch is attributed to the fact that dynamical [155] and long-range correlations are neglected within RMFT, which is based on a local and static molecular-field approximation.

As mentioned in section 4.2.3, the superconducting gap is not identical to the true superconducting order parameter, $\Phi \equiv |\langle c_{i\uparrow}^\dagger c_{i+\tau\downarrow}^\dagger - c_{i\downarrow}^\dagger c_{i+\tau\uparrow}^\dagger \rangle|$ (see [20, 21]). Here, we determine the expectation value of Φ within the re-transformed wave

function, $e^{-iS}P_G|\Psi_0\rangle$. Following section 2.4, we evaluate the canonical transformation e^{-iS} in order $\mathcal{O}(t/U)$. Doing so provides systematic t/U corrections to the result from section 4.2.3, where we used the wave function $P_G|\Psi_0\rangle$ in calculating the expectation value of the superconducting order parameter.

The calculations for the expectation value of a general observable \hat{O} within the Hubbard model are summarized by

$$\langle \hat{O} \rangle_{e^{-iS}P_G\Psi_0} = \langle e^{iS}\hat{O}e^{-iS} \rangle_{P_G\Psi_0} \quad (110a)$$

$$\approx \langle \hat{O} + i[S, \hat{O}] \rangle_{P_G\Psi_0}, \quad (110b)$$

where the last step corresponds to the evaluation of e^{-iS} in order $\mathcal{O}(t/U)$; compare with section 2.4. Note that (110b) corresponds to an expectation value of the operator $O + i[S, \hat{O}]$ in the projected state $P_G|\Psi_0\rangle$. We can therefore use a generalized GA by invoking the counting arguments given in section 3.1.

Setting $\hat{O} = c_{i\uparrow}^\dagger c_{i+\tau\downarrow}^\dagger - c_{i\downarrow}^\dagger c_{i+\tau\uparrow}^\dagger$, the superconducting order parameter Φ for the Hubbard model can be calculated using by above scheme. One finds

$$\Phi \approx g_t \tilde{\Delta} + \frac{t}{U} g_3 (6 - x) \tilde{\Delta} \tilde{\xi}. \quad (111)$$

In deriving (111) we considered $t' \approx 0$ within S , for simplicity, because $|t'| \ll |t|$. As shown in figure 29, Φ vanishes as $x \rightarrow 0$, and the t/U corrections do not qualitatively change the result of Zhang *et al.* [20] near half-filling. We emphasize that the above procedure can be used to calculate the expectation value of any observable and provides a systematic way to study the Hubbard model in the strong coupling limit.

Next we consider the nature of the low-lying excitations, i.e. the QPs created at the nodal point, $k_F \equiv k_{F,x} = k_{F,y}$. The nodal dispersion around k_F is characterized by the velocity, v_F , which directly influences a number of experimentally accessible quantities. The Fermi velocity v_F can be directly calculated by the gradient of $\xi_{\mathbf{k}}$

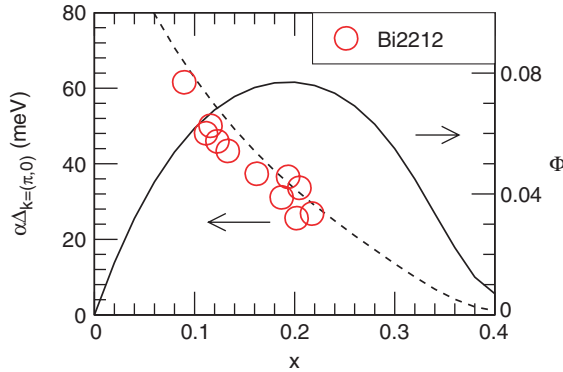


Figure 29. Doping dependence of (solid curve, right scale) the superconducting order parameter, Φ , and (dashed curve, left scale) the superconducting gap, $|\Delta_{\mathbf{k}}|$, at $\mathbf{k} = (\pi, 0)$ for $t = 300$ meV. The RMFT superconducting gap is scaled by a factor $\alpha = \frac{1}{2}$ for comparison with experimental data (circles, Bi2122 [24]). From [7].

along the direction $(0, 0) \rightarrow (\pi, \pi)$ within RMFT. The results obtained by using $\xi_{\mathbf{k}}$ from equation (108) are presented in figure 30 (for $t=0.3, 0.4$ and 0.5 eV and $a_0=4$ Å). Edegger *et al.* [7] also found that the theoretically v_F is well approximated by the formula,

$$v_F/a_0 \approx \sqrt{2} \sin k_F \left[2g_t(t + 2t' \cos k_F) + x_1 \frac{J}{4} \tilde{\xi} \right]. \quad (112)$$

where J' and J'' are set to zero for simplicity. As we discuss later, the effective values of J' and J'' within the GA become zero at half-filling. So, ignoring their effect on the dispersion modifies the result only weakly. As seen in figure 30, v_F increases with x , but remains finite as $x \rightarrow 0$. In addition, we can infer from (112) that the energy scale of the nodal velocity at $x=0$ is determined by J , i.e. $v_F/(a_0 J) \approx \sqrt{2} \sin(k_F) \frac{11}{4} \tilde{\xi} \approx 1.5$ (with $\tilde{\xi} \approx 0.38$ and $k_F \approx \pi/2$). The observed doping dependence stems from the effects of the Gutzwiller projection P_G . As x increases, holes gain kinetic energy by direct hopping, namely, g_t increases with doping; but g_s decreases, leading to the doping dependence of v_F seen in figure 30. Note, that the RMFT results presented in figure 30 are absolute in value. No rescaling has been made for comparison with the experiments, in contrast to the results for the gap $|\Delta_{\mathbf{k}=(\pi, \pi)}|$ presented in figure 29.

The above results are in agreement with the VMC results of Paramekanti *et al.* [21, 117], who extracted v_F from the discontinuity of the first moment of the spectral function in the repulsive U Hubbard model (see also section 5.3.2), and of Yunoki *et al.* [146], who obtained v_F from the QP dispersion in the t – J model (see also section 7.2). These results also yield a good fit to the ARPES data [39, 156–159], as illustrated in figure 30. We note that the doping dependence of v_F in the severely underdoped regime remains to be settled experimentally. While some groups report a

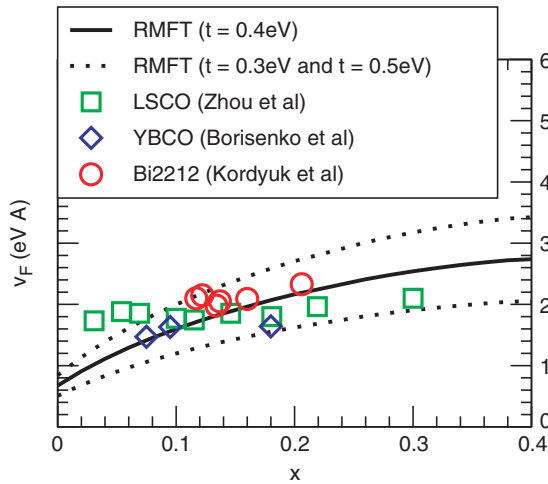


Figure 30. Doping dependence of the Fermi velocity, v_F . The RMFT results are compared with experimental data from Zhou *et al.* [39], Borisenko *et al.* [156] and Kordyuk *et al.* [157]. Reprinted with permission from [7] © 2006 by the American Physical Society.

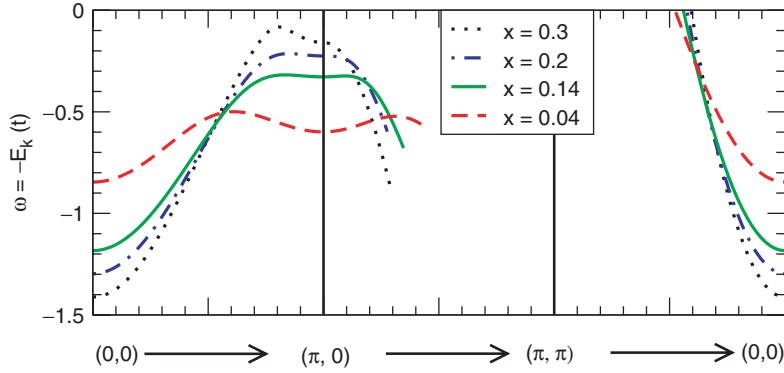


Figure 31. Energy dispersion, $\omega = -E_{\mathbf{k}} = \sqrt{\xi_{\mathbf{k}} + \Delta_{\mathbf{k}}}$, of the Gutzwiller–Bogoliubov QP for different doping x . Reprinted with permission from [7] © 2006 by the American Physical Society.

nearly constant Fermi velocity (see the data for LSCO in figure 30), others observe a slight increase with doping (see the data for YBCO and Bi2212 in figure 30). We further emphasize that the energy scales t and J might be extracted from the ARPES data in v_F , whenever data with high accuracy becomes available. By using $\tilde{\xi} \approx 0.38$ and setting k_F and the ratio t'/t to the experimentally observed values, t and J can be fitted by (112). In addition, the RMFT calculations find that the nodal properties remain essentially unchanged when $\tilde{\Delta}$ is set to zero, i.e. the doping dependence of v_F results from the vicinity of the RVB state to a Mott insulator, rather than the occurrence of superconductivity itself.

In figure 31, we present the energy dispersion, $\omega = -E_{\mathbf{k}}$, of the Gutzwiller–Bogoliubov QP along the directions $(0,0) \rightarrow (\pi,0)$, $(\pi,0) \rightarrow (\pi,\pi)$ and $(\pi,\pi) \rightarrow (0,0)$ for different doping levels x . The dispersion is flattened when approaching half-filling and the gap around $(\pi,0)$ becomes large. We emphasize that these RMFT calculations adequately describe only the low-energy sector of the HTSCs and do not seek to explain the ‘kink’ at higher energies [39, 156–159].

Equations (108) and (109) can also be used to study the effects of t' on the magnitude of the superconducting order parameter Φ . Figure 32 shows the value of Φ at optimal doping as a function of the ratio t'/t in the bare non-interacting dispersion. We observe a maximum at about $t'/t = -0.35$ depending slightly on whether we set $^\dagger t'' = 0$ or $t'' = -t'/2$. This observation is in agreement with band-structure calculations [160] where it is found empirically that compounds with ratio $t'/t \approx -0.1$ in the dispersion (determined from band-structure calculations) have smaller T_c (corresponds to smaller Φ) than compounds with a ratio $t'/t \approx -0.35$. The RMFT calculations in figure 32 also match VMC results of Shih *et al.* [161], which we discuss in more detail in section 5.2.2.

[†]We note that the inclusion of $t'' = -t'/2$ into the bare dispersion is sometimes used to get a better fit with band-structure calculations and ARPES data.

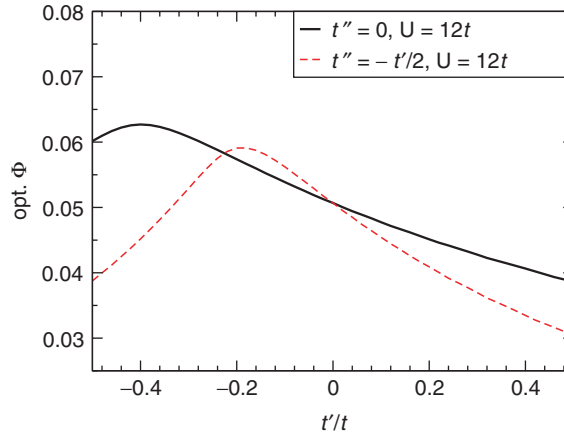


Figure 32. The magnitude of the optimal superconducting order parameter (opt. Φ) as a function of the ratio t'/t as obtained in the RMFT calculations for the Hubbard model. Here opt. Φ provides the value of Φ at optimal doping, i.e. the maximal value of Φ for this particular set of model parameters (t'/t , $U = 12t$). The dashed curve shows calculations, where third-nearest-neighbour hopping has been taken into account into dispersion by setting $t'' = -t'/2$.

To summarize, the calculational scheme we described above presents a systematic way to study the Hubbard model in the strong coupling limit. It is based on the validity of the t – J model as an effective Hamiltonian (in the large U limit) and on determining expectation values within the re-transformed trial wave function, $e^{-iS}P_G|\Psi_0\rangle$; a scheme that can be extended to excited states as described in section 6 (see also [7]).

4.4. Possible extensions and further applications

4.4.1. Incorporation of antiferromagnetism. The incorporation of antiferromagnetism is an example of a possible extension of the RMFT. In order to describe an antiferromagnet with finite sublattice magnetization m , we have to allow for an additional degree of freedom in the wave function. When deriving the corresponding gap equation we must keep in mind that the antiferromagnetic correlation affects the GA as discussed in section 3.1. However, Himeda and Ogata [102] showed by VMC calculations that even the formulas from section 3.1 do not adequately describe all aspects in a magnetic ordered state. They determined effective Gutzwiller renormalization factors by comparing the numerically obtained expectation values in the projected state with the respective mean-field values before projection. It was found that the z -component of the Gutzwiller renormalization factor g_s^z is enhanced compared with those of the xy -component g_s^\pm .

Ogata and Himeda [107] argued that the discrepancies stem from spatial correlations neglected by the GA. They derived extended Gutzwiller renormalization factors by considering a cluster around the sites i and j to incorporate further inter-site correlations. Applying these renormalization factors and solving the gap equations

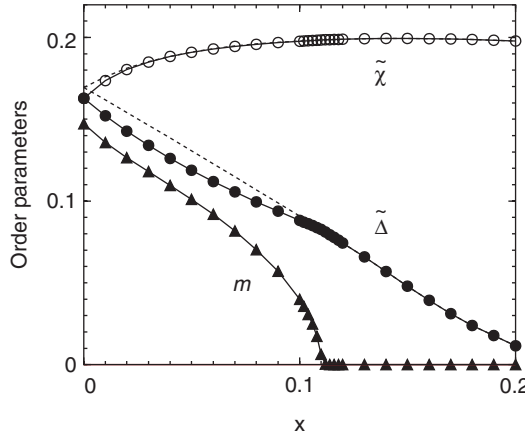


Figure 33. RMFT calculations including antiferromagnetism from Ogata and Himeda [107]. The self-consistent parameters $\tilde{\Delta}$ (pairing amplitude), $\tilde{\chi}$ (hopping amplitude) and m (staggered magnetization) are shown as a function of the doping rate $x = 1 - n$ for $J/t = 0.3$ and $t' = J' = 0$. The dashed curves represent the results when the antiferromagnetic order is suppressed, i.e. m is fixed to zero. Reprinted with permission from [107] © 2003 by the Institute of Pure and Applied Physics.

including antiferromagnetism yields the results of figure 33. We see that for doping, $\delta < 0.1$, long-range antiferromagnetic order coexists with superconductivity. For higher doping the magnetization m vanishes and solely the superconducting order remains. This result is obtained neglecting the next-nearest-neighbour hopping ($t' = 0$) and agrees with previous VMC results [102–105]. We note that the extended Gutzwiller renormalization factors of Ogata and Himeda are essential for reproducing the VMC calculations. However, figure 33 does not quantitatively agree with the experimental phase diagram of hole-doped cuprates, where antiferromagnetism disappears at about 3–5% doping. A better match may be obtained by considering the effects of t' as done in VMC [106] and quantum cluster studies [162, 163].

4.4.2. Applications to inhomogeneous systems. The RMFT described has also been used to study inhomogeneous phases such as stripes and checkerboard charge order [98–101], vortex cores [111, 112] and magnetic and non-magnetic impurities [108–110]. These investigations throw light on the interplay between antiferromagnetic correlations, d -wave superconductivity and charge order and can be compared with STM data.

However, such studies require an unrestricted Hartree–Fock treatment of the renormalized t – J Hamiltonian (93), i.e. local expectation values such as $\tilde{\Delta}_{ij} \equiv \langle c_{i\uparrow}^\dagger c_{j\downarrow}^\dagger \rangle_{\Psi_0}$ and $\tilde{\xi}_{ij\sigma} \equiv \langle c_{i\sigma}^\dagger c_{j\sigma} \rangle_{\Psi_0}$ must be considered independently for each bond [164]. Furthermore, the local charge densities $n_{i\sigma}$ generally differ from site to site and thus the Gutzwiller renormalization factors of the renormalized Hamiltonian depend on the site indices i and j (g_t^{ij} , g_s^{ij}). Special attention must be paid when deriving these Gutzwiller renormalization factors, because the local charge densities can differ between the projected and unprojected state (see the discussion in section 3.1). For inhomogeneous systems the RMFT gap equations

generalize to the so-called Bogoliubov–de Gennes equations, which must then be solved self-consistently.

The investigation of charge modulations within above framework [98–101] provides an understanding of the 4×4 checkerboard patterns seen in the STM data of the HTSCs. These studies neglect long-range antiferromagnetism and assume $\tilde{\xi}_{ij} = \tilde{\xi}_{ij\uparrow} = \tilde{\xi}_{ij\downarrow}$ and $n_{i\uparrow} = n_{i\downarrow}$. This is a reasonable assumption since the authors concentrated on doping levels where antiferromagnetism is not observed experimentally. The renormalized mean-field Hamiltonian can then be written as [100]

$$H_{\text{MF}} = -t \sum_{\langle ij \rangle \sigma} g_t^{ij} (c_{i,\sigma}^\dagger c_{j,\sigma} + \text{h.c.}) - \mu \sum_{i\sigma} n_{i,\sigma} - \frac{3}{4} J \sum_{\langle ij \rangle \sigma} g_S^{ij} (\tilde{\xi}_{ji} c_{i,\sigma}^\dagger c_{j,\sigma} + \text{h.c.} - |\tilde{\xi}_{ij}|^2) - \frac{3}{4} J \sum_{\langle ij \rangle \sigma} g_S^{ij} (\tilde{\Delta}_{ji} c_{i,\sigma}^\dagger c_{j,-\sigma}^\dagger + \text{h.c.} - |\tilde{\Delta}_{ij}|^2). \quad (113)$$

However, we must abandon the above constraints $\tilde{\xi}_{ij} = \tilde{\xi}_{ij\uparrow} = \tilde{\xi}_{ij\downarrow}$ and $n_{i\uparrow} = n_{i\downarrow}$ for investigations around vortex cores or impurities, where antiferromagnetic correlations are essential. Doing so and solving the Bogoliubov–de Gennes equations under an uniformly applied magnetic field shows that significant antiferromagnetic correlations develop inside vortex cores [112] in agreement with experimental observations [165–170]. Tsuchiura *et al.* [108–110] also studied the effects of magnetic and non-magnetic impurities on the local density of states in HTSCs within above approach. The results obtained resemble the STM data [46–48] quite well†. The self-consistent determination of order parameters within the renormalized Bogoliubov–de Gennes theory was also applied to study surface effects in 2D superconducting states [172, 173].

To analyse the above problems within an unrestricted Hartree–Fock theory, most authors consider a large (but finite) unit cell, which exhibits a certain charge ordering pattern or which has a vortex core or an impurity site in the middle. The corresponding renormalized Bogoliubov–de Gennes equations can then be solved by assuming a lattice of unit cells (e.g. $N_c = 20 \times 20$) and making use of Fourier transformations. While most studies use the Gutzwiller factors derived in section 3, some recent works [110, 112] use the extensions proposed by Ogata and Himeda [107] (see section 4.4.1). Finally, we note that all of these studies concentrate on the ground state properties ($T=0$). It would be very interesting to consider finite-temperature effects within a renormalized unrestricted Hartree–Fock theory and, to the best of our knowledge, such studies have not yet been carried out.

4.4.3. Gossamer superconductivity. Another class of renormalized mean-field theories considers a modified version of the Hubbard model, which includes a superexchange interaction J like in the t – J Hamiltonian. This t – J – U model was proposed by Zhang [174] to study the so-called gossamer superconductivity [175]. Here, the form of the GA, which includes finite double occupancy, must be used for the renormalized Hamiltonian [174]. The RMFT gap equations are obtained in a

†Nevertheless VMC calculations [171] for a non-magnetic impurity report some minor discrepancies to the corresponding RMFT study [110].

straightforward manner and the number of double occupancies is determined by optimizing the ground state energy. Within this approach, at half-filling, there is a first-order phase transition from a Mott insulating phase at large Coulomb repulsion U to a gossamer superconducting phase at small U . Away from half-filling the Mott insulator evolves into an RVB state, which is adiabatically connected to the gossamer superconductor [176]. Some authors follow this approach to study HTSCs [164, 176–179] while others have used it in the phenomenology of organic superconductors [92, 93].

4.4.4. Time-dependent GA. The studies discussed so far mainly focused on the superconducting state. Seibold and Lorenzana [180] considered the Hubbard model without superconducting pairing and developed a time-dependent GA analogous to the time-dependent Hartree–Fock theory. This formalism incorporates ground state correlations beyond the GA within the random phase approximation and allows for a computation of the dynamical density–density response function. The scheme successfully describes several interesting features of HTSCs, such as the dynamics of stripes [181] or the dispersion of magnetic excitations [182–184] and was recently applied to investigate checkerboard inhomogeneities [185]. It would be very useful if this scheme could be adapted to study the dynamics of a homogeneous superconducting phase.

5. VMC calculations for HTSCs: an overview

The VMC technique allows for an accurate evaluation of expectation values in Gutzwiller projected wave functions. In this section we present the technical details of the VMC method and review the variational search for the optimal ground state energy in the Hubbard and t – J model. In this context, we also discuss the coexistence of superconductivity with antiferromagnetism and flux states as well as the improvement of the trial wave function by further variational parameters and Jastrow factors. Further we consider doping-dependent features of projected wave functions and compare them with experimental findings in HTSCs. Finally, we discuss a recent numerical study dealing with the tendency towards a spontaneous breaking of the FS symmetry.

5.1. Details of the VMC method

The VMC method was first applied to the study the projected Fermi sea [116, 186], which has a fixed particle number. However, superconducting BCS wave functions $|\Psi_0\rangle$ are generally defined in a grand canonical ensemble, where the wave function shows particle number fluctuations. These particle number fluctuations are also present in the projected BCS wave function, $|\tilde{\Psi}\rangle \equiv P_G|\Psi_0\rangle$. Within the VMC scheme we have now two possibilities, we can either work with $|\tilde{\Psi}\rangle$ (grand canonical ensemble) directly [97] or we can project out the particle number fluctuations by a projector P_N that fixes the particle number and work with $|\Psi\rangle \equiv P_N|\tilde{\Psi}\rangle$ (canonical ensemble) [17]. In this review, we only present the method of Gros [17, 147], used in most recent VMC calculations, because it avoids complications due to the fluctuating

particle number. The possible discrepancies between the grand canonical and the canonical VMC scheme have been discussed in detail in section 3.2.

5.1.1. Real-space representation of the trial wave function. Before performing a VMC calculation we have to rewrite the wave function in an appropriate way. By inserting a complete set of states $\{|\alpha\rangle\}$ for the subspace that excludes double occupancy (and with a fixed particle number N), we can remove the projection operator P_N and P_G from the wave function $|\Psi\rangle$,

$$|\Psi\rangle \equiv P_N P_G |\Psi_0\rangle = \sum_{\alpha} \langle\alpha|\Psi_0\rangle |\alpha\rangle. \quad (114)$$

The most suitable choice of $|\alpha\rangle$ is given by a straightforward real-space representation in terms of fermion creation operators,

$$|\alpha\rangle = c_{\mathbf{R}_1, \uparrow}^{\dagger} \cdots c_{\mathbf{R}_{N_{\uparrow}}, \uparrow}^{\dagger} c_{\mathbf{R}_1, \downarrow}^{\dagger} \cdots c_{\mathbf{R}_{N_{\downarrow}}, \downarrow}^{\dagger} |0\rangle. \quad (115)$$

The state (115) is specified by two disjoint sets $\{\mathbf{R}_1 \dots \mathbf{R}_{N_{\uparrow}}\}$ and $\{\mathbf{R}_1 \dots \mathbf{R}_{N_{\downarrow}}\}$, which determine the positions of the up- and down-spin electrons on a finite lattice.

Next we have to calculate the overlap $\langle\alpha|\Psi_0\rangle$. To determine this quantity by a Monte Carlo calculation, we write the BCS wave function $P_N|\Psi_0\rangle$ as [15]

$$P_N|\Psi_0\rangle \equiv P_N \prod_{\mathbf{k}} (u_{\mathbf{k}} + v_{\mathbf{k}} c_{\mathbf{k}\uparrow}^{\dagger} c_{-\mathbf{k}\downarrow}^{\dagger}) |0\rangle \quad (116a)$$

$$\propto P_N \prod_{\mathbf{k}} (1 + a_{\mathbf{k}} c_{\mathbf{k}\uparrow}^{\dagger} c_{-\mathbf{k}\downarrow}^{\dagger}) |0\rangle \quad (116b)$$

$$\propto \left(\sum_{\mathbf{k}} a_{\mathbf{k}} c_{\mathbf{k}\uparrow}^{\dagger} c_{-\mathbf{k}\downarrow}^{\dagger} \right)^{N/2} |0\rangle \quad (116c)$$

$$= \left(\sum_{\mathbf{R}_{j,\downarrow}, \mathbf{R}_{j,\uparrow}} a(\mathbf{R}_{j,\downarrow} - \mathbf{R}_{j,\uparrow}) c_{\mathbf{R}_{j,\uparrow}, \uparrow}^{\dagger} c_{\mathbf{R}_{j,\downarrow}, \downarrow}^{\dagger} \right)^{N/2} |0\rangle. \quad (116d)$$

In (116b) we defined the quantity $a_{\mathbf{k}} \equiv v_{\mathbf{k}}/u_{\mathbf{k}}$, which can be written as

$$a_{\mathbf{k}} = \frac{\Delta_{\mathbf{k}}}{\xi_{\mathbf{k}} + \sqrt{\xi_{\mathbf{k}}^2 + \Delta_{\mathbf{k}}^2}}, \quad (117)$$

using the mean-field result from (97). Owing to the projection operator P_N we can then represent the wave function by a product of $N/2$ pairs, where we use $N_{\sigma} = N_{\uparrow} = N_{\downarrow} = N/2$, valid for a BCS wave function. In (116d) we assumed $a_{\mathbf{k}} = a_{-\mathbf{k}}$, applied a Fourier transformation and defined

$$a(\mathbf{r}) \equiv \sum_{\mathbf{k}} a_{\mathbf{k}} \cos(\mathbf{k} \cdot \mathbf{r}). \quad (118)$$

Finally, we arrive at the real space representation of $P_N|\Psi_0\rangle$ as in (116d).

As all configurations α in (114) have the same to particle number N , $\langle\alpha|\Psi_0\rangle = \langle\alpha|P_N|\Psi_0\rangle$. Making use of (116d) one finds that the overlap, $\langle\alpha|\Psi_0\rangle$, is given (see [17, 147]) by the determinant of the matrix A_{α} , which has

the form

$$\begin{pmatrix} a(\mathbf{R}_{1,\downarrow} - \mathbf{R}_{1,\uparrow}) & a(\mathbf{R}_{1,\downarrow} - \mathbf{R}_{2,\uparrow}) & \dots & a(\mathbf{R}_{1,\downarrow} - \mathbf{R}_{N_\sigma,\uparrow}) \\ a(\mathbf{R}_{2,\downarrow} - \mathbf{R}_{1,\uparrow}) & a(\mathbf{R}_{2,\downarrow} - \mathbf{R}_{2,\uparrow}) & & a(\mathbf{R}_{2,\downarrow} - \mathbf{R}_{N_\sigma,\uparrow}) \\ \vdots & & \ddots & \vdots \\ a(\mathbf{R}_{N_\sigma,\downarrow} - \mathbf{R}_{1,\uparrow}) & a(\mathbf{R}_{N_\sigma,\downarrow} - \mathbf{R}_{2,\uparrow}) & \dots & a(\mathbf{R}_{N_\sigma,\downarrow} - \mathbf{R}_{N_\sigma,\uparrow}) \end{pmatrix}.$$

To see this we must expand (116d) and gather all terms contributing to the configuration α , which has down electrons on $\{\mathbf{R}_{1,\downarrow}, \mathbf{R}_{2,\downarrow}, \dots, \mathbf{R}_{N_\sigma,\downarrow}\}$ and up electrons on $\{\mathbf{R}_{1,\uparrow}, \mathbf{R}_{2,\uparrow}, \dots, \mathbf{R}_{N_\sigma,\uparrow}\}$. The number and functional form of these terms are obviously the same as those for $|A_\alpha|$. Next we must order up and down electrons in the same way for all terms. By doing so we pick up relative signs, which are exactly reproduced by the determinant of A_α .

We note that the above real-space representation can be extended [86] to wave functions, which allow for a staggered magnetization and an unequal number of up and down electrons, $N_\uparrow \neq N_\downarrow$. Then, the $a(\mathbf{r})$ in (116d) and (118) becomes spin and site dependent, i.e. $a(\mathbf{r}) \rightarrow a(\mathbf{R}_{i,\sigma_i}, \mathbf{R}_{j,\sigma_j}, \sigma_i, \sigma_j)$. The values of $a(\mathbf{R}_{i,\sigma_i}, \mathbf{R}_{j,\sigma_j}, \sigma_i, \sigma_j)$ depend on the particular choice of the mean-field wave function and can be evaluated numerically. The overlap $\langle \alpha | \Psi_0 \rangle$ is then determined by [86]

$$\langle \alpha | \Psi_0 \rangle = P_f(\mathbf{Q}), \quad (119)$$

where $P_f(\mathbf{Q})$ is the Pfaffian[†] of the matrix

$$\mathbf{Q} = a(\mathbf{R}_{i,\sigma_i}, \mathbf{R}_{j,\sigma_j}, \sigma_i, \sigma_j) - a(\mathbf{R}_{j,\sigma_j}, \mathbf{R}_{i,\sigma_i}, \sigma_j, \sigma_i). \quad (120)$$

The positions of the electrons, \mathbf{R}_{i,σ_i} and \mathbf{R}_{j,σ_j} determine the real space configuration α . For a simple BCS wave function with $a(\mathbf{R}_{i,\uparrow}, \mathbf{R}_{j,\uparrow}, \uparrow, \uparrow) = a(\mathbf{R}_{i,\downarrow}, \mathbf{R}_{j,\downarrow}, \downarrow, \downarrow) = 0$ and $a(\mathbf{R}_{i,\uparrow} - \mathbf{R}_{j,\downarrow}) = a(\mathbf{R}_{i,\uparrow}, \mathbf{R}_{j,\downarrow}, \uparrow, \downarrow)$, the overlap $\langle \alpha | \Psi_0 \rangle$ in equation (119) reduces to the previously discussed determinant $|A_\alpha|$.

5.1.2. Implementation of the Monte Carlo simulation. Using (114), we may write the expectation value of an operator \hat{O} in $|\Psi\rangle$ as,

$$\langle \hat{O} \rangle_\Psi = \frac{\langle \Psi_0 | P_G P_N \hat{O} P_N P_G | \Psi_0 \rangle}{\langle \Psi_0 | P_G P_N P_G | \Psi_0 \rangle} \quad (121a)$$

$$= \sum_{\alpha, \beta} \langle \alpha | \hat{O} | \beta \rangle \frac{\langle \Psi_0 | \alpha \rangle \langle \beta | \Psi_0 \rangle}{\langle \Psi_0 | P_N P_G | \Psi_0 \rangle} \quad (121b)$$

$$= \sum_{\alpha} \left(\sum_{\beta} \frac{\langle \alpha | \hat{O} | \beta \rangle \langle \beta | \Psi_0 \rangle}{\langle \Psi_0 | \alpha \rangle} \right) \frac{|\langle \Psi_0 | \alpha \rangle|^2}{\langle \Psi_0 | P_N P_G | \Psi_0 \rangle} \quad (121c)$$

$$= \sum_{\alpha} f(\alpha) p(\alpha), \quad (121d)$$

[†]The Pfaffian is the analogue of a determinant which is defined only for antisymmetric matrices. For an antisymmetric matrix A , the square of the Pfaffian is equivalent to its determinant, namely, $P_f(A)^2 = |A|$.

with,

$$f(\alpha) = \sum_{\beta} \frac{\langle \alpha | \hat{O} | \beta \rangle \langle \beta | \Psi_0 \rangle}{\langle \Psi_0 | \alpha \rangle}, \quad (122a)$$

$$p(\alpha) = \frac{|\langle \Psi_0 | \alpha \rangle|^2}{\langle \Psi_0 | P_N P_G | \Psi_0 \rangle}. \quad (122b)$$

Here, α and β are real space configurations (115). As

$$p(\alpha) \geq 0, \quad \sum_{\alpha} p(\alpha) = 1, \quad (123)$$

are the features of a probability distribution, we can evaluate $\langle \hat{O} \rangle_{\Psi}$ by a random walk through the configuration space with weight $p(\alpha)$. Therefore, we can analyse (121) with a standard metropolis Monte Carlo calculation. We note that the norm $\langle \Psi_0 | P_N P_G | \Psi_0 \rangle$ in (122b) is not of relevance within the Monte Carlo calculation, because only relative probabilities $p(\alpha)$ enter the transition probability.

Next, we comment on the updating procedure and the calculation of the determinant $|A_{\alpha}|$. Most VMC calculations generate a new configuration α' by randomly interchanging two electrons with opposite spin or moving an electron to an empty site. The random walks thus constructed are ergodic. In general, to optimize the numerical performance, the rules for generating the random walk through the configuration space should be chosen so as to maximize the acceptance rate, $T(\alpha \rightarrow \alpha')$.

The calculation of $|A_{\alpha}|$ is numerically expensive and is required at each Monte Carlo step for the computation of $p(\alpha)$. Therefore, it is advantageous to determine the ratio $|A_{\alpha'}|/|A_{\alpha}|$ between new and old determinant (new and old configuration α' and α) instead of directly evaluating $|A_{\alpha'}|$ for every configuration. According to Ceperley *et al.* [187], this ratio can be efficiently computed within $\mathcal{O}(N_{\sigma}^2)$ computation steps, while a direct evaluation of $|A_{\alpha'}|$ requires $\mathcal{O}(N_{\sigma}^3)$ steps. The trick is to store not only the matrix A_{α} , but also its inverse A_{α}^{-1} . For the commonly used updating procedures mentioned above, α' differs from α only by the interchange of two electrons with opposite spins or the interchange of an electron and an empty site. Thus, the matrices $A_{\alpha'}$ and A_{α} differ only by one row and one column, and $|A_{\alpha'}|/|A_{\alpha}| = |A_{\alpha'} A_{\alpha}^{-1}|$, which enters the transition rate $T(\alpha \rightarrow \alpha')$, can be easily computed.

A general advantage of the Monte Carlo method is the possibility to estimate the numerical accuracy systematically with the error being proportional to the inverse square root of the number of Monte Carlo steps N_r . Present computer capacities allow us to consider sufficiently large clusters, where finite size effects play a minor role. However, $a_{\mathbf{k}} = v_{\mathbf{k}}/u_{\mathbf{k}}$, defined in equation (117) becomes singular whenever $\Delta_{\mathbf{k}} = 0$ and $\xi_{\mathbf{k}} \leq 0$. In particular, this is problematic for a d -wave order parameter, for which $\Delta_{\mathbf{k}} = 0$ for all k -points along the Brillouin zone diagonals, i.e. $|k_x| = |k_y|$. It is thus convenient to avoid these \mathbf{k} points by an appropriate choice of boundary conditions. There are three different approaches discussed in literature. The first possibility is a tilted lattice with periodic boundary conditions (PBCs). Such a lattice has $L^2 + 1$ sites with odd L , preserves the fourfold rotational symmetry of the lattice and does not introduce any twist in the boundary conditions. An example of these (widely used) boundary conditions (see, e.g., [17, 21, 117, 147]) is illustrated

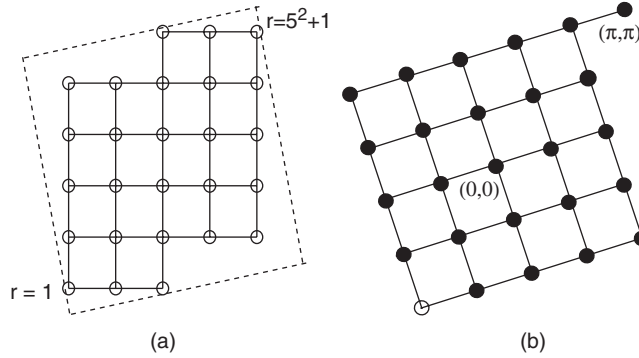


Figure 34. (a) Real-space picture of the $L^2 + 1$ lattice for $L = 5$, with PBCs, $(5, 1)$ and $(-1, 5)$, applied along the opposite edges of the tilted square indicated by dashed lines. (b) The \mathbf{k} -space Brillouin zone of the 'tilted lattice' for $L = 5$. Reprinted with permission from [117] © 2004 by the American Physical Society.

in figure 34. Another choice is an $L \times L$ lattice with even L and periodic and anti-periodic boundary conditions in the x and the y direction, respectively. Finally it is possible to use a rectangular $L_x \times L_y$ lattice with PBCs and mutually coprime dimensions L_x and L_y , i.e. the greatest common divisor of L_x and L_y being 1.

5.2. Improvements of the trial wave function

The early VMC calculations for projected BCS states of Gros [17] and Yokoyama and Shiba [97] were carried out to check whether a Gutzwiller projected superconducting wave function is indeed a variationally good trial state for the t - J model. To limit the number of variational parameters, these authors used a dimensionless dispersion, $\xi_{\mathbf{k}} = -2(\cos k_x + \cos k_y) - \mu$, and various superconducting gap functions $\Delta_{\mathbf{k}}$ to calculate $a_{\mathbf{k}} = \Delta_{\mathbf{k}} / (\xi_{\mathbf{k}} + \sqrt{\xi_{\mathbf{k}}^2 + \Delta_{\mathbf{k}}^2})$. In his original work, Gros [17] compared variational energies of s -wave, $\Delta_{\mathbf{k}} = \Delta$, d -wave, $\Delta_{\mathbf{k}} = \Delta(\cos k_x - \cos k_y)$, and extended s -wave, $\Delta_{\mathbf{k}} = \Delta(\cos k_x + \cos k_y) - \mu$, functions. By optimizing solely† the variational parameter Δ , he found that a d -wave gap can substantially lower the energy compared to projected Fermi sea ($\Delta_{\mathbf{k}} = 0$) at half-filling as well as at finite doping. The result is consistent with other early works such as the VMC calculations of Yokoyama and Shiba [97] or the mean-field theories of Zhang *et al.* [20] and Kotliar and Liu [18].

More detailed studies shown that the optimal superconducting state remains a pure d -wave even when mixed states of s - and d -wave pairing are considered [188]. The optimal variational parameter Δ decreases when going away from half-filling and vanishes at about 30% doping. The exact dimension of the superconducting

†Owing to the fixed particle number, the chemical potential μ becomes an additional free parameter. However, this parameter was fixed in [17] by setting the chemical potential μ to those of the unprojected wave function.

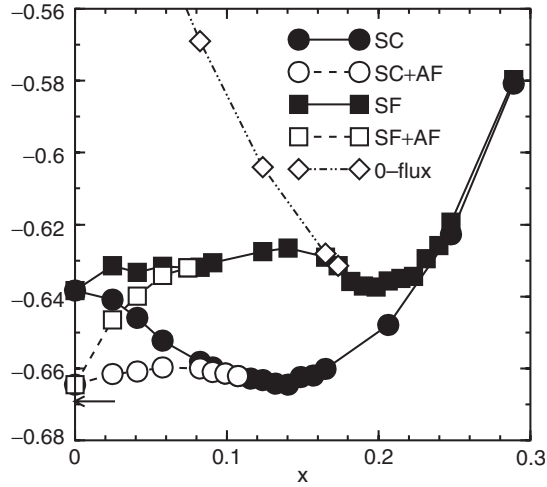


Figure 35. Optimal energies per site (in units of J) for five different Gutzwiller projected wave functions with a linear part subtracted ($E - \mu_{\text{sep}}$) as a function of doping x . Wave functions: superconducting without antiferromagnetism (SC, full circles), superconducting with antiferromagnetism (SC+AF, open circles), staggered-flux without antiferromagnetism (SF, full squares), staggered-flux with antiferromagnetism (SF+AF, open squares) and zero-flux (projected Fermi sea, open diamonds). The arrow in the panel shows the best variational estimate for the half-filled system ($E = -0.669J$ per site) [189, 190]. Only nearest-neighbour hopping is considered and $J/t = 0.3$. Reprinted with permission from [105] © 2004 by the American Physical Society.

region in the phase diagram depends on the choice of J/t as well as on the inclusion of the correlated hopping term [188].

5.2.1. Antiferromagnetism and flux states. Further extensions [102–106] considered the incorporation of antiferromagnetism for a more accurate description of the t – J model near half-filling. These studies show a coexistence between superconductivity and antiferromagnetic long-range order (AFLRO) for doping $x \leq 0.1$. At half-filling, the optimal wave function constructed in this manner has a staggered magnetization of 0.75 and a variational energy of $-0.664J$ per site: impressively close to the best numerical estimate of $-0.669J$ per site by Green’s function Monte Carlo techniques [189, 190]. A comparison of the variational energies of the different wave functions is given in figure 35. The figure also reveals an upward convexity of the ground state energy (SC+AF state) as a function of doping. This indicates a phase separation at $x_{\text{sep}} = 0.13$ (see figure 35). However, Ivanov [105] demonstrated that a sufficiently strong nearest-neighbour Coulomb repulsion can suppress the formation of separated phases. Further VMC calculations showed that the coexistence of superconductivity and AFLRO is nearly absent if next- and second-nearest-neighbour hopping are included [106]. For these more realistic model parameters, the AFLRO disappears at about 6% doping in better agreement with experimental observations [106].

Apart from the superconducting states, the projected staggered-flux state has also been studied as a competitive variational state; however, its energy lies above those

of the d -wave for all dopings (figure 35). As discussed in section 4, the flux state becomes identical to the superconducting state at half-filling explaining the collapse of the energies in figure 35 (see also [142]). This behaviour is due to SU(2) symmetry, which is also responsible for the occurrence of staggered-vorticity correlations of current in the d -wave state at small dopings [191].

5.2.2. Increasing the number of variational parameters. In recent VMC calculations, the chemical potential μ as well as the next nearest neighbour hopping t'_{var} are chosen as additional variational parameters, which are optimized numerically. While the chemical potential has minor influence on the optimal state [188], a variational t'_{var} can significantly effect the shape of the FS. Himeda and Ogata [192] reported that for a bare dispersion $t' = 0$ and a doping level of $x = 0.15$ the lowest energy is provided by a variational $t'_{\text{var}} = -0.1t$, causing a spontaneous deformation of the FS. More detailed VMC studies [161] include next-nearest (t') and next-next-nearest (t'') neighbour hopping in the bare dispersion and also use variational parameters t'_{var} and t''_{var} . The obtained momentum distribution $n(\mathbf{k})$ (related to the FS, see section 6.5) together with the optimal variational Δ and t'_{var} from these calculations are illustrated in figure 36. This work of Shih *et al.* [161] also revealed that the more negative the bare ratio t'/t , the higher the superconducting pairing in the optimal variational state of the t - J model. This is in agreement with band-structure calculations [160] that suggest that the ratio t'/t is essential to raise T_c . Similar trends can be inferred from the RMFT calculations for the Hubbard model discussed in section 4.3.2.

VMC studies of inhomogeneous phases [193] find that around $x = \frac{1}{8}$, stripe states with fluctuating d -wave superconductivity can lower the variational ground state energy in the 2D t - J model. More recent studies report that at $x = \frac{1}{8}$, a bond-order modulated staggered-flux state can also overcome the RVB superconductor for sufficiently large short-range Coulomb repulsion [194]. However, the energy gains within these studies are often quite small and sensitively depend on model parameters.

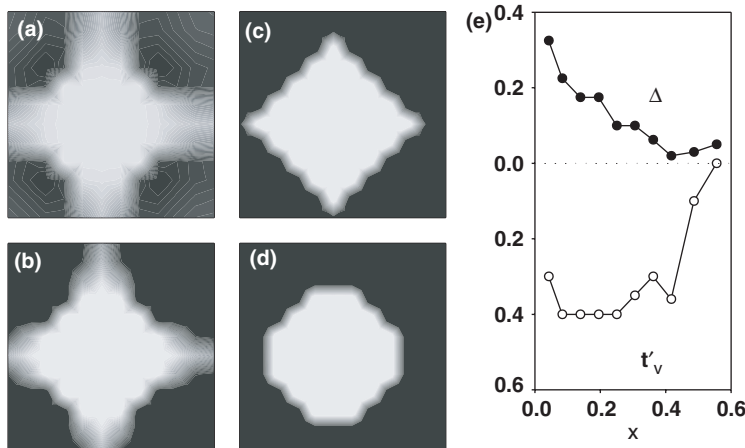


Figure 36. Momentum distribution $n(\mathbf{k})$ in the first Brillouin zone for doping (a) $x = 0.19$, (b) $x = 0.31$, (c) $x = 0.42$ and (d) $x = 0.49$ for 12×12 lattice with $J/t = 0.3$, $t' = -0.3t$ and $t'' = 0$. (e) Optimal parameters t'_v (squares) and Δ (circles). Reprinted with permission from [161] © 2004 by the American Physical Society.

Nevertheless, these VMC calculations show that the slightly doped t – J model exhibits tendencies towards various inhomogeneities, which could be relevant for explaining some of the experimental observations in the underdoped HTSCs.

The energy of the projected d -wave state can be improved further by the incorporation of Jastrow factors (see section 2.6). Sorella *et al.* [145] showed numerically that such wave functions lower the variational energy and still exhibit long-range superconducting order. Nevertheless there is still debate (see [195–197]) whether the superconductivity within the VMC scheme results only from a biased choice of the wave function or is indeed a ground state property of the t – J model. In our opinion, this debate does not pose an obstacle to our understanding of the HTSCs, as we are primarily interested in physical properties of projected wave functions rather than in proving them to be exact ground states of a particular Hamiltonian. In this way, we follow the point of view espoused by Anderson *et al.* [198]

‘The philosophy of this method is analogous to that used by BCS for superconductivity, and by Laughlin for the fractional quantum Hall effect: simply guess a wave function. Is there any better way to solve a non-perturbative many-body problem?’

5.2.3. Investigation of the Pomeranchuk instability. The possibility that strong correlations may break the symmetry of the underlying FS was studied recently in [8]. As illustrated in figure 37(a), this instability results in a deformation of the FS, which becomes quasi-1D, although the underlying 2D lattice is still isotropic. Motivated by the FS depicted in figure 37(a), the state resulting from the tetragonal symmetry breaking can be called a ‘quasi-1D state’. This phenomenon is also called a Pomeranchuk instability of the FS.

To investigate instabilities towards quasi-1D states, we have to extend the variational space by an additional order parameter, which allows for a finite asymmetry in the wave function. A possible choice was proposed by Edegger *et al.* [8], who determined $a_{\mathbf{k}} = \Delta_{\mathbf{k}}/(\xi_{\mathbf{k}} + \sqrt{\xi_{\mathbf{k}}^2 + \Delta_{\mathbf{k}}^2})$ by using

$$\xi_{\mathbf{k}} = -2 \left[(1 + \delta_{\text{var}}^{\text{1D}}) \cos k_x + (1 - \delta_{\text{var}}^{\text{1D}}) \cos k_y \right] - 4t'_{\text{var}} \cos k_x \cos k_y - \mu_{\text{var}} \quad (124)$$

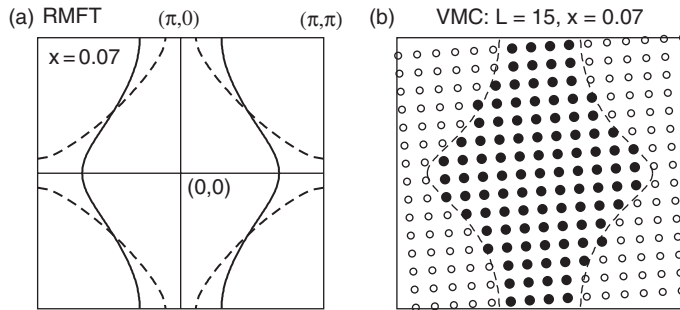


Figure 37. FS of the isotropic t – J model with $J = 0.3t$ and $t' = -0.3t$ at $x = 0.07$. (a) RMFT results for the FS of the normal state with $\Delta_{\mathbf{k}} \equiv 0$ (quasi-1D state, solid curve) and the optimal d -wave state (isotropic, dashed line). (b) Best quasi-1D state on a $(15^2 + 1)$ -sites lattice by VMC; filled circles indicate the FS. Reprinted with permission from [8] © 2006 by the American Physical Society.

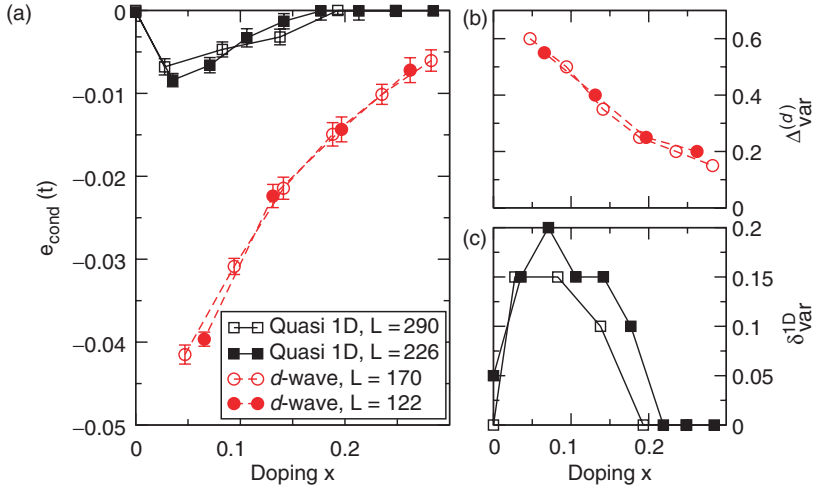


Figure 38. (a) VMC results for condensation energies per site e_{cond} of the quasi-1D state ($\delta_{\text{var}}^{1D} \neq 0$, $\Delta_{\mathbf{k}} \equiv 0$) and the d -wave state ($\Delta_{\mathbf{k}} \neq 0$, $\delta_{\text{var}}^{1D} \equiv 0$) with $t' = -0.3t$; see (124) and (125) for the definition of these states. The optimal variational $\Delta_{\text{var}}^{(d)}$ of the d -wave is shown in (b), the optimal variational asymmetry δ_{var}^{1D} of the quasi-1D state is given in (c). The errors in (b) and (c) are $\Delta\Delta_{\text{var}}^{(d)} = 0.05$ and $\Delta\delta_{\text{var}}^{1D} = 0.05$, respectively. System sizes: $L = 11^2 + 1 = 122$, $L = 13^2 + 1 = 170$, $L = 15^2 + 1 = 226$ and $L = 17^2 + 1 = 290$. Reprinted with permission from [8] © 2006 by the American Physical Society.

and

$$\Delta_{\mathbf{k}} = \Delta_{\text{var}}^{(d)}(\cos k_x - \cos k_y) + \Delta_{\text{var}}^{(s)}(\cos k_x + \cos k_y). \quad (125)$$

The five variational parameters, namely, the asymmetry δ_{var}^{1D} between the x and the y direction, the variational next-nearest neighbour hopping term t'_{var} , a variational chemical potential μ_{var} and variational parameters for d - and s -wave pairing, $\Delta_{\text{var}}^{(d)}$ and $\Delta_{\text{var}}^{(s)}$, can be optimized by determining the energy expectation values for different choices of variational parameters within a standard VMC technique.

VMC calculations for the isotropic t - J model [8] show, in agreement with previous studies [199–201], that the optimal variational state remains a pure d -wave without any anisotropy (see figure 38). However, when restricting solely to non-superconducting solutions, i.e. setting $\Delta_{\mathbf{k}} \equiv 0$ by using $\Delta_{\text{var}}^{(d)} = \Delta_{\text{var}}^{(s)} = 0$, a projected anisotropic Fermi sea provides a better energy than the isotropic one. In figure 38, this effect is shown for a VMC calculation [8] in an isotropic t - J model. The figure also illustrates that the optimal d -wave state has much better energy than the quasi-1D state, which is the best state in the variational subspace $\Delta_{\mathbf{k}} \equiv 0$.

The situation can be quite different when the underlying lattice structure is anisotropic. In this case, the tendency towards a quasi-1D state is present even in the superconducting state. RMFT, VMC [8] and SBMFT [199, 200] calculations predict an optimal state in which the bare anisotropy δ_0^{1D} of the lattice can be significantly enhanced due to the electron correlations. As seen in figure 39(a), the bare asymmetry of $\delta_0^{1D} = 0.05$ increases within the RMFT calculations up to about

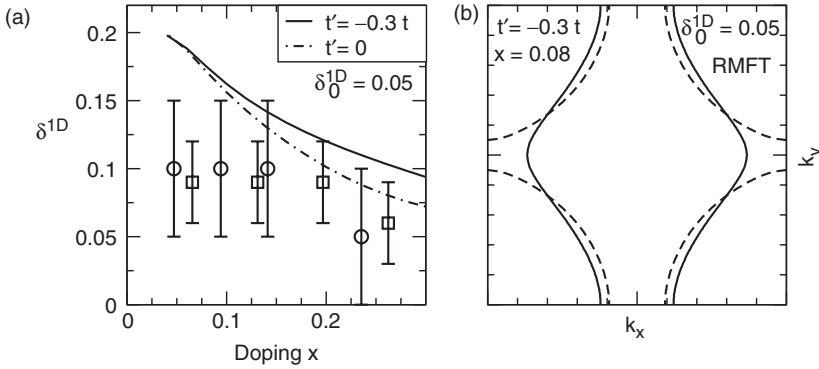


Figure 39. RMFT and VMC results for the $d+s$ -wave ground state of the anisotropic t - J model with $J=0.3t$ and $\delta_0^{1D} \equiv (t_x - t_y)/(t_x + t_y) = 0.05$. (a) Effective asymmetry $\delta^{1D} \equiv (\tilde{t}_x - \tilde{t}_y)/(\tilde{t}_x + \tilde{t}_y)$ from RMFT as a function of hole doping x for (dashed curve) $t' = 0$ and (solid curve) $t' = -0.3t$. VMC results for $t' = 0$ are given by squares and circles for $L=122$ and $L=170$, respectively. (b) RMFT FS (solid curves) of the $d+s$ -wave ground state and the tight binding dispersion (dashed curves) at $x=0.08$ with $t' = -0.3t$ and $\delta_{1D}^0 = 0.025$. Reprinted with permission from [8] © 2006 by the American Physical Society.

$\delta_{\text{opt}}^{1D} = 0.2$ in the underdoped regime. These results are confirmed to some extent by VMC calculations (figure 39(a), circles and squares), which show an increase of the asymmetry up to about $\delta_{\text{var}}^{1D} \approx 0.1$. Furthermore, the enhancement of anisotropy may even lead to a change in the topology of the underlying FS as can be inferred from figure 39(b).

The Pomeranchuk instability is one out of several possible instabilities in the t - J model that arise from the effects of superexchange and that can be revealed by VMC and RMFT techniques. As $J \propto 4t^2/U$, a small asymmetry in the bare hopping integral t becomes twice as large in the superexchange energy. Hence, it is natural that the effects discussed in this section are largest in the underdoped regime, where the dispersion is mainly determined by J .

5.3. Ground state properties: VMC results

Within this section, we discuss the ground state properties of the HTSCs by considering observables in a Gutzwiller projected superconducting state. We follow, in part, Paramakanti *et al.* [21, 117], who studied the Hubbard model in the strong coupling limit using the re-transformed trial wave function, $e^{-iS}P_G|\Psi_0\rangle$ (see section 4). By evaluating the canonical transformation e^{-iS} to $\mathcal{O}(t/U)$, this ansatz can be treated within the VMC scheme. The t/U corrections due to e^{-iS} provide a more accurate description of the HTSCs; however, the qualitative nature of the results is not changed compared with the t - J model. In the following, we ignore the possibility of the superconducting state coexisting with a flux state, antiferromagnetism or a charge ordered state.

5.3.1. Superconducting gap and order parameter. In the previous section, we saw that the variational parameter Δ , which is proportional to the superconducting gap $\Delta_{\mathbf{k}}$, increases in the limit of half-filling. The doping dependence of Δ is illustrated in

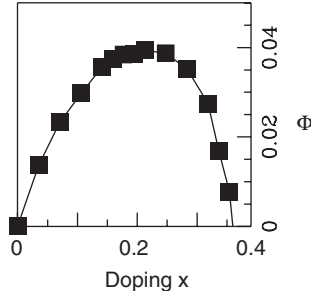


Figure 40. Doping dependence of the superconducting order parameter Φ from VMC calculations of Paramakanti *et al.* [21]. Model parameters: $U = 12t$, $t' = -t/4$.

figure 36 and resembles the RMFT result (figure 29) as well as the experimental observed gap at $\mathbf{k} = (\pi, 0)$. However, we cannot deduce the relevant energy scale of the gap from Δ , because it is a dimensionless parameter within the VMC calculations. For detailed statements about the gap we have to consider the energy of excited states as we do in sections 6 and 7.

When considering the variational parameter Δ , we must realize, as discussed in section 4, that it does not correspond to the true superconducting order $\Phi \equiv |\langle c_{i\uparrow}^\dagger c_{i+\tau\downarrow}^\dagger - c_{i\downarrow}^\dagger c_{i+\tau\uparrow}^\dagger \rangle|$. The relevant physical quantity here is the off-diagonal long-range order (ODLRO) [17, 21, 147] defined by

$$F_{\alpha,\beta}(\mathbf{r} - \mathbf{r}') = \langle c_{\uparrow}^\dagger(\mathbf{r}) c_{\downarrow}^\dagger(\mathbf{r} + \hat{\alpha}) c_{\downarrow}(\mathbf{r}) c_{\uparrow}(\mathbf{r} + \hat{\beta}) \rangle,$$

where $\hat{\alpha}, \hat{\beta} = \hat{x}, \hat{y}$. In the limit of large $|\mathbf{r} - \mathbf{r}'|$, $F_{\alpha,\beta}$ is related to Φ^2 by means of $F_{\alpha,\beta} \rightarrow \pm \Phi^2$ with $+$ ($-$) sign obtained for $\hat{a} \parallel$ (\perp) to \hat{b} , indicating d -wave superconductivity [21]. The doping dependence of the superconducting order parameter Φ is depicted in figure 40 (VMC calculations of Paramakanti *et al.* [21]). It is not identical to Δ as first noted by Gros [17, 147]. The VMC calculation match the RMFT result (figure 29), where Φ vanishes linearly as $x \rightarrow 0$. The vanishing order parameter Φ indicates a Mott insulating phase at $x=0$, where superconductivity is destroyed by the suppression of particle number fluctuations. At finite doping x a superconducting state is realized in the range $0 < x < 0.35$.

5.3.2. Derivation of spectral features from ground state properties. Next we follow [21] and analyse the one-particle spectral function $A(\mathbf{k}, \omega)$ by calculating the moments

$$M_l(\mathbf{k}) = \int_{-\infty}^0 d\omega \omega^l A(\mathbf{k}, \omega), \quad (126)$$

in the projected d -wave ground state at $T=0$. This ansatz allows us to obtain information about $A(\mathbf{k}, \omega)$ from ground state expectation values without the need for explicit representations of the excited states. We first concentrate on the zeroth moment $M_0(\mathbf{k}) \equiv n(\mathbf{k})$, which is equivalent to the moment distribution $n(\mathbf{k})$. figure 41(a) shows that $n(\mathbf{k})$ has a jump along $(0, 0)$ to (π, π) . This implies the

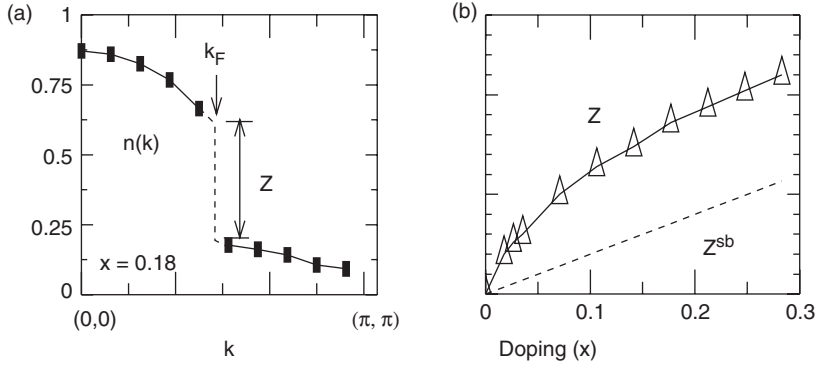


Figure 41. (a) The momentum distribution function $n(\mathbf{k})$ plotted along the diagonal $\mathbf{k} = (k, k)$ showing the jump at k_F which implies a gapless nodal QP with spectral weight Z . (b) Nodal QP weight $Z(x)$ as a function of doping x compared with the simple SBMFT result $Z^{sb}(x) = x$. Model parameters: $U = 12t$, $t' = -t/4$. Reprinted with permission from [21] © 2001 by the American Physical Society.

existence of gapless QPs and allows us to write the low-energy part of the spectral function along the diagonal as

$$A(\mathbf{k}, \omega) = Z\delta(\omega - \xi_k) + A^{\text{inc}}, \quad (127)$$

where, $\xi_k = v_F(k - k_F)$, is the QP dispersion and A^{inc} , a smooth incoherent part. The location of the discontinuity determines the Fermi point k_F and its magnitude, the QP weight, Z . figure 41(b) reveals a significant doping dependence and shows that Z vanishes when approaching the Mott–Hubbard insulator $x = 0$. This behaviour is in agreement with more direct calculations, which explicitly include QP states (sections 6 and 7) as well as experiments.

To determine the nodal Fermi velocity v_F , we have to evaluate the first moment $M_1(\mathbf{k}) = \langle c_{\mathbf{k}\sigma}^\dagger [H, c_{\mathbf{k}\sigma}] \rangle$ along the nodal direction. Owing to the singular behaviour of $A(\mathbf{k}, \omega)$ at k_F , it can be written as,

$$M_1(\mathbf{k}) = Z\xi_k\Theta(-\xi_k) + \text{smooth part}. \quad (128)$$

As the slope $dM_1(\mathbf{k})/dk$ has a discontinuity of Zv_F at k_F , Paramakanti *et al.* [21] extracted the nodal Fermi velocity v_F as shown in figure 42(a). The doping dependence of v_F together with its bare value v_F^0 are shown in figure 42(b). We see that Fermi velocity is only weakly doping dependent, a result which is consistent with the ARPES data. However, this estimate of v_F is rather inaccurate compared with the direct evaluation [146] from the QP excitation energies, which are discussed in section 7.

Ground state expectation values also provide important information about the optical conductivity in the Hubbard and the t – J model. The total optical spectral weight $D_{\text{tot}}(x)$ can be calculated by [117]

$$\int_0^\infty d\omega \text{Re}\sigma(\omega) = \pi \sum_{\mathbf{k}} m^{-1}(\mathbf{k})n(\mathbf{k}) \equiv \pi D_{\text{tot}}/2, \quad (129)$$

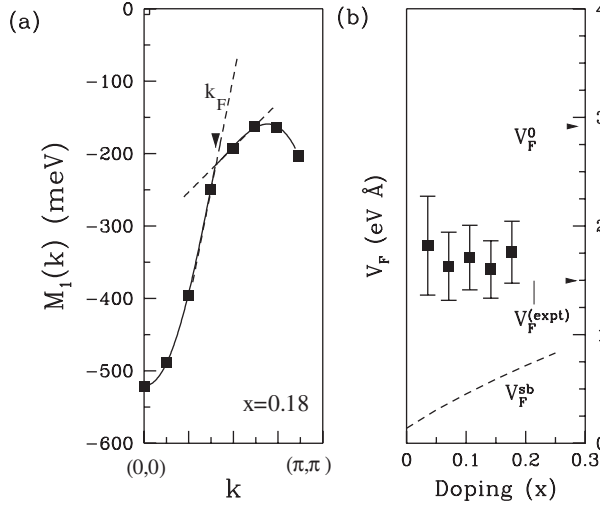


Figure 42. (a) The first moment $M_1(\mathbf{k})$ of the spectral function along the zone diagonal, with smooth fits for $k < k_F$ and $k > k_F$, showing a discontinuity of Zv_F in its slope at k_F . (b) Doping dependence of the nodal QP velocity obtained from the slope discontinuity of $M_1(\mathbf{k})$. Error bars come from fits to $M_1(\mathbf{k})$ and errors in Z . Also shown are the bare nodal velocity v_F^0 , the slave boson mean field $v_F^{sb}(x)$ (dashed line) and the ARPES estimate $v_F^{(expt)}$ [23, 24]. Model parameters: $U = 12t$, $t' = -t/4$. Reprinted with permission from [21] © by the American Physical Society.

where $m^{-1}(\mathbf{k}) = (\partial^2 \epsilon(\mathbf{k}) / \partial \mathbf{k}_x \partial \mathbf{k}_x)$ is the non-interacting mass tensor. Here $\epsilon(\mathbf{k})$ is the non-interacting dispersion (we set $\hbar = c = e = 1$). As the integral in (129) goes from zero to $+\infty$, it includes contributions from the upper Hubbard band and is thus finite even at $x=0$ as shown in figure 43(a).

Paramekanti *et al.* [21, 117] emphasized that the low-frequency optical weight, or Drude weight [202],

$$D_{\text{low}} = \partial^2 \langle H_A \rangle / \partial A^2, \quad (130)$$

is more interesting, because the upper cutoff is chosen smaller than U and thus excludes the upper Hubbard band. In (130), A is the electron-magnetic vector potential, which is introduced into the Hamiltonian (1) in terms of a Peierls substitution [202],

$$c_{i\sigma}^\dagger c_{j\sigma} \rightarrow c_{i\sigma}^\dagger c_{j\sigma} \exp(ie\mathbf{A}(\mathbf{R}_i - \mathbf{R}_j)), \quad (131)$$

where we used $\mathbf{A} = (A, 0)$ and set $\hbar = c = 1$ for simplicity. As shown in figure 43(a), the Drude weight D_{low} vanishes linearly for $x \rightarrow 0$. This demonstrates that the Gutzwiller projected superconductor indeed describes an insulator in the half-filled limit, which can be argued to be a general property of projected states [117]. The VMC results for the Drude weight D_{low} resemble the experimental data in magnitude as well as in the doping dependence quite well [117, 203]. By plotting D_{low} versus Z (from the nodal point) Paramekanti *et al.* also illustrated that $D_{\text{low}} \propto Z$, see figure 43(b).

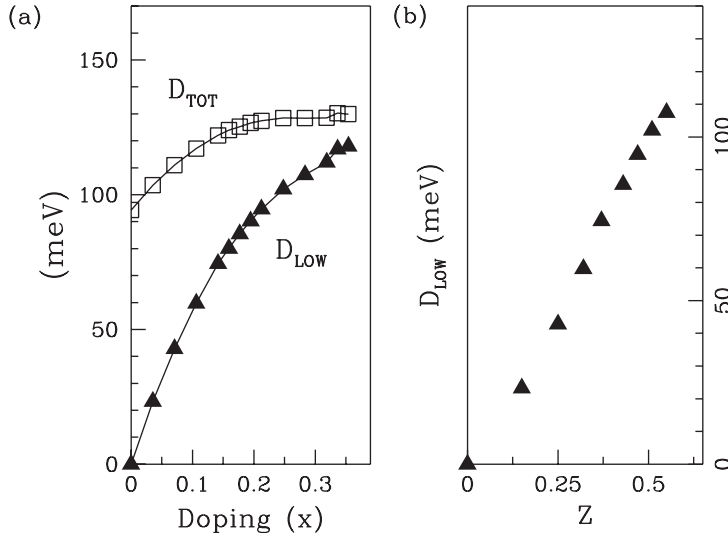


Figure 43. (a) Doping dependence of the total (D_{tot}) and low-energy (D_{low}) optical spectral weights. (b) The optical spectral weight D_{low} versus the nodal QP weight Z . Model parameters: $U = 12t$, $t' = -t/4$. Reprinted with permission from [21] © 2001 by the American Physical Society.

The Drude weight D_{low} also provides an upper bound to the superfluid stiffness D_s , i.e. $D_s \leq D_{\text{low}}$ (see [204]). It follows that $D_s \rightarrow 0$ as $x \rightarrow 0$ in agreement with experiments [205]. As the penetration depth λ_L is related to D_s by $\lambda_L^{-2} = 4\pi e^2 D_s / \hbar^2 c^2 d_c$, where d_c is the mean-interlayer spacing along the c -axis in a layered compound, Paramakanti *et al.* [117] could also estimate a lower bound for λ_L which is again consistent with the experimental data.

These VMC calculations based on a Gutzwiller projected superconducting ground state describe several key features of HTSCs remarkable well. The results are in general agreement with RMFT and confirm the usefulness of projected wave functions in the context of HTSCs. Although restricted to $T=0$, the above ansatz gives us some hints about the finite-temperature regime. The superconducting order parameter Φ resembles the doping dependence of T_c and vanishes at half-filling, while the superconducting gap (expected to scale with Δ) remains finite. This suggests that the underdoped regime exhibits strong pairing and that the superconducting transition may be determined by the onset of phase coherence (rather than the vanishing of pairing amplitude).

6. QP states within RMFT

Extending the RMFT to excited states requires the consideration of Gutzwiller-Bogoliubov QPs within the t - J and the Hubbard model. These Gutzwiller-Bogoliubov excitations then allow for a systematic analysis of the single-particle spectral function and explain momentum- and doping-dependent features in ARPES and STM experiments. Apart from these key results, in this section we

also discuss the renormalization of the current carried by Gutzwiller–Bogoliubov QPs and the consequences for the suppression of the superfluid density. We also discuss the discrepancies between different approaches in determining the underlying FS of a Gutzwiller projected superconductor.

6.1. Coherent and incoherent spectral weight

To model the spectral features of HTSCs, we need to study the excited states of a Gutzwiller projected superconductor. In this section, we consider the transfer of spectral weight from coherent QPs to an incoherent background. Stimulated by STM, which reveals a striking particle–hole asymmetry in the spectra of underdoped HTSCs [50, 53, 54], this problem has received much attention recently and investigated using both RMFT [6, 153, 206] and VMC methods [6, 21, 117, 207–212]. As nicely seen in the experiments, e.g. in [53, figures 1(c) and 3(e)] or figure 11, the spectral weights for hole and particle addition show a distinct asymmetry.

6.1.1. Sum rules for the spectral weight. The asymmetry in the STM spectra may be explained qualitatively by considering sum rules [206, 213–216] for the one-particle spectral function,

$$A(\mathbf{k}, \omega) = \sum_m \langle 0 | c_{\mathbf{k}\sigma}^\dagger | m \rangle \langle m | c_{\mathbf{k}\sigma} | 0 \rangle \delta(\omega + (E_m - E_0)) \quad (132a)$$

$$+ \sum_m \langle 0 | c_{\mathbf{k}\sigma} | m \rangle \langle m | c_{\mathbf{k}\sigma}^\dagger | 0 \rangle \delta(\omega - (E_m - E_0)), \quad (132b)$$

with,

$$\int_{-\infty}^{\infty} d\omega A(\mathbf{k}, \omega) = 1. \quad (133)$$

In (132a) and (132b), we use the $T=0$ spectral representation of $A(\mathbf{k}, \omega)$, where $|m\rangle$ are the exact many-body eigenstates with energies E_m . The ground state is given by $m=0$, and ω is measured with respect to the chemical potential. We are now interested in the low-energy spectral weight of a doped Mott insulator described by a Gutzwiller projected ground state, i.e. $|0\rangle \sim |\Psi\rangle \equiv P_G |\Psi_0\rangle$.

When removing a hole from the ground state (as in (132a)) it is clear that no doubly occupied sites are created. Thus, the resulting state is situated in LHB and involves only low-energy excitations, i.e. $0 < E_m - E_0 \ll U$ (excitation energies much smaller than the Hubbard U). Thus, on the hole side, the low-energy spectral weight corresponding to momentum \mathbf{k} and spin σ is given by

$$\int_{-\infty}^0 d\omega A(\mathbf{k}, \omega) = \langle 0 | c_{\mathbf{k}\sigma}^\dagger c_{\mathbf{k}\sigma} | 0 \rangle = \langle n_{\mathbf{k}\sigma} \rangle_\Psi. \quad (134)$$

By summing over all spin and momenta, we obtain the total low energy spectral weight for the hole side,

$$\frac{1}{L} \sum_{\mathbf{k}, \sigma} \int_{-\infty}^0 d\omega A(\mathbf{k}, \omega) = \frac{1}{L} \sum_{\mathbf{k}, \sigma} \langle n_{\mathbf{k}\sigma} \rangle_\Psi = n. \quad (135)$$

We note that similar sum rules can be derived for the dynamical conductivity, namely, the f -sum rule [217].

The situation is different when adding an electron to the ground state (as in (132b)). In such a process a part of the resulting state is located in the ‘upper Hubbard band’ (UHB), i.e. a doubly occupied site may be created. Therefore, we have to choose an upper cutoff Ω_L (located between LHB and UHB) to extract the low-energy spectral weight. By integrating $A(\mathbf{k}, \omega)$ from zero to Ω_L , we restrict ourselves solely to the Gutzwiller projected eigenstates out of all $|m\rangle$, and we obtain†

$$\int_0^{\Omega_L} d\omega A(\mathbf{k}, \omega) = \langle 0 | c_{\mathbf{k}\sigma} P_G c_{\mathbf{k}\sigma}^\dagger | 0 \rangle = \langle P_G c_{\mathbf{k}\sigma} P_G c_{\mathbf{k}\sigma}^\dagger P_G \rangle_{\Psi_0}. \quad (136)$$

Summing again over all spin and momenta and making use of Fourier transformation, we find the total low energy spectral weight for the electron side to be,

$$\frac{1}{L} \sum_{\mathbf{k}, \sigma} \int_0^{\Omega_L} d\omega A(\mathbf{k}, \omega) = \frac{1}{L} \sum_{\mathbf{k}, \sigma} \langle P_G c_{\mathbf{k}\sigma} P_G c_{\mathbf{k}\sigma}^\dagger P_G \rangle_{\Psi_0} \quad (137a)$$

$$= \frac{1}{L} \sum_{l, \sigma} \langle P_G c_{l\sigma} (1 - n_{l-\sigma}) c_{l\sigma}^\dagger P_G \rangle_{\Psi_0} \quad (137b)$$

$$= \frac{1}{L} \sum_{l, \sigma} \langle (1 - n_{l-\sigma})(1 - n_{l\sigma}) \rangle_{\Psi} \quad (137c)$$

$$= 2 \cdot (1 - n), \quad (137d)$$

where we used $P_G c_{l\sigma}^\dagger P_G (1 - n_{l-\sigma}) c_{l\sigma}^\dagger P_G$ (for a site l) to obtain (137b).

From (135) and (137), we find that it is more difficult to add an electron to the LHB than to extract an electron in a doped Mott insulator. This asymmetry increases as one approaches half-filling. For a hole density, $x = 1 - n$, the total spectral weight on the particle side is reduced to $2x = 2(1 - n)$, while the hole side of the spectral weight is not much affected. Note that these sum rules, while explaining the particle–hole asymmetry of the total spectral weight, tell us very little about the energy distribution of spectral weight within the LHB.

We further note that the total spin-integrated spectral weight is 2 and the integrated spectral weight of the upper Hubbard band is consequently $2 - n - 2 \cdot (1 - n) = n$, which agrees with the Hubbard-I approximation for the paramagnetic case [218].

6.1.2. Definition of coherent QP excitations. To explain the distribution of spectral weight at low energies, we approximate the eigenstates $|m\rangle$ by the Gutzwiller–Bogoliubov QPs, equation (103), derived from RMFT [7, 206]. We formulate particle-like Gutzwiller–Bogoliubov QPs by

$$|\Psi_{\mathbf{k}\sigma}^{N+1}\rangle = P_{N+1} P_G \gamma_{\mathbf{k}\sigma}^\dagger |\Psi_0\rangle, \quad (138)$$

†For a more detailed reasoning leading to this step, we refer the reader to [206].

as well as hole-like Gutzwiller–Bogoliubov QPs with the same momentum and spin by

$$|\Psi_{\mathbf{k}\sigma}^{N-1}\rangle = P_{N-1}P_G\gamma_{\mathbf{k}\sigma}^\dagger|\Psi_0\rangle. \quad (139)$$

In the following, we fix the particle number N by the operator P_N and thus the ground state is $|\Psi^N\rangle = P_N P_G |\Psi_0\rangle$. To avoid confusion, we include an index N for the particle number in the wave function. At the level of mean-field theory, the energies corresponding to the states (138) and (139) are given by the RMFT excitations $E_{\mathbf{k}}$, as discussed in section 4.2.

Using (138) and (139) in (132a) and (132b) yields

$$A(\mathbf{k}, \omega) = Z_{\mathbf{k}}^+ u_{\mathbf{k}}^2 \delta(\omega - E_{\mathbf{k}}) + Z_{\mathbf{k}}^- v_{\mathbf{k}}^2 \delta(\omega + E_{\mathbf{k}}) + A^{\text{inc}}(\mathbf{k}, \omega), \quad (140)$$

with the QP weights $\tilde{Z}_{\mathbf{k}\sigma}^\pm$ given by

$$\tilde{Z}_{\mathbf{k}\sigma}^+ \equiv Z_{\mathbf{k}}^+ u_{\mathbf{k}}^2 = \frac{|\langle \Psi_{\mathbf{k}\sigma}^{N+1} | c_{\mathbf{k}\sigma}^\dagger | \Psi_0^N \rangle|^2}{\langle \Psi_{\mathbf{k}\sigma}^{N+1} | \Psi_{\mathbf{k}\sigma}^{N+1} \rangle \langle \Psi_0^N | \Psi_0^N \rangle}, \quad (141)$$

and

$$\tilde{Z}_{\mathbf{k}\sigma}^- \equiv Z_{\mathbf{k}}^- v_{\mathbf{k}}^2 = \frac{|\langle \Psi_{-\mathbf{k}-\sigma}^{N-1} | c_{\mathbf{k}\sigma} | \Psi_0^N \rangle|^2}{\langle \Psi_{-\mathbf{k}-\sigma}^{N-1} | \Psi_{-\mathbf{k}-\sigma}^{N-1} \rangle \langle \Psi_0^N | \Psi_0^N \rangle}. \quad (142)$$

Here, we distinguish between the QP weight $\tilde{Z}_{\mathbf{k}\sigma}^\pm$ mostly used in VMC calculations and the QP weight renormalization $Z_{\mathbf{k}}^\pm$ often given within RMFT studies. In (140), the Gutzwiller–Bogoliubov QPs lead to δ -peaked excitations, which are associated with the coherent peaks, e.g. seen in ARPES. For projected wave functions, the weight of these coherent excitations is renormalized (owing to Gutzwiller projection) by a factor $Z_{\mathbf{k}}^\pm$. Thus, by construction, the full spectral weight is not exhausted by the Gutzwiller–Bogoliubov excitations, (138) and (139), demanding the presence of an incoherent background $A^{\text{inc}}(\mathbf{k}, \omega)$.

It is not yet settled whether the asymmetry in the HTSCs comes from the incoherent part as dictated by the spectral sum rules or whether such an asymmetry is present in the coherent QP spectrum [6, 153, 206, 209, 210]. As we show below, recent works based on the GA support the former proposal [7, 206], i.e. a particle–hole symmetric QP weight renormalization,

$$Z_{\mathbf{k}} = Z_{\mathbf{k}}^+ = Z_{\mathbf{k}}^-. \quad (143)$$

However, recent VMC calculations [209, 211] (discussed in section 7.1) claim that this symmetry is exactly fulfilled only for \mathbf{k} at the (underlying) FS. Therefore, zero-energy (or very low-energy) excitations would still exhibit particle–hole symmetry, whereas coherent excitations at higher energies could lead to an asymmetry in spectral weight. This asymmetry in VMC results is most pronounced in the underdoped region and disappears in the limit of zero pairing (projected Fermi sea) [210, 211].

6.1.3. Incoherent background of the spectral weight. Next, we discuss the incoherent background of the hole spectrum. By using the spectral representation, (132a) and (132b), together with $A(\mathbf{k}, \omega)$ from (140), we find the relation,

$$\langle n_{\mathbf{k}\sigma} \rangle_\Psi = Z_{\mathbf{k}}^- u_{\mathbf{k}}^2 + n_{\mathbf{k}\sigma}^{\text{inc}}, \quad (144)$$

with

$$n_{\mathbf{k}\sigma}^{\text{inc}} = \int_{-\infty}^0 d\omega A^{\text{inc}}(\mathbf{k}, \omega). \quad (145)$$

Thus, the momentum distribution, $\langle n_{\mathbf{k}\sigma} \rangle$, provides the total spectral weight with momentum \mathbf{k} and spin σ at the hole side, i.e. the coherent weight $Z_{\mathbf{k}}^- u_{\mathbf{k}}^2$ overlaid by the incoherent background $n_{\mathbf{k}\sigma}^{\text{inc}}$. We calculate these quantities in section 6.3 by the GA and show their behaviour in the first Brillouin zone.

6.1.4. Divergent \mathbf{k} -dependent self-energy. In section 5.3, we discussed VMC results for the QP weight renormalization at the nodal point \mathbf{k}_F . These calculations show that $Z \rightarrow 0$ for $x \rightarrow 0$, where $Z = Z_{\mathbf{k}_F}^+ = Z_{\mathbf{k}_F}^-$. Before extending our considerations to all \mathbf{k} -points, let us discuss some consequences for the self-energy in the half-filled limit. Owing to the vanishing gap along the nodal direction, $(0, 0) \rightarrow (\pi, \pi)$, we can approximate Green's function in the vicinity of \mathbf{k}_F by $G^{-1}(\mathbf{k}, \omega) = \omega - \epsilon(\mathbf{k}) - \mu - \Sigma(\mathbf{k}, \omega)$, where $\Sigma \equiv \Sigma' + i\Sigma''$. Standard arguments then lead to the results [219],

$$Z = \left(1 - \frac{\partial \Sigma'}{\partial \omega}\right)^{-1}, \quad v_F = Z \left(v_F^0 + \frac{\partial \Sigma'}{\partial \mathbf{k}}\right), \quad (146)$$

where the right-hand side is evaluated at the node $(\mathbf{k}_F, \omega = 0)$. As $Z \rightarrow 0$ for $x \rightarrow 0$, $|\partial \Sigma' / \partial \omega|$ diverges like $1/x$ in this limit. Owing to the finite Fermi velocity v_F (see sections 4.3 and 5.3), a compensating divergence in the \mathbf{k} -dependence of the self-energy with

$$\frac{\partial \Sigma'}{\partial \mathbf{k}} \sim \frac{1}{x} \quad (147)$$

automatically shows up. This limiting behaviour of v_F and Z is also experimentally observed and transcends conventional Landau–Fermi liquid behaviour, where the \mathbf{k} -dependence of the self-energy is usually small.

Equation (147) constitutes a key experimental result for the HTSCs, because ARPES shows unambiguously that $v_F \rightarrow \text{constand}$ and $Z \rightarrow 0$ for $x \rightarrow 0$ (see [23, 24, 37, 39]). The fact that (147) arises naturally within the Gutzwiller–RVB framework provides a strong argument for the basic premise of the theory. It is a consequence of the vanishing of the number of free charge carriers $\sim 1 - n$ due to the projection close to half-filling. The number of charge carriers is, in contrast, $\sim n$ and not singular within normal Fermi liquid theory. These considerations lead to further consequences for higher-energy features of the one-particle self-energy, which have been explored by Randeria *et al.* [219].

6.2. Calculation of the QP weight within RMFT

To evaluate the QP weight in (141) and (142) within RMFT, one can follow [6] and use the GA for partially projected states as presented in section 3.3. Here, we briefly discuss the mean steps required for this calculation and refer to Fukushima *et al.* [6] for more details. For simplicity, one may work with a particle excitation,

$$|\Psi_{\mathbf{k}\sigma}^{N+1}\rangle = P_{N+1} P_{G\mathbf{k}\sigma}^\dagger |\Psi_0\rangle, \quad (148)$$

and a hole excitation,

$$|\Psi_{\mathbf{k}\sigma}^{N-1}\rangle = P_{N-1}P_G c_{-\mathbf{k}-\sigma}|\Psi_0\rangle. \quad (149)$$

Note that this redefinition does not effect the final results because all calculations include norms and $\gamma_{\mathbf{k}\sigma}^\dagger|\Psi_0\rangle \sim c_{\mathbf{k}\sigma}^\dagger|\Psi_0\rangle \sim c_{-\mathbf{k}-\sigma}|\Psi_0\rangle$ for a BCS wave function $|\Psi_0\rangle$.

The first step in the calculation of the QP weight is the determination of the norms

$$N_{\mathbf{k}\sigma}^{N\pm 1} = \langle \Psi_{\mathbf{k}\sigma}^{N\pm 1} | \Psi_{\mathbf{k}\sigma}^{N\pm 1} \rangle$$

of the excitations $|\Psi_{\mathbf{k}\sigma}^{N\pm 1}\rangle$. Invoking GA for partially projected states (see section 3.3), one finds [6]

$$\frac{N_{\mathbf{k}\sigma}^{N+1}}{N_G^N} \approx g_t(1 - n_{\mathbf{k}\sigma}^0), \quad \frac{N_{-\mathbf{k}-\sigma}^{N-1}}{N_G^N} = \frac{n_{\mathbf{k}\sigma}^0}{g_t}, \quad (150)$$

where $g_t = (1 - n)/(1 - n_\sigma)$, $N_G^N = \langle \Psi^N | \Psi^N \rangle$, and $n_{\mathbf{k}\sigma}^0 \langle c_{\mathbf{k}\sigma}^\dagger c_{\mathbf{k}\sigma} \rangle_{\Psi_0}$ is the momentum distribution function in the unprojected wave function. It should be noted that the above result was derived for the non-magnetic case $n_\sigma = n_\uparrow = n_\downarrow = n/2$.

After calculating the normalization, one can use the same techniques to obtain [6]

$$\frac{\langle \Psi_0 | c_{\mathbf{k}\sigma} P_G P_{N+1} c_{\mathbf{k}\sigma}^\dagger P_N P_G | \Psi_0 \rangle}{N_G^N} \approx g_t(1 - n_{\mathbf{k}\sigma}^0), \quad (151)$$

$$\frac{\langle \Psi_0 | c_{\mathbf{k}\sigma}^\dagger P_{N-1} P_G c_{\mathbf{k}\sigma} P_G P_N | \Psi_0 \rangle}{N_G^N} \approx n_{\mathbf{k}\sigma}^0, \quad (152)$$

for the numerators in the equations for the QP weights, (141) and (142). Using (151), (152) and the normalizations in (141) and (142), we find the QP weights of particle- and the hole-like excitations,

$$Z_{\mathbf{k}}^+ u_{\mathbf{k}}^2 = \frac{|\langle \Psi_{\mathbf{k}\sigma}^{N+1} | c_{\mathbf{k}\sigma}^\dagger | \Psi_0^N \rangle|^2}{\langle \Psi_{\mathbf{k}\sigma}^{N+1} | \Psi_{\mathbf{k}\sigma}^{N+1} \rangle \langle \Psi_0^N | \Psi_0^N \rangle} \approx g_t(1 - n_{\mathbf{k}\sigma}^0), \quad (153)$$

$$Z_{\mathbf{k}}^- v_{\mathbf{k}}^2 = \frac{|\langle \Psi_{-\mathbf{k}-\sigma}^{N-1} | c_{\mathbf{k}\sigma} | \Psi_0^N \rangle|^2}{\langle \Psi_{-\mathbf{k}-\sigma}^{N-1} | \Psi_{-\mathbf{k}-\sigma}^{N-1} \rangle \langle \Psi_0^N | \Psi_0^N \rangle} \approx g_t n_{\mathbf{k}\sigma}^0, \quad (154)$$

respectively. As $n_{\mathbf{k}\sigma}^0 = v_{\mathbf{k}}^2 = 1 - u_{\mathbf{k}}^2$, it follows $Z_{\mathbf{k}}^+ \approx Z_{\mathbf{k}}^- \approx g_t$, which vanishes at half-filling $n \rightarrow 1$.

The above results show that within the GA, the coherent QP weight does not cause particle-hole asymmetry, i.e. $Z_{\mathbf{k}}^+ \approx Z_{\mathbf{k}}^-$. It seems, therefore, that the asymmetric DOS observed in STM can only be explained by the incoherent spectrum of Gutzwiller projected superconductors. A symmetric spectral weight for coherent QP excitations is also obtained in calculations for the Hubbard model (include the transformation e^{-iS} ; see [7, 206]. However, the RMFT results for $\tilde{Z}_{\mathbf{k}}^+ = Z_{\mathbf{k}}^+ u_{\mathbf{k}}^2$ and $\tilde{Z}_{\mathbf{k}}^- = Z_{\mathbf{k}}^- v_{\mathbf{k}}^2$ do not exactly match recent VMC calculations [209–212], which directly evaluate $\tilde{Z}_{\mathbf{k}}^+$ and $\tilde{Z}_{\mathbf{k}}^-$ (see section 7.1). Nevertheless, the general doping dependence of above QP weight qualitatively agrees with VMC results and with the coherent weight seen in ARPES measurements [7].

6.3. QP weight for the Hubbard model in the strong coupling limit

In the previous section, we illustrated how one can determine the QP within the GA. Here, we follow [7, 206] and extend this calculation to the Hubbard Hamiltonian, in analogy to the extensions of the RMFT discussed in section 4.3. By using a re-transformed ground state, $|\Psi\rangle \equiv e^{-iS} P_G P_N |\Psi_0\rangle$ as well as re-transformed excited states,

$$|\Psi_{\mathbf{k}\sigma}^{N\pm 1}\rangle \equiv e^{-iS} P_G P_{N\pm 1} \gamma_{\mathbf{k}\sigma}^\dagger |\Psi_0\rangle, \quad (155)$$

we can systematically study the QP weight renormalization within the Hubbard model in the strong coupling limit. Evaluating the canonical transformation e^{-iS} in order $\mathcal{O}(t/U)$ gives the following particle–hole symmetric QP weight renormalization [7], $Z_{\mathbf{k}} = Z_{\mathbf{k}}^+ = Z_{\mathbf{k}}^-$,

$$Z_{\mathbf{k}} \approx g_t + \frac{g_3}{U} \left(\frac{1-x^2}{2} \epsilon_{\mathbf{k}}^0 + \frac{3-x}{L} \sum_{\mathbf{k}'} v_{\mathbf{k}}^2 \epsilon_{\mathbf{k}'}^0 \right), \quad (156)$$

with $\epsilon_{\mathbf{k}}^0 = 2t(\cos k_x + \cos k_y) + 4t' \cos k_x \cos k_y$. Equation (156) also includes corrections from the next-nearest-neighbour hopping term t' . The renormalization $Z_{\mathbf{k}}$ of the nodal QP weight is plotted as a solid curve in figure 44, and agrees well with VMC results for the Hubbard model [21]. The dashed curve corresponds to the RMFT result for the t – J model, $Z_{\mathbf{k}} = g_t$, which is compared with the dotted curve, $Z_{\mathbf{k}} = x$, from SBMFT.

The spectral weight of the coherent peak, measured in ARPES, is related to the QP weight $\tilde{Z}_{\mathbf{k}} = Z_{\mathbf{k}} n_{\mathbf{k}\sigma}^0$; it is shown in figure 45(a) along the directions $(0, 0) \rightarrow (\pi, 0)$, $(\pi, 0) \rightarrow (\pi, \pi)$ and $(\pi, \pi) \rightarrow (0, 0)$ for different x . As seen in the figure, the QP spectral weight is severely modified by Gutzwiller projection. It decreases with doping and vanishes at half-filling. This causes a shift of spectral weight to an incoherent background as seen in the momentum distribution function,

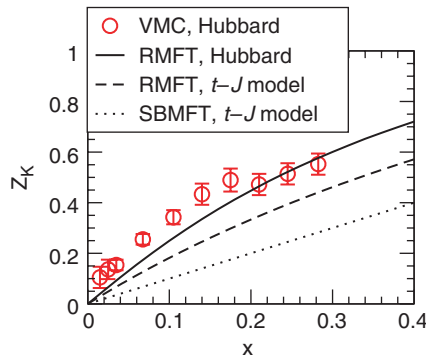


Figure 44. Renormalization $Z_{\mathbf{k}}$ of the Gutzwiller–Bogoliubov nodal QP as a function of doping x . The model parameters are $t = -t'/4$ and $U = 12t$. RMFT results for the Hubbard and the t – J model are compared with VMC data for the Hubbard model (from [21]) and with the SBMFT result in the t – J model. Reprinted with permission from [7] © 2006 by the American Physical Society.

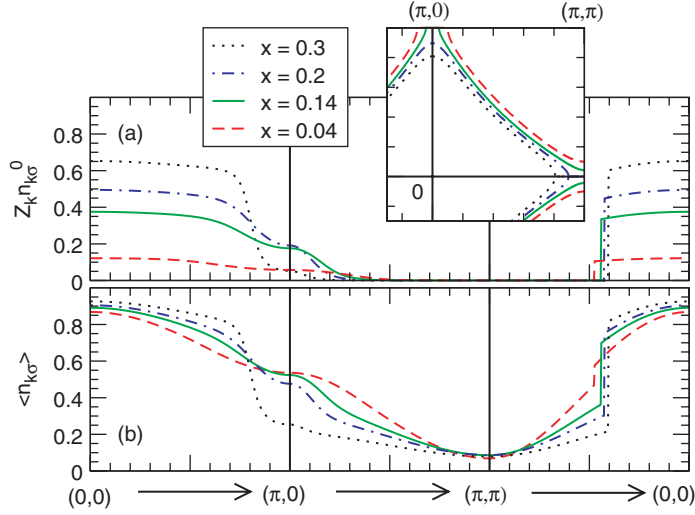


Figure 45. (a) QP weight $Z_{\mathbf{k}} n_{\mathbf{k}\sigma}^0$ and (b) momentum distribution $\langle n_{\mathbf{k}\sigma} \rangle$ of the Gutzwiller–Bogoliubov QP for different doping x . The corresponding FS, $\xi_{\mathbf{k}} = 0$, is shown in the inset of (a). The model parameters are $t = -t'/4$ and $U = 12t$. Reprinted with permission from [7] © 2006 by the American Physical Society.

$\langle n_{\mathbf{k}\sigma} \rangle \approx Z_{\mathbf{k}} v_{\mathbf{k}}^2 + n_{\mathbf{k}\sigma}^{\text{inc}} + \mathcal{O}(t/U)^2$. While the first term corresponds to the coherent QP weight, the second gives the distribution of the incoherent part. One obtains [7]

$$n_{\mathbf{k}\sigma}^{\text{inc}} \approx \frac{(1-x)^2}{2(1+x)} + \sum_{\tau} \frac{t_{\tau}}{2U} \cos(\mathbf{k}\tau) \left[\frac{(1-x)^3}{1+x} + \left(\frac{3g_s + 1}{2} - g_3 \frac{3+x}{2} \right) |\tilde{\Delta}_{\tau}|^2 + \left(\frac{3g_s - 1}{2} - g_3 \frac{3-x}{2} \right) \tilde{\xi}_{\tau}^2 \right], \quad (157)$$

which is a smooth function of \mathbf{k} , where $\tilde{\Delta}_{\tau}$ and $\tilde{\xi}_{\tau}$ are the pairing and hopping amplitudes between nearest- and next-nearest-neighbour sites, $\tau = (\pm 1, 0)$, $(0, \pm 1)$, $(\pm 1, \pm 1)$, as defined in section 4. Results are shown in figure 45(b). The incoherent weight is spread over the entire Brillouin zone and overlies the coherent part from the Gutzwiller–Bogoliubov QPs. At half-filling, all weight becomes incoherent. These results are in qualitative agreement with calculations for the t – J model (recovered by neglecting the t/U corrections in above equations).

6.3.1. Non-monotonic behaviour of the QP weight at $(\pi, 0)$. Here, we consider the coherent QP weight $Z_{\mathbf{k}} v_{\mathbf{k}}^2$ at the antinodal point $\mathbf{k} = (\pi, 0)$ within the Hubbard model in the strong coupling limit ($U = 12t$). The RMFT theory predicts a non-monotonic behaviour as a function of doping, shown in figures 45(a) and 46. This effect arises from a combination of the effects due to the Gutzwiller projection and to the topology change (see the inset of figure 45(a)) of the underlying FS; figure 46(a) illustrates this clearly. While the QP weight renormalization, $Z_{\mathbf{k}}$, increases with increasing doping, $n_{\mathbf{k}}^0 = v_{\mathbf{k}}^2$, decreases owing to the topology change, which occurs at $x \approx 0.15$ – 0.20 for our choice of hopping parameters ($t' = -t/4$). The change of the

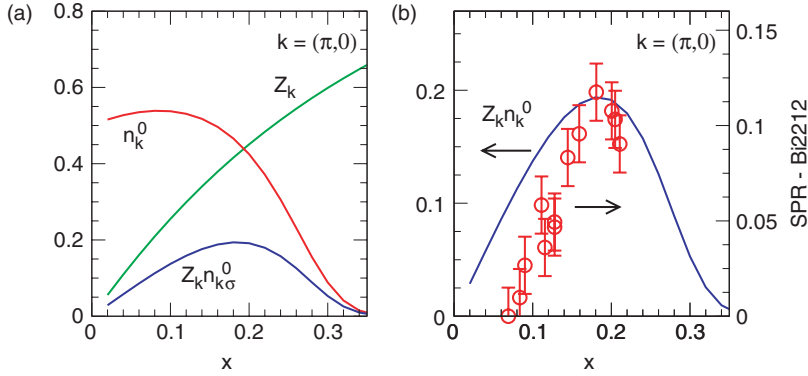


Figure 46. Doping dependence at the antinodal point, $\mathbf{k} = (\pi, 0)$: (a) QP renormalization Z_k , the unrenormalized QP weight, $n_{k\sigma}^0 = v_k^2$, and the renormalized coherent QP weight $Z_k v_k^2$; (b) coherent weight $Z_k v_k^2$ compared with the experimentally determined SPR (the ratio of coherent spectral weight relative to the total spectral weight) for Bi2212 [37]; see also figure 8. The model parameters are $t = -t'/4$ and $U = 12t$. Reprinted with permission from [7] © 2006 by the American Physical Society.

FS seems to be a generic feature of hole-doped cuprates [220, 221], although the exact doping concentration x for which this occurs is sensitive to the ratio between various hopping parameters. The combined effect of strong correlations and topology change leads to a maximum of the QP weight for the doping level, x , at which the underlying FS changes topology. Indications for such a behaviour have been seen in ARPES [37, 38]. Feng *et al.* [37] extracted the SPR (illustrated in figure 46(b)), which is proportional to the coherent QP spectral weight, $Z_k v_k^2$. They found that the SPR increases with small x , attains a maximum value around $x \approx 0.2$ where it begins to decrease. Ding *et al.* [38], reported similar results from ARPES. In figure 46(b), the SPR experimentally drops below the theoretical prediction for underdoped samples. This is likely to be the effect of inhomogeneities and of the resulting gap variations [54], which cause a strong scattering of QPs near the antinodes.

Although the topology change does not influence the stability of the superconducting state within RMFT, the superconducting pairing parameter Φ (related to T_c) and the QP weight $Z_k v_k^2$ show some similarity as a function of doping. However, we emphasize that this similarity does not result from any direct relation between these two quantities.

6.4. QP current renormalization

An important issue in the theory of the HTSCs are the properties of the nodal quasiparticle (NQP) excitations, in particular the renormalization of the respective QP current [222] and their role in suppressing the superfluid density ρ_s . As pointed out by several authors [223–225], the proliferation of NQPs at finite temperatures decreases $\rho_s(T)$ [223],

$$\frac{\rho_s(T)}{m} = \frac{\rho_s^{(0)}}{m} - \frac{2 \ln 2}{\pi} \alpha^2 \left(\frac{v_F}{v_2} \right) T, \quad (158)$$

where v_F and v_2 are the NQP velocities in the longitudinal and transverse directions, respectively, and $\rho_s^{(0)}$ is the zero-temperature superfluid density. The renormalization factor α (also called the effective charge [225]) relates the current carried by the QP to its velocity,

$$\mathbf{j}(\mathbf{k}) = -e\alpha\mathbf{v}(\mathbf{k}).$$

Assuming that superconductivity is destroyed by thermal NQPs, T_c is determined by simply setting (158) to zero, i.e. determining the temperature at which the superfluid density vanishes [223, 224]. The behaviour of T_c as a function of doping is then governed by the doping dependencies of the various quantities in (158). The latter can be calculated within the framework of the RVB theory. Numerical calculations [21] show that $\rho_s^{(0)} \rightarrow 0$ as $x \rightarrow 0$. The nodal velocity v_F is approximately constant [7], whereas the transverse velocity v_2 increases as the insulator ($x=0$) is approached. The situation is rather unclear for the renormalization factor α . While some theories argue for a constant α [225], recent experimental (measurement of the superfluid density [226]) as well as theoretical results [10, 208] seem to support the conclusion that α decreases as $x \rightarrow 0$.

To clarify this issue, Edegger *et al.* [10] used RMFT to calculate the current renormalization for the t - J model with $J = t/3$. For the superfluid density at zero temperature, RMFT yields a doping dependence of,

$$\rho_s^{(0)} \sim g_t \equiv \frac{2x}{1+x}, \quad (159)$$

where we used [202],

$$\rho_s^{(0)} \sim \left\langle \sum_{\sigma} t_{\tau} (c_{i+\tau, \sigma}^{\dagger} c_{i, \sigma} + c_{i, \sigma}^{\dagger} c_{i+\tau, \sigma}) \right\rangle_{\Psi}, \quad (160)$$

and evaluated (160), invoking the GA. Here, we used $\tau = \hat{x}, \hat{y}$ and neglected corrections due to the re-transformation e^{-iS} of the wave function to the Hubbard model, i.e. we set $e^{-iS} = 1$. Using linear response theory for the superfluid density [202] and restricting ourselves to low temperatures, we recover (158) within RMFT [10]. The renormalization factor α can be derived by considering the current carried by the Gutzwiller projected Bogoliubov QP states $|\Psi_{\mathbf{k}\sigma}\rangle$,

$$\mathbf{j}(\mathbf{k}) \equiv ie \left\langle \sum_{\langle ij \rangle, \sigma} t_{ij} (c_{i, \sigma}^{\dagger} c_{j, \sigma} - c_{j, \sigma}^{\dagger} c_{i, \sigma}) \right\rangle_{\Psi_{\mathbf{k}\sigma}}. \quad (161)$$

By invoking the Gutzwiller renormalization scheme, we find

$$\mathbf{j}(\mathbf{k}) = -eg_t \frac{d}{dk} \epsilon^0(\mathbf{k}), \quad (162)$$

where $\epsilon^0(\mathbf{k})$ is the unrenormalized tight binding dispersion relation; again we set $e^{-iS} = 1$ for simplicity, i.e. we neglect any t/U -corrections in (161) and (162). Combining (159) and (162) allows us to extract α . At the nodal point, one finds $\alpha = g_t v_F^0 / v_F$, where v_F^0 is the unrenormalized Fermi velocity. The results are shown in figures 47 and 48, along with VMC data taken from [208]. As can be seen, both methods are in excellent agreement and show that the renormalization factor $\alpha \rightarrow 0$, as $x \rightarrow 0$. As the x dependence of the superfluid stiffness can be obtained

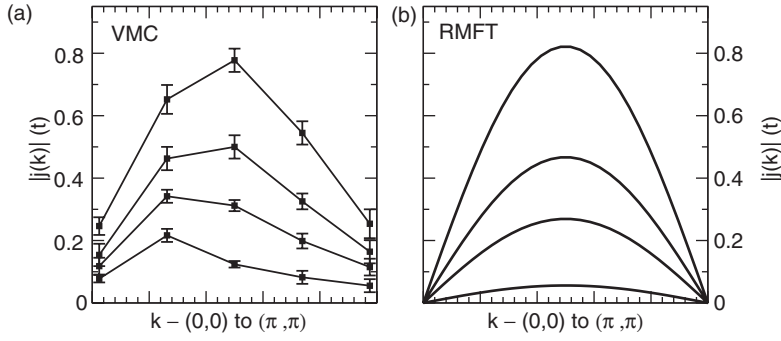


Figure 47. The magnitude of the current $|j(k)|$ along the nodal direction, $(0,0)$ to (π, π) . (a) VMC calculations on a 10×10 lattice (data taken from [208]) and (b) RMFT results are compared for the doping levels $x = 0.01, 0.05, 0.09$ and 0.17 (increasing magnitude). Reprinted with permission from [10] © 2007 by Elsevier.

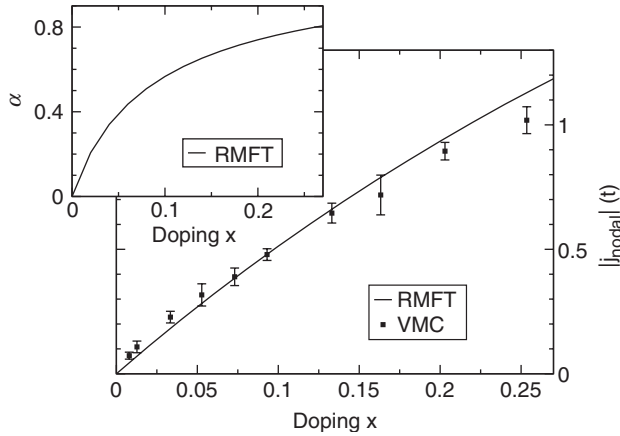


Figure 48. Magnitude of the nodal current as a function of doping. RMFT results are compared with the VMC calculations on a 20×20 lattice (data taken from [208]). Inset: RMFT result for the current renormalization factor, $\alpha \equiv |j_{\text{nodal}}|/v_F$, as a function of doping x . Reprinted with permission from [10] © 2007 by Elsevier.

experimentally, it is important to study $d\rho_s(T)/dT \propto \alpha^2 v_F/v_2$. We show the results for this quantity in figure 49(a). Note that $v_F/v_2 \propto v_F/\Delta_{\text{SC}}$ already shows a significant x -dependence and may explain the experimentally observed doping dependence of $d\rho_s(T)/dT$ (see [226]). However, multiplication by α^2 leads to a slope $d\rho_s(T)/dT$ that vanishes as $x \rightarrow 0$, i.e. as $x \rightarrow 0$, the effective NQP charge vanishes faster than the superfluid density does. Therefore, we get a meaningless estimate for T_c by setting (158) to zero as shown in figure 49.

This problem was noted by Lee and Wen [223, 224] in the context of the U(1) gauge theory of the t - J model. They argued that an SU(2) formulation may resolve the problem, yielding a constant α . However, a constant α does not completely agree

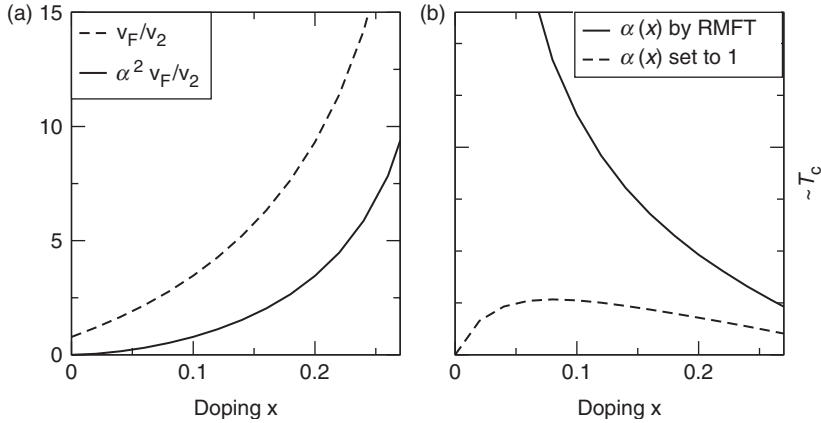


Figure 49. (a) Doping dependence of v_F/v_2 and $\alpha^2 v_F/v_2$ from RMFT with $t' = -0.2t$ and $U = 12t$ in the large U Hubbard model. (b) Doping dependence of T_c from setting (158) to zero: solid curve, $\alpha(x)$ from RMFT; dashed curve, $\alpha(x)$ is set equal to one by hand. Reprinted with permission from [10] © 2007 by Elsevier.

with the experimentally observed x -dependence of the superconducting dome either (maximal T_c at $x \approx 0.08$, see figure 49(b)). There are several possible reasons for the discrepancy. It may be that the RMFT result for α is indeed correct, in which case the issue can be resolved by more experiments explicitly extracting α in the underdoped regime. This would automatically mean that T_c is not determined by NQPs, i.e. (158), and that one needs to look for other possibilities such as vortex proliferation as mechanisms that set the scale for T_c .

Another possibility is that the theoretical framework behind the Gutzwiller–RVB theory misses a crucial ingredient in the derivation of (158) and the calculation of the effective current renormalization α . Indeed, the applicability of the standard Kubo formula for ρ_s [202] in a projected Hilbert space may be questioned and one needs to reexamine this calculation carefully to check whether (158) is indeed correct.

A recent more phenomenological approach argues that the overall temperature dependence of the superfluid density at low dopings is well described by a three-dimensional strongly anisotropic weakly interacting Bose gas [227]. However, more work is necessary to connect such phenomenological models to the RVB theory we have outlined so far.

6.5. Determining the underlying FS of strongly correlated superconductors

The underlying FS in the HTSCs was studied recently by Gros *et al.* [9] and Sensarma *et al.* [228]. These results clarify the notion of a FS in a superconducting state and what it means when we say that ARPES measures the FS of a superconductor.

In the case of the HTSCs, owing to the large superconducting gap (pseudogap) below (above) the superconducting transition temperature, an FS can be defined only along the nodal directions (the so-called Fermi arcs [23, 24, 41–43]). The full ‘underlying FS’ emerges only when the pairing interactions are turned off, either by a

Gedanken experiment or by raising the temperature. Its experimental determination presents a great challenge because ARPES is more accurate at lower temperatures. Therefore, it is of importance to know what exactly is measured by ARPES in a superconducting or in a pseudogap state of the HTSCs.

6.5.1. Fermi versus Luttinger surface. We follow [9] and begin by highlighting the differences between a Fermi and a Luttinger surface. The FS is determined by the poles of the one-electron Green's function $G(\mathbf{k}, \omega)$, namely, by $\text{Re}G(\mathbf{k}, \omega = 0) \equiv \pm\infty$ (see [229]). The Luttinger surface is defined as the locus of points in reciprocal space, where the real part of the one-particle Green's function changes sign [230]. In the Fermi liquid state of normal metals, the Luttinger surface coincides with the FS. In a Mott–Hubbard insulator the Green's function changes sign owing to a characteristic $1/\omega$ divergence of the single-particle self-energy [231–233] at momenta \mathbf{k} of the non-interacting FS. In the HTSCs the gapped states destroy the FS but only mask the Luttinger surface. Hence, it seems natural to relate the Luttinger surface of the superconducting and of the pseudogap states with the concept of an ‘underlying FS’ and ask whether such a surface can be determined by ARPES.

The single particle Green's function is given by

$$G(\mathbf{k}, \omega) \equiv \sum_n \frac{|\langle n | c_{\mathbf{k}\sigma}^\dagger | 0 \rangle|^2}{\omega - (E_n - E_0) + i0^+} + \sum_n \frac{|\langle n | c_{\mathbf{k}\sigma} | 0 \rangle|^2}{\omega + (E_n - E_0) + i0^+}, \quad (163)$$

where E_n are the eigenvalues corresponding the eigenstates $|n\rangle$ of the Hamiltonian; the ground state and its energy are given by $|0\rangle$ and E_0 , respectively. In order to perform explicit analytic calculations one can approximate the coherent part of (163) by the RMFT results for the Hubbard model (see sections 4.3 and 6.3). In analogy to section 6.1.2 for the spectral function $A(\mathbf{k}, \omega)$, we can use $Z_{\mathbf{k}} u_{\mathbf{k}}^2 = |\langle n | c_{\mathbf{k}\sigma}^\dagger | 0 \rangle|^2$, $Z_{\mathbf{k}} v_{\mathbf{k}}^2 = |\langle n | c_{\mathbf{k}\sigma} | 0 \rangle|^2$ and $E_{\mathbf{k}} = E_n - E_0$. Thus, the RMFT result for the coherent part of the Green's function becomes

$$G(\mathbf{k}, \omega) \approx \frac{Z_{\mathbf{k}} u_{\mathbf{k}}^2}{\omega - E_{\mathbf{k}} + i0^+} + \frac{Z_{\mathbf{k}} v_{\mathbf{k}}^2}{\omega + E_{\mathbf{k}} + i0^+}. \quad (164)$$

Within RMFT the elementary excitations in the superconducting d -wave ground state are given by the dispersion relation

$$E_{\mathbf{k}} = \sqrt{\xi_{\mathbf{k}}^2 + \Delta_{\mathbf{k}}^2}, \quad (165)$$

where $\xi_{\mathbf{k}}$ and $\Delta_{\mathbf{k}}$ are determined by (108) and (109), respectively. Evaluating $\text{Re}G(\mathbf{k}, \omega = 0)$ by (164) one finds

$$\text{Re} G(\mathbf{k}, \omega = 0) = \frac{Z_{\mathbf{k}}}{E_{\mathbf{k}}} (v_{\mathbf{k}}^2 - u_{\mathbf{k}}^2) = -\frac{Z_{\mathbf{k}}}{E_{\mathbf{k}}^2} \xi_{\mathbf{k}}, \quad (166)$$

where the right-hand side follows from the mean-field relation, $v_{\mathbf{k}}^2 = 1 - u_{\mathbf{k}}^2 = (1 - \xi_{\mathbf{k}}/E_{\mathbf{k}})/2$ (see equation (97)). The poles of $\text{Re}G(\mathbf{k}, \omega = 0)$, which determine the FS, are therefore given by

$$E_{\mathbf{k}} \equiv 0. \quad (167)$$

However, for a d -wave superconductor, equation (167) is fulfilled only at the nodal points; consequently, a FS is well defined solely at these points. Alternatively, one can consider the Luttinger surface, defined by sign changes in the Green's functions at $\omega=0$. From (166), sign changes are found whenever

$$\xi_{\mathbf{k}} \equiv 0. \quad (168)$$

From above equations, we conclude that the Luttinger surface is determined by the condition $\xi_{\mathbf{k}} \equiv 0$, which is also the definition of the normal state FS when $\Delta_{\mathbf{k}} \equiv 0$.

6.5.2. FS determination. There are several ways to determine the FS in practice. However, these methods do not coincide with the underlying FS, namely, the Luttinger surface, in the HTSCs owing to the large superconducting gap (or large pseudogap) in the underdoped regime.

To demonstrate this fact, we follow [9, 228] and discuss the so-called ‘maximal intensity method’ in more detail. In this approach the intensity of ARPES spectra at zero frequency is used to map out the underlying FS. This quantity is determined by $A(\mathbf{k}, \omega=0) = -\pi^{-1} \text{Im}G(\mathbf{k}, \omega=0)$, which becomes

$$\sim \frac{\Gamma_{\mathbf{k}}}{E_{\mathbf{k}}^2 + \Gamma_{\mathbf{k}}^2}, \quad (169)$$

if one replaces 0^+ by a finite broadening $\Gamma_{\mathbf{k}}$ in (164). The $\Gamma_{\mathbf{k}}$ is determined both by the experimental resolution and the width of the QP peak. When the momentum dependence of $\Gamma_{\mathbf{k}}$ is small compared with that of $E_{\mathbf{k}}$ (as is usually the case), the maximal intensity is given by the set of momenta $\hbar\mathbf{k}$ for which $E_{\mathbf{k}}$ is minimal.

This method in determining the underlying FS was examined in [9] by calculating (169) within RMFT for a strongly correlated d -wave superconducting state. All calculations in [9] were done with model parameters for HTSCs using RMFT [7, 20], for which the QP dispersion $E_{\mathbf{k}}$ retains the form of (165). Figure 50 shows results for the spectral intensity at zero frequency as well as the locus of the Luttinger surface, where the former is deduced from the inverse of $E_{\mathbf{k}}$.

For large hole doping, $x=0.25$, the superconducting gap is small and the Luttinger surface is close to the points in momentum space for which the zero-frequency intensity is maximal. However, for smaller doping, $x=0.05$, the gap is substantial and the Luttinger surface deviates qualitatively from the maximal intensity surface owing to the momentum dependence of $\Delta_{\mathbf{k}}$ (see the ridges in figure 50). It follows that when the gap or the pseudogap is large, the criterion of maximal spectral intensity alone does not suffice to identify the correct FS and it is necessary to supplement the analysis of the zero-frequency ARPES intensity, (169), with a dispersion relation such as (165). These considerations explain why the (outer) maximal intensity ridges seen in ARPES (at low temperatures in the underdoped regime) may yield an underlying FS whose volume is too large. In particular, this effect is seen in $\text{Ca}_{2-x}\text{Na}_x\text{CuO}_2\text{Cl}_2$ (see [234]), which also exhibits quite a large pseudogap [235].

As discussed by Gros *et al.* [9], even larger deviations from the underlying FS are present in the ‘maximal gradient method’. This method is based on the fact that the FS is given by the set of \mathbf{k} values for which the momentum distribution function $n_{\mathbf{k}}$ shows a jump discontinuity. When this discontinuity is smeared out, say by thermal broadening or a small gap, the gradient of $n_{\mathbf{k}}$, $|\nabla_{\mathbf{k}}n_{\mathbf{k}}|$, is assumed to be maximal at the

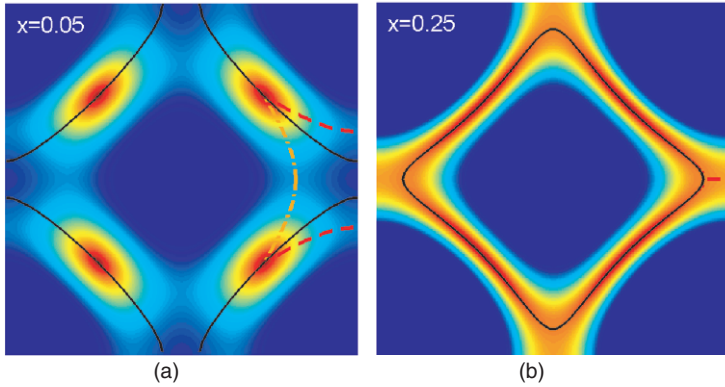


Figure 50. The zero-frequency spectral intensity (deduced from the inverse of $E_{\mathbf{k}}$, which was determined by RMFT with model parameters $t' = -t/4$ and $U = 12t$) in the first Brillouin zone for hole dopings (a) $x = 0.05$ and (b) $x = 0.25$. The colour coding blue/red corresponds to the low/high zero-frequency spectral intensity. The ridges of maximal intensity are indicated by the (dashed) red and (dashed-dotted) orange lines, respectively, and the Luttinger surface is indicated by the black line. Reprinted with permission from [9] © 2006 by PNAS. See online version for colour.

locus of the underlying FS. However, this method is very sensitive to the presence of even small gaps [9] and cannot be used to determine the underlying FS unambiguously from numerical [236, 237] or ARPES data [238, 239]. Furthermore, we note that even the Luttinger surface in the HTSCs can slightly violate the Luttinger count. This surprising result is discussed in [9] and [228] in more detail.

Bieri and Ivanov [211] recently proposed an alternative definition of the underlying FS \mathbf{k}_F by the condition $\tilde{Z}_{\mathbf{k}_F}^- = \tilde{Z}_{\mathbf{k}_F}^+$, namely, that the quasi-particle and the quasi-hole weight coincide at the FS, as they do for a Fermi liquid state (see section 6.1 for the definition of $\tilde{Z}_{\mathbf{k}}^\pm$). This definition also agrees with the Luttinger surface, $\xi_{\mathbf{k}} \equiv 0$, within RMFT. However, when considering a Gutzwiller-projected superconducting state within the VMC technique deviations from the Luttinger surface are observed [211]. This deviations stem from the asymmetry between $\tilde{Z}_{\mathbf{k}}^+$ and $\tilde{Z}_{\mathbf{k}}^-$, which shows up in the VMC calculations only.

6.5.3. Renormalization of the FS towards perfect nesting. The presence of strong electron–electron interactions also changes the geometry of the Luttinger surface close to half-filling. The Cu–O planes of the HTSCs are characterized by a nearest-neighbour hopping parameter $t \approx 300 \text{ meV}$ and a next-nearest-neighbour hopping parameter $t' \approx -t/4$. These parameters are the bare parameters and determine the dispersion relation

$$\epsilon_{\mathbf{k}} = -2t(\cos k_x + \cos k_y) - 2t'(\cos(k_x + k_y) + \cos(k_x - k_y)), \quad (170)$$

in the absence of any electron–electron interaction. On the other hand, true hopping processes are influenced by the Coulomb interaction (here $U = 12t$) leading to a renormalization of the effective hopping matrix elements,

$$t \rightarrow \tilde{t} = \tilde{t}(U), \quad t' \rightarrow \tilde{t}' = \tilde{t}'(U). \quad (171)$$

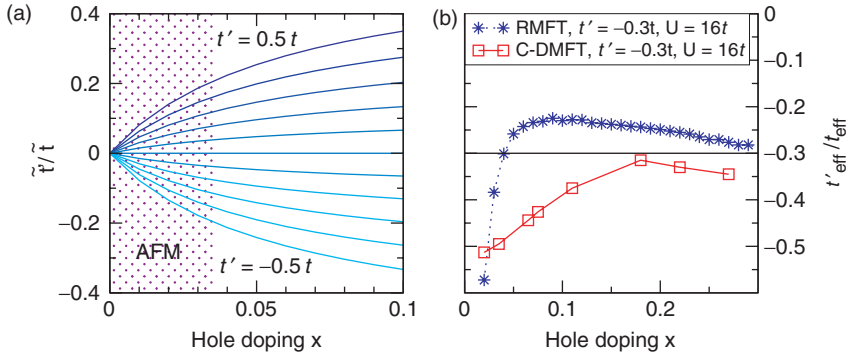


Figure 51. (a) Renormalization of the next-nearest-neighbour hopping amplitude, $t' \rightarrow \tilde{t}$, as a function of hole-doping concentration x for various values of bare t' . All effective \tilde{t} are renormalized to zero at half-filling by the large Coulomb repulsion. We highlight the region for which we expect the superconducting d -wave state to become unstable against antiferromagnetism (AFM) owing to the nearly perfect nesting of the Luttinger surface. RMFT calculations with $U = 12t$. From [9]. (b) Determination of t'_{eff} by a fit to the maximal intensity surface, see figure 50. We compare RMFT calculations with Cluster-DMFT (C-DMFT) calculations from Civelli *et al.* [240] for $t' = -0.3t$ (indicated by the black line) and $U = 16t$.

One can extract \tilde{t} and \tilde{t}' from the RMFT dispersion $\xi_{\mathbf{k}}$ in (108), see section 4.3, and finds close to half-filling $\tilde{t} \propto J = 4t^2/U$ and $\tilde{t}' \rightarrow 0$, i.e. the next-nearest-neighbour hopping is renormalized to zero. This behaviour is illustrated in figure 51(a). The resulting Luttinger surface renormalizes to perfect nesting. A similar behaviour has been observed in recent variational studies of organic charge transfer-salt superconductors [94].

At half-filling the Hubbard model reduces to a spin-model with nearest neighbour $J = 4t^2/U$ and a frustrating next-nearest neighbour $J' = 4(t')^2/U$. The ground state wave function obeys the so-called Marshall sign rule[†] in the absence of frustration, $J' = 0$, namely when the underlying FS is perfectly nested by the reciprocal magnetic ordering vector $\mathbf{Q} = (\pi, \pi)$ (in units of the inverse lattice constant). Hence, any deviation from the Marshall sign rule as a function of the frustrating J' can be used to determine the degree of effective frustration present in the ground state. We emphasize this is a qualitative statement of the ground state wave function. A numerical study has found that the Marshall sign rule remains valid even for small but finite J' , namely, the effective frustration renormalizes to zero [242]. Such a behaviour is in agreement with the results presented in figure 51(a).

However, we note that the renormalization to perfect nesting was not seen in Cluster-DMFT (C-DMFT) studies, e.g. by Civelli *et al.* [240]. We believe that these

[†]Marshall [241] showed that the ground state of the spin- $\frac{1}{2}$ Heisenberg Hamiltonian on any bipartite lattice will be a singlet. Furthermore, the ground state wave function picks up a sign whenever two antiparallel spins from different sublattices are interchanged. This is the Marshall sign rule.

discrepancies stem from the way of fitting the effective next-nearest-neighbour hopping t'_{eff} . Within the C-DMFT study of Civelli *et al.* the FS is determined very similarly than within the maximal intensity method. Therefore, deviations from the effective \tilde{t} of the Luttinger surface (shown in figure 51(a)) are unsurprising. In figure 51(b), we compare the effective next-nearest-neighbour hopping t'_{eff} determined by a fit to the maximal intensity surface (see figure 50, outer ridges) with the C-DMFT results [240]. Both methods show a qualitatively very similar doping dependence. When approaching half-filling $|t'_{\text{eff}}|$ first decreases, but then starts to grow rapidly in the underdoped regime. We associate this effect with the increasing influence of the d -wave gap in the maximal intensity surface at small doping. The above considerations show that the determination of the underlying FS in the HTSCs is a tricky task, where special care is required when comparing data from different approaches.

7. QP states within the VMC scheme

VMC calculations for the QP weight in the t – J model only agree qualitatively with the approximative RMFT results. Minor deviations from the RMFT studies may explain a contribution of the coherent excitations to the distinct particle–hole asymmetry seen in the STM spectra. Apart from the QP weight, we also discuss excitation energies determined by VMC calculations, which match well with previous RMFT results.

7.1. Direct calculation of the QP weight

RMFT together with GA is an useful tool to analyse QP features in strongly correlated superconducting states. However, the RMFT and GA are approximate methods and it is desirable to check their predictions numerically by VMC calculations. This consideration motivated several authors [207–212] to calculate the QP weight, (141) and (142) directly by evaluating appropriate expectation values within the projected wave function $|\Psi\rangle$. These VMC studies confirm the RMFT prediction that the QP weight decreases towards half-filling, where it finally vanishes. However, as we show below, the VMC results reveal some limitations of the RMFT concerning the determination of the detailed doping- and \mathbf{k} -dependence of the QP weight. We note that most of the VMC calculations presented below do not include a re-transformed trial wave function and describe observables in the t – J model. These calculations can be directly compared with the RMFT results from section 6.2.

To calculate the QP weight within the VMC scheme, most authors use two helpful exact relations for Gutzwiller projected wave functions. First, one finds for the QP weight $\tilde{Z}_{\mathbf{k}\sigma}$ of electron-like excitations [207–211],

$$\tilde{Z}_{\mathbf{k}\sigma}^+ = \frac{1+x}{2} - \langle n_{\mathbf{k}\sigma} \rangle_{\Psi^N}, \quad (172)$$

that can be derived without any approximation and assumption. Thus, $\tilde{Z}_{\mathbf{k}\sigma}^+$ can be calculated from the momentum distribution of the ground state $|\Psi^N\rangle$ (see [207, 208]).

For the QP weight $\tilde{Z}_{\mathbf{k}\sigma}^-$, there is no exact relation corresponding to (172). However, several authors showed [210–212] that $\tilde{Z}_{\mathbf{k}\sigma}^+$ and $\tilde{Z}_{\mathbf{k}\sigma}^-$ combined satisfy the exact relation,

$$\tilde{Z}_{-\mathbf{k}-\sigma}^+ \cdot \tilde{Z}_{\mathbf{k}\sigma}^- = \frac{|\langle \Psi^N | c_{\mathbf{k}\sigma}^\dagger c_{-\mathbf{k}-\sigma}^\dagger | \Psi^{N-2} \rangle|^2}{\langle \Psi^N | \Psi^N \rangle \langle \Psi^{N-2} | \Psi^{N-2} \rangle} \equiv P_{\mathbf{k}}. \quad (173)$$

This relation is very useful, because the matrix elements contributing to $P_{\mathbf{k}}$ only involve ground states with different particle numbers. The quantity $P_{\mathbf{k}}$ is closely related to the off-diagonal long-range order in the pairing correlation and can be calculated in a straightforward way by VMC techniques (see, e.g., [210]). Equation (173) was also confirmed numerically [212]. However, we note that (172) and (173) are only valid for the projected wave functions $P_G|\Psi\rangle$, and cannot be used for the re-transformed wave function $e^{-iS}P_G|\Psi\rangle$, because the canonical transformation e^{-iS} does not commute with the electron and the projection operators.

7.1.1. Momentum dependence of the QP weight. VMC results for the QP weights $\tilde{Z}_{\mathbf{k}}^+$ (adding an electron) and $\tilde{Z}_{\mathbf{k}}^-$ (removing an electron), together with the total weight, $\tilde{Z}_{\mathbf{k}}^{\text{tot}} = \tilde{Z}_{\mathbf{k}}^+ + \tilde{Z}_{\mathbf{k}}^-$, are summarized in figure 52. These calculations show that $\tilde{Z}_{\mathbf{k}}^{\text{tot}}$ is continuous over the whole Brillouin zone, thus supporting the idea that $Z_{\mathbf{k}}^+ = Z_{\mathbf{k}}^-$ at the (underlying) FS [209]. However, away from the FS, figure 52 also exhibits some deviations from the simple RMFT calculations ($\tilde{Z}_{\mathbf{k}}^+ = g_t u_{\mathbf{k}}^2$ and $\tilde{Z}_{\mathbf{k}}^- = g_t v_{\mathbf{k}}^2$ with $g_t = 2x/(1+x)$). For instance, inside the Brillouin zone and along the nodal direction, RMFT gives a constant QP weight $\tilde{Z}_{\mathbf{k}}^-$ (because $\langle n_{\mathbf{k}\sigma} \rangle = v_{\mathbf{k}}^2$ is constant along the nodal direction in the t - J model, see figure 53) whereas the VMC calculations (triangles in figure 52(c); see also [211]) clearly show a non-constant behaviour.

In the absence of a superconducting gap the QP weight at the FS is determined by the jump in the moment distribution $\langle n_{\mathbf{k}\sigma} \rangle$, as discussed in section 5.3.2. Furthermore, $\tilde{Z}_{\mathbf{k}}^+$ is generally related by means of equation (172) to $\langle n_{\mathbf{k}\sigma} \rangle$ for the t - J model. Owing to this relation between $\langle n_{\mathbf{k}\sigma} \rangle$ and $\tilde{Z}_{\mathbf{k}}^+$, we re-consider the moment dependence of $\langle n_{\mathbf{k}\sigma} \rangle$ in the VMC and the RMFT calculations. In figure 53 we show RMFT as well as VMC results for the moment dependence of $\langle n_{\mathbf{k}\sigma} \rangle$ along the nodal direction determined within the Hubbard and the t - J model, respectively. We note that expectation values for the Hubbard model are obtained by applying a re-transformed wave function $e^{-iS}|\Psi\rangle$, which can be evaluated in order $\mathcal{O}(t/U)$; see (110b) in section 4.3. In contrast, the re-transformation e^{-iS} is neglected for the calculation of observables in the t - J model. figure 53(a) shows that, except for the jump at the Fermi point \mathbf{k}_F , the RMFT gives a constant $\langle n_{\mathbf{k}\sigma} \rangle$ along the nodal direction for the t - J model. However, VMC calculations at the same doping level ($x=0.05$) and for the same model parameters exhibit a non-monotonic behaviour near the Fermi point, see the white squares in figure 53(b). This effect comes from the correlated hopping nature of the electron in the projected Hilbert space and is not obtained within RMFT. This result also explains the origin of the discrepancies between the RMFT and the VMC methods in determining the QP weight and reveals some limitations of the RMFT in calculating momentum-dependent quantities. However, including the re-transformation of the wave function for the Hubbard model removes the non-monotonic behaviour of $\langle n_{\mathbf{k}\sigma} \rangle$ in the VMC data; see

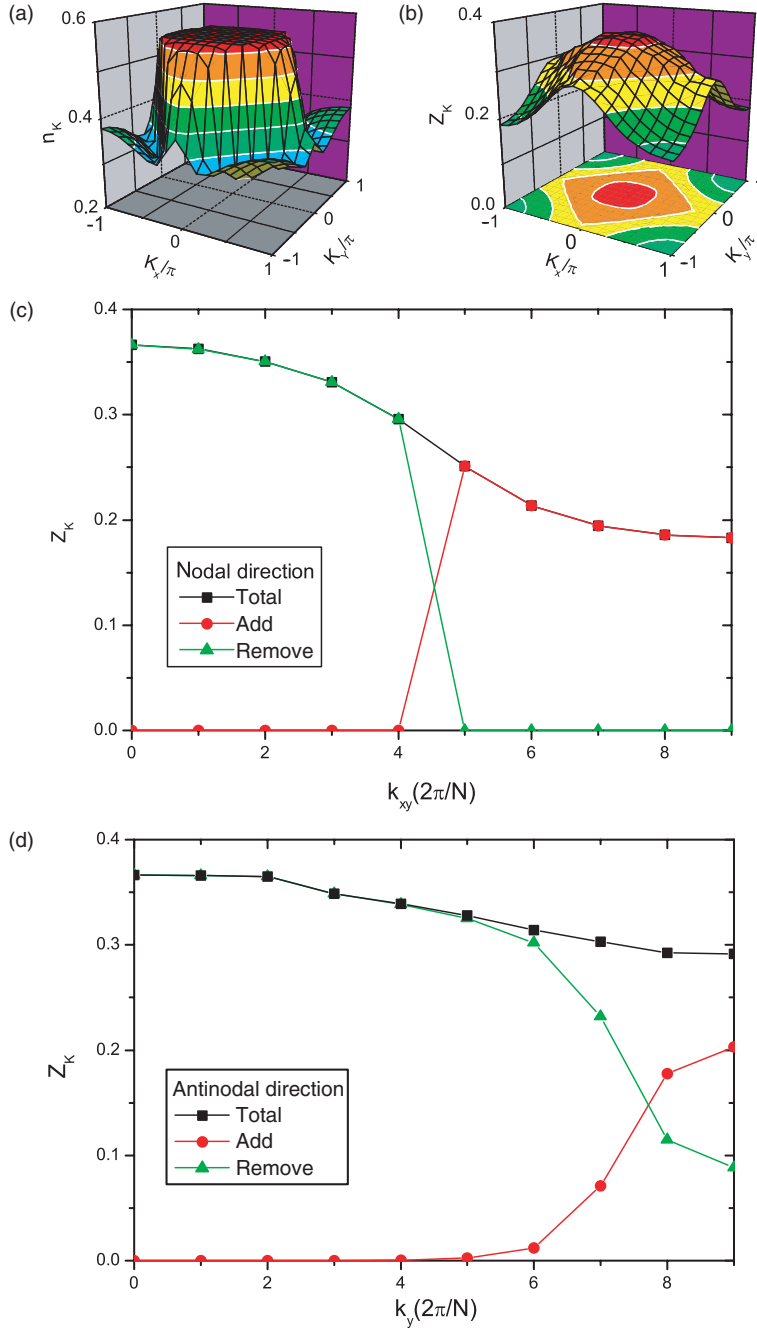


Figure 52. VMC result for Gutzwiller projected d -wave BCS state on a 18×18 lattice with 42 holes ($x \simeq 0.13$) and $\Delta/t = 0.1$. (a) Momentum distribution function $\langle n_{\mathbf{k}} \rangle$. (b) Total QP weight $\tilde{Z}_{\mathbf{k}}^{\text{tot}}$. (c) QP weight in the $(0,0) - (\pi,\pi)$ direction. (d) QP weight in the $(0,0) - (0,\pi)$ direction (total $\tilde{Z}_{\mathbf{k}}^{\text{tot}}$, add $\tilde{Z}_{\mathbf{k}}^+$, remove $\tilde{Z}_{\mathbf{k}}^-$). Results correspond to the t - J model since the re-transformation of the wave function was neglected. Reprinted with permission from [209] © 2007 IOP.

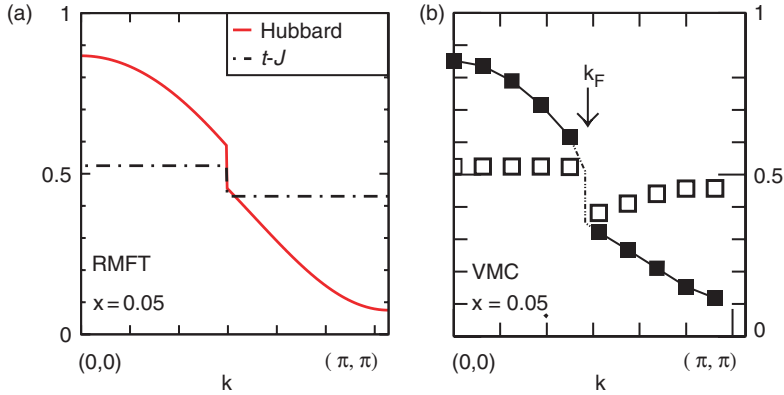


Figure 53. The momentum distribution $\langle n_{\mathbf{k}} \rangle$ along the nodal direction $\mathbf{k} = (k, k)$ for the Hubbard (black squares in (b)) and the t - J model (white squares in (b)) from (a) RMFT and (b) VMC calculations, respectively. The calculations are based on the full t - J Hamiltonian (6) with $t' = -t/4$ and $U = 12t$ at a doping level $x = 0.05$. Expectation values for the Hubbard model are evaluated within a re-transformed wave function, see (110b), whereas these corrections are neglected in the t - J model. The RMFT calculations are based on the results from sections 6.2 and 6.3; the VMC data are taken from [117].

figure 53(b). Thus, RMFT and VMC are in better qualitative agreement when $\langle n_{\mathbf{k}\sigma} \rangle$ is calculated within the Hubbard model; compare the solid curve in figure 53(a) with the black squares in figure 53(b).

7.1.2. Doping dependence of the mean QP weight. Some discrepancies between VMC and RMFT in the doping dependence of the coherent QP weight have been discussed by Chou *et al.* [210]. They calculated the average coherent QP weight for removing an electron,

$$\tilde{Z}_{\text{ave}}^- \equiv \frac{1}{L} \sum_{\mathbf{k}} \tilde{Z}_{\mathbf{k}\sigma}^-, \quad (174)$$

by the VMC scheme and compare it with the RMFT results. As shown in figure 54, VMC calculations give a significantly larger coherent QP weight than RMFT at the hole side, which is directly related to a reduction of the (average) incoherent background $n_{\text{ave}}^{\text{inc}}$ by the same amount.

On the other hand the average QP weight for adding an electron,

$$\tilde{Z}_{\text{ave}}^+ \equiv \frac{1}{L} \sum_{\mathbf{k}} \tilde{Z}_{\mathbf{k}\sigma}^+ = \frac{1+x}{2} - \frac{1}{L} \sum_{\mathbf{k}} \langle n_{\mathbf{k}\sigma} \rangle_{\Psi} = \frac{1+x}{2} - \frac{1-x}{2} = x, \quad (175)$$

is exactly the same in the RMFT and the VMC scheme, where we used (172) in (175). Thus, it was argued [210], that the increased coherent weight at the hole side seen in the VMC calculations, can explain the particle-hole asymmetry in the tunnelling experiments. However, considering the large asymmetry in the experiments and the predictions from sum rules, it is likely that, at least at higher energies, a considerable part of the asymmetry is caused by the incoherent background.

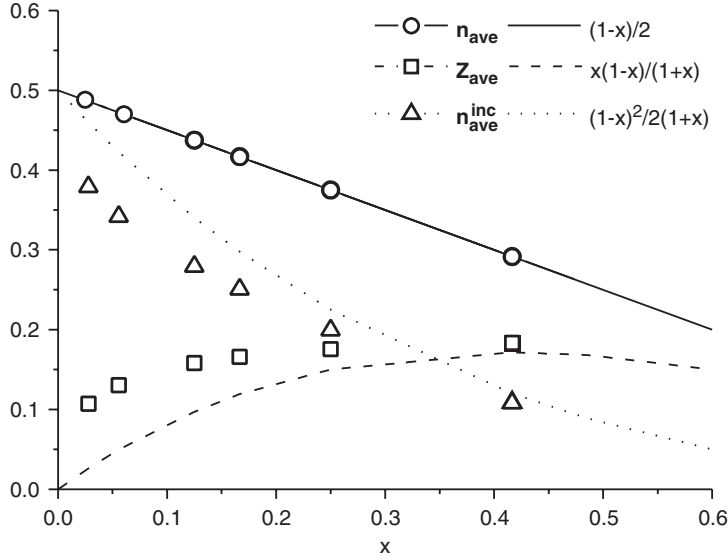


Figure 54. The doping dependence of average QP weights Z_{ave}^- for removing an electron in a d -wave state obtained by VMC calculations (12×12 lattice, $t' = 0$) and by RMFT, respectively. The results are for the t - J model (no re-transformation of the wave function). The squares (triangles) are the VMC results for Z_{ave}^- ($n_{\text{ave}}^{\text{inc}} = n_{\text{ave}} - Z_{\text{ave}}^-$) with $n_{\text{ave}} = 1/L \sum_{\mathbf{k}} \langle n_{\mathbf{k}\sigma} \rangle_{\Psi} = (1-x)/2$. The dashed and dotted curves without data points represent results by RMFT. Reprinted with permission from [210] © 2006 by the American Physical Society.

7.2. VMC calculations for the QP energy

In the previous section, we discussed how the spectral weight of Gutzwiller–Bogoliubov QP excitations can be determined directly using VMC and how such results compare with RMFT. Now we turn to the excitation energies, $E_{\mathbf{k}}$, of the QP. Here, again, RMFT results can be checked by calculating the energy corresponding to the excited state $|\Psi_{\mathbf{k},\sigma}^{N\pm 1}\rangle$ directly, equations (138) and (139), within the t - J model. Subtracting the ground state energy, we obtain the excitation energy,

$$E = \langle H_{t-J} \rangle_{\Psi_{\mathbf{k},\sigma}^{N\pm 1}} - \langle H_{t-J} \rangle_{\Psi^N}. \quad (176)$$

We discuss now the VMC calculations of Yunoki *et al.* [146], who also included a Jastrow factors into the wave functions to improve the ground state energy. Figure 55 illustrates a typical dispersion along the nodal direction obtained by determining $E_{\mathbf{k}} = |E|$ for every \mathbf{k} -point separately. As shown in the figure, a tight-binding dispersion fits well to the numerical data, and it is possible to extract interesting quantities like the nodal Fermi velocity v_F or the nodal Fermi point $|\mathbf{k}_F|$.

By repeating the calculation from figure 55 for various electron densities, one can determine the doping dependence of v_F and $|\mathbf{k}_F|$. Figure 56(a) illustrates that the Fermi velocity only slightly decreases when approaching half-filling as already seen from RMFT (see [7] and section 4.3). The results of Yunoki *et al.* also agree with previous VMC calculations utilizing the moments of the spectral function (see [21])

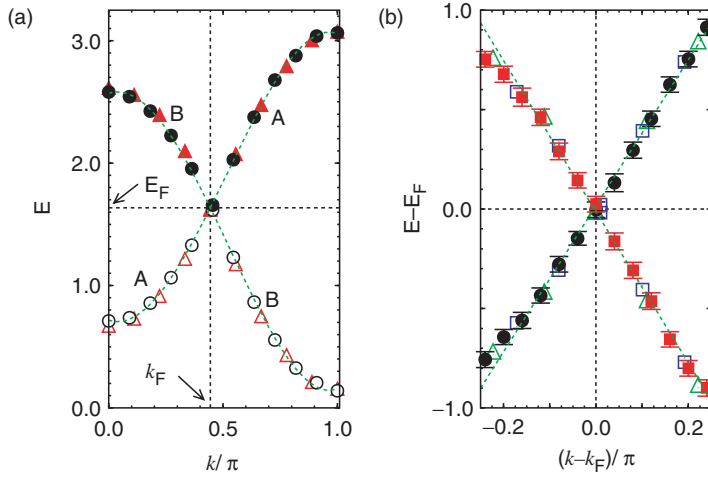


Figure 55. Dispersion E in the nodal direction for the 2D t - J model with $J/t=0.3$ and $t'/t=-0.2$ at $x=0.099$. (a) Full dispersion for $L=162$ (triangles) and 242 (circles). The electron removal (addition) spectrum is denoted by open (full) symbols. The dashed curves are tight binding fits. (b) Same as (a) but focusing on the excitations near E_F . In addition to the data for $L=162$ (open triangles) and 242 (open squares), results for $L=1250$ (full squares and circles) are also plotted. From [146].

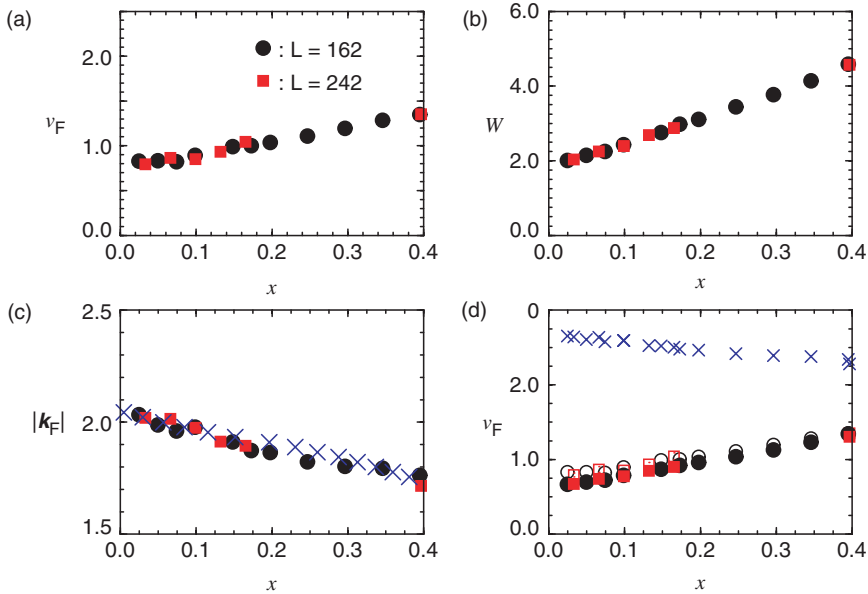


Figure 56. (a) Nodal Fermi velocity v_F , (b) bandwidth W , (c) nodal Fermi momentum $|k_F|$ and (d) unrenormalized Fermi velocity v_F^0 (crosses) compared with v_F for the 2D t - J model with $J/t=0.3$ and $t'/t=-0.2$ at different x . From [146].

and section 5.3), as well as with ARPES experiments [39, 156–159]. In figure 56(c), we see the doping dependence of the nodal Fermi point $|\mathbf{k}_F|$, which matches experimental and RMFT predictions. The renormalized band width W is given in figure 56(b); it is tightly related to v_F . Figure 56(d) illustrates a comparison between the Fermi velocity v_F and the unrenormalized velocity v_F^0 , revealing the strong renormalization effects due to the Gutzwiller projection. However, it is important to note that, in contrast to the QP weight \tilde{Z}_k , the Fermi velocity does not vanish in the half-filled limit

While Yunoki *et al.* [146] only considered the nodal dispersion, Yunoki recently extended these VMC calculations to the whole Brillouin zone [212]. His results agree quite well with the RMFT dispersion, giving further support to the Gutzwiller–Bogoliubov QP picture. To conclude this section, VMC calculations for the spectral weight and the QP excitations are in good qualitative agreement with RMFT. This is important because it shows that the simple analytical approach of RMFT together with the GA can be used reliably. Two key features emerge consistently from these two approaches: a finite and constant Fermi velocity contrasting with a vanishing QP weight in the half-filled limit.

8. Summary and outlook

In this review, we have attempted to summarize the basic idea of using Gutzwiller projected wave functions in the description of high-temperature superconductivity. Projected wave functions provide a straightforward implementation of the RVB picture wherein superexchange leads to pair correlations and doping the Mott insulator leads to a superconducting ground state.

Projected wave functions can be studied both analytically and numerically. A superconducting state with d -wave symmetry arises as the best variational wave function within the Gutzwiller–RVB theory. Incorporation of antiferromagnetic order and next-nearest-neighbour hopping then allows for a quantitative description of the cuprate phase diagram within the t – J and the Hubbard model. Sophisticated VMC calculations give detailed information about the size of the antiferromagnetic region and the stability against phase separation. These ground state properties seen in the VMC technique were recently confirmed by various quantum cluster methods, lending further support to the Gutzwiller–RVB picture.

In addition to the VMC technique, the effect of projection can be treated by Gutzwiller approximation, which then allows for a formulation of a RMFT. The RMFT results agree in general with VMC calculations and provide systematic analytic expressions for doping-dependent features.

Within the Gutzwiller–RVB picture, HTSCs are viewed as doped Mott insulators, i.e. restriction to singly occupied orbitals owing to strong correlation effects. This causes a significant decrease in the mobility of electrons (holes) near half-filling as correctly described within above microscopic calculations. The resulting renormalization of the kinetic energy explains the decrease of the superconducting order parameter, of the superfluid density and of the Drude weight when approaching half-filling. RMFT and VMC calculations also explain the large superconducting gap and the small QP weight in the underdoped cuprates. Further, the modelling of

charge ordered states, impurity sites or vortex cores qualitative agrees with experiments.

While the QP weight Z vanishes in the half-filled limit, the nodal Fermi velocity v_F stays finite. RMFT and VMC calculations explain this interesting experimental observation by the effect of the superexchange interaction on the dispersion. However, in the half-filled limit, such a behaviour ($Z \rightarrow 0$ and $v_F = \text{constand}$) immediately results in a divergence of the ω - as well as of the \mathbf{k} -dependence of the self-energy. The consequences of these divergences for any Fermi liquid description at finite doping are not fully understood. In a recent paper, Anderson [243] suggested that projected wave functions contain the essential physics to explain the non-Fermi liquid behaviour of the normal state in the cuprate superconductors, i.e. the region in the cuprate phase diagram above the pseudogap temperature scale. One reason why there has not been much progress on this issue is that we need a scheme to calculate the single particle Green's function directly in a Gutzwiller projected state. The standard technique of introducing a complete set of orthogonal excitations works as long as we only consider the contribution of the 'projected quasiparticle (hole)'. However, as we discussed earlier, the total spectral weight of a photohole (say) is not exhausted by the projected quasihole excitation. The effect can be understood most transparently as the non-commutativity of a photohole state $c_{i\sigma}P_G|\Psi_0\rangle$ and projected excitations of the form $P_Gc_{i\sigma}|\Psi_0\rangle$. It follows that a photohole is a mixture of a projected single hole excitation and a multiparticle excitation which signifies the backflow of, say, \downarrow spins accompanying a propagating \uparrow spin hole. A consistent scheme to treat this effect has not yet been devised.

Another important open question is the role played by phase fluctuations in Gutzwiller projected BCS wave functions. It was noted in the early papers of Anderson and collaborators [95] that phase fluctuations are expected to play an important role as one approaches the Mott insulator in the phase diagram. The recent experiments of Ong and collaborators [26, 27] point to the existence of a vortex liquid phase above T_c in the underdoped superconductors. A description of this phase within the Gutzwiller–RVB theory has not yet been formulated. It should be pointed out that a large corpus of literature exists on fluctuating d -wave superconductors, but to the best of our knowledge, no one has attempted to derive an effective 'phase-only' model from a microscopic Hamiltonian for Mott–Hubbard superconductors. Drzazga *et al.* addressed this issue, many years ago, using a high-temperature expansion [244]. Using standard functional integral techniques, these authors performed a Ginzburg–Landau expansion for the free energy functional of an RVB state [130]. They found that singlet pairing sets in at temperature scales higher than the (mean-field) transition temperature T_c . As the hole concentration goes to zero, the local $U(1)$ gauge symmetry in the theory leads to phase fluctuations that destroy off-diagonal long-range order. However, their calculations show that an extended s -wave state is favoured, a result that is inconsistent with the Gutzwiller–RVB theory described in this article. It would be very interesting to revisit this problem and attempt to derive a Ginzburg–Landau expansion of the d -wave Gutzwiller–RVB state. Such a step is necessary to extend the Gutzwiller–RVB framework to the description of phase degrees of freedom, and the effect of the latter in destroying superconducting correlations, both as a function of temperature and doping.

A related issue is the understanding of the pseudogap state within the RVB theory. The view we advocated was that local singlet pairing exists at temperature scales $T < T^*$. Much support for this idea comes from the experimental observation that the BCS ratio, $\Delta/(2k_B T^*)$, is constant and in agreement with mean-field theory for all doping levels, when we use the onset temperature of the pseudogap T^* instead of T_c . While this is certainly suggestive, there is no direct way of proving this within the theory, again because we do not yet have a method to describe finite-temperature effects within the Gutzwiller framework. Extending the Gutzwiller–RVB theory to the description of finite-temperature phases is an important step that needs to be taken to complete our understanding of the pseudogap state. In this context, we note that a finite-temperature scheme for Gutzwiller projected Fermi liquids was developed by Seiler *et al.* [121] to study ^3He . Whether a similar scheme can be developed to study projected d -wave superconductors at finite temperatures remains to be seen. A related issue is the investigation of finite frequency excitations in the Gutzwiller–RVB scheme. In particular, it will be very useful to study the collective excitations of the Gutzwiller superconductor along the lines of Anderson’s original work on equations of motion for collective modes in a BCS superconductor [245].

Acknowledgements

The authors thank P. W. Anderson for several discussions and comments on this manuscript. VNM thanks P. W. Anderson, G. Baskaran, G. Levine, N. P. Ong, T. V. Ramakrishnan, D. Schmeltzer and Z.-Y. Weng for several discussions over the years.

References

- [1] J.G. Bednorz and K.A. Müller, *Z. Phys.* **64** 189 (1986).
- [2] M.R. Norman and C. Pepin, *Rep. Prog. Phys.* **66** 1547 (2003).
- [3] C.C. Tsuei and J.R. Kirtley, *Rev. Mod. Phys.* **72** 969 (2000).
- [4] D.J. Scalapino, *Handbook of High Temperature Superconductivity*, edited by J.R. Schrieffer (Springer, New York, 2006).
- [5] B. Edegger, N. Fukushima, C. Gros and V.N. Muthukumar, *Phys. Rev. B* **72** 134504 (2005).
- [6] N. Fukushima, B. Edegger, V.N. Muthukumar and C. Gros, *Phys. Rev. B* **72** 144505 (2005).
- [7] B. Edegger, V.N. Muthukumar, C. Gros and P.W. Anderson, *Phys. Rev. Lett.* **96** 207002 (2006).
- [8] B. Edegger, V.N. Muthukumar and C. Gros, *Phys. Rev. B* **74** 165109 (2006).
- [9] C. Gros, B. Edegger, V.N. Muthukumar and P.W. Anderson, *Proc. Natl. Acad. Sci. USA* **103** 14298 (2006).
- [10] B. Edegger, V.N. Muthukumar and C. Gros, *Physica C*, **460–462** 1151 (2007).
- [11] L. Pauling, *Phys. Rev.* **54** 899 (1938).
- [12] L. Pauling, *Nature* **161** 1019 (1948).
- [13] P.W. Anderson, *Mat. Res. Bull.* **8** 153 (1973).
- [14] P. Fazekas and P.W. Anderson, *Philos. Mag.* **30** 432 (1974).
- [15] P.W. Anderson, *Science* **235** 1196 (1987).
- [16] C. Gros, R. Joynt and T.M. Rice, *Z. Phys.* **68** 425 (1987).
- [17] C. Gros, *Phys. Rev. B* **38** 931 (1988).

- [18] G. Kotliar and J. Liu, Phys. Rev. B **38** 5142 (1988).
- [19] P.A. Lee, N. Nagaosa and X.-G. Wen, Rev. Mod. Phys. **78** 17 (2006).
- [20] F.C. Zhang, C. Gros, T.M. Rice and H. Shiba, Supercond. Sci. Tech. **1** 36 (1988).
- [21] A. Paramekanti, M. Randeria and N. Trivedi, Phys. Rev. Lett. **87** 217002 (2001).
- [22] M.R. Norman, D.P. Pines and C. Kallin, Adv. Phys. **54** 715 (2005).
- [23] A. Damascelli, Z. Hussain and Z.-X. Shen, Rev. Mod. Phys. **75** 473 (2003).
- [24] J.C. Campuzano, M.R. Norman and M. Randeria, *Physics of Conventional and Unconventional Superconductors* (Springer, Berlin, 2004).
- [25] F.C. Zhang and T.M. Rice, Phys. Rev. B **37** 3759 (1988).
- [26] N.P. Ong, Y. Wang, S. Ono, Y. Ando and S. Uchida, Ann. Phys. **13** 9 (2004).
- [27] Y. Wang, S. Ono, Y. Onose, G. Gu, Y. Ando, Y. Tokura, S. Uchida and N.P. Ong, Science **299** 86 (2003).
- [28] S.A. Kivelson, E. Fradkin, V. Oganesyan, I.P. Bindloss, J.M. Tranquada, A. Kapitulnik and C. Howald, Rev. Mod. Phys. **75** 1201 (2003).
- [29] J.M. Tranquada, *Treatise of High Temperature Superconductivity*, edited by J.R. Schrieffer, Preprint (2005), cond-mat/0512115.
- [30] C.M. Varma, P.B. Littlewood, S. Schmitt-Rink, E. Abrahams and A.E. Ruckenstein, Phys. Rev. Lett. **63** 1996 (1989).
- [31] E. Dagotto, Science **309** 257 (2005).
- [32] S. Doniach and E. Sondheimer, *Green's Functions for Solid State Physicists* (Benjamin, Reading, MA, 1982).
- [33] J. Mesot, M.R. Norman, H. Ding, M. Randeria, J.C. Campuzano, A. Paramekanti, H.M. Fretwell, A. Kaminski, T. Takeuchi, T. Yokoya, T. Sato, T. Takahashi, T. Mochiku and K. Kadowaki, Phys. Rev. Lett. **83** 840 (1999).
- [34] J.C. Campuzano, H. Ding, M.R. Norman, H.M. Fretwell, M. Randeria, A. Kaminski, J. Mesot, T. Takeuchi, T. Sato, T. Yokoya, T. Takahashi, T. Mochiku, K. Kadowaki, P. Guptasarma, D.G. Hinks, Z. Konstantinovic, Z.Z. Li and H. Raffy, Phys. Rev. Lett. **83** 3709 (1999).
- [35] H. Won and K. Maki, Phys. Rev. B **49** 1397 (1994).
- [36] M. Kugler, O. Fischer, Ch. Renner, S. Ono and Y. Ando, Phys. Rev. Lett. **86** 4911 (2001).
- [37] D.L. Feng, D.H. Lu, K.M. Shen, C. Kim, H. Eisaki, A. Damascelli, R. Yoshizaki, J.-I. Shimoyama, K. Kishio, G.D. Gu, S. Oh, A. Andrus, J. O'Donnell, J.N. Eckstein and Z.-X. Shen, Science **289** 277 (2000).
- [38] H. Ding, J.R. Engelbrecht, Z. Wang, J.C. Campuzano, S.-C. Wang, H.-B. Yang, R. Rogan, T. Takahashi, K. Kadowaki and D.G. Hinks, Phys. Rev. Lett. **87** 227001 (2001).
- [39] X.J. Zhou, T. Yoshida, A. Lanzara, P.V. Bogdanov, S.A. Kellar, K.M. Shen, W.L. Yang, F. Ronning, T. Sasagawa, T. Kakeshita, T. Noda, H. Eisaki, S. Uchida, C.T. Lin, F. Zhou, J.W. Xiong, W.X. Ti, Z.X. Zhao, A. Fujimori, Z. Hussain and Z.-X. Shen, Nature **423** 398 (2003).
- [40] M. Chiao, R.W. Hill, C. Lupien, L. Taillefer, P. Lambert, R. Gagnon and P. Fournier, Phys. Rev. B **62** 3554 (2000).
- [41] M.R. Norman, H. Ding, M. Randeria, J.C. Campuzano, T. Yokoya, T. Takeuchi, T. Takahashi, T. Mochiku, K. Kadowaki, P. Guptasarma and D.G. Hinks, Nature **392** 157 (1998).
- [42] A.G. Loeser, Z.-X. Shen, D.S. Dessau, D.S. Marshall, C.H. Park, P. Fournier and A. Kapitulnik, Science **273** 325 (1996).
- [43] D.S. Marshall, D.S. Dessau, A.G. Loeser, C.-H. Park, A.Y. Matsuura, J.N. Eckstein, I. Bozovic, P. Fournier, A. Kapitulnik, W.E. Spicer and Z.-X. Shen, Phys. Rev. Lett. **76**, 4841 (1996).
- [44] H. Ding, T. Yokoya, J.C. Campuzano, T. Takahashi, M. Randeria, M.R. Norman, T. Mochiku, K. Kadowaki and J. Giapintzakis, Nature **382** 51 (1996).
- [45] A. Kanigel, M.R. Norman, M. Randeria, U. Chatterjee, S. Suoma, A. Kaminski, H.M. Fretwell, S. Rosenkranz, M. Shi, T. Sato, T. Takahashi, Z.Z. Li, H. Raffy, K. Kadowaki, D. Hinks, L. Ozyuzer and J.C. Campuzano, Nature Physics **2** 447 (2006).
- [46] E.W. Hudson, S.H. Pan, A.K. Gupta, K.-W. Ng and J.C. Davis, Science **285** 88 (1999).

- [47] A. Yazdani, C.M. Howald, C.P. Lutz, A. Kapitulnik and D.M. Eigler, *Phys. Rev. Lett.* **83** 176 (1999).
- [48] S.H. Pan, E.W. Hudson, K.M. Lang, H. Eisaki, S. Uchida and J.C. Davis, *Nature* **403** 746 (2003).
- [49] I. Maggio-Aprile, Ch. Renner, A. Erb, E. Walker and Ø. Fischer, *Phys. Rev. Lett.* **75** 2754 (1995).
- [50] Ch. Renner, B. Revaz, K. Kadowaki, I. Maggio-Aprile and Ø. Fischer, *Phys. Rev. Lett.* **80** 3606 (1998).
- [51] S.H. Pan, E.W. Hudson, A.K. Gupta, K.-W. Ng, H. Eisaki, S. Uchida and J.C. Davis, *Phys. Rev. Lett.* **85** 1536 (2000).
- [52] M. Vershinin, S. Misra, S. Ono, Y. Abe, Y. Ando and A. Yazdani, *Science* **303** 1995 (2004).
- [53] T. Hanaguri, C. Lupien, Y. Kohsaka, D.-H. Lee, M. Azuma, M. Takano, H. Takagi and J.C. Davis, *Nature* **430** 1001 (2004).
- [54] K. McElroy, D.-H. Lee, J.E. Hoffman, K.M. Lang, J. Lee, E.W. Hudson, H. Eisaki, S. Uchida and J.C. Davis, *Phys. Rev. Lett.* **94** 197005 (2005).
- [55] V.J. Emery, *Phys. Rev. Lett.* **58** 3759 (1987).
- [56] C.M. Varma, S. Schmitt-Rink and E. Abrahams, *Solid State Commun.* **62** 681 (1987).
- [57] E. Dagotto, *Rev. Mod. Phys.* **66** 763 (1994).
- [58] T. Moriya and K. Ueda, *Adv. Phys.* **49** 555 (2000).
- [59] Y. Yanase, T. Jujo, T. Nomura, H. Ikeda, T. Hotta and K. Yamada, *Phys. Rep.* **387** 1 (2003).
- [60] A.V. Chubukov, D. Pines and J. Schmalian, *The Physics of Conventional and Unconventional Superconductors*, edited by K.H. Bennemann and J.B. Ketterson (Springer, New York, 2002).
- [61] S.A. Kivelson and E. Fradkin, *Treatise of High Temperature Superconductivity*, edited by J.R. Schrieffer, Preprint (2005), cond-mat/0507459.
- [62] E.W. Carlson, V.J. Emery, S.A. Kivelson and D. Orgad, *The Physics of Conventional and Unconventional Superconductors*, edited by K.H. Bennemann and J.B. Ketterson (Springer, New York, 2002).
- [63] E. Demler, W. Hanke and S.-C. Zhang, *Rev. Mod. Phys.* **76** 909 (2004).
- [64] T. Maier, M. Jarrell, T. Pruschke and M.H. Hettler, *Rev. Mod. Phys.* **77** 1027 (2005).
- [65] C.M. Varma, *Phys. Rev. B* **73** 155113 (2006).
- [66] S. Chakravarty, R.B. Laughlin, D.K. Morr and C. Nayak, *Phys. Rev. B* **63** 094503 (2001).
- [67] M. Randeria, *Proceedings of the International School of Physics Enrico Fermi Course CXXXVI on High Temperature Superconductors*, edited by G. Iadonisi, J.R. Schrieffer and M.L. Chialfalo (IOS Press, Amsterdam, 1998), p. 53.
- [68] Q. Chen, J. Stajic, S. Tan and K. Levin, *Phys. Rep.* **412** 1 (2005).
- [69] Y. Endoh, K. Yamada, R.J. Birgeneau, D.R. Gabbe, H.P. Jenssen, M.A. Kastner, C.J. Peters, P.J. Picone, T.R. Thurston, J.M. Tranquada, G. Shirane, Y. Hidaka, M. Oda, Y. Enomoto, M. Suzuki and T. Murakami, *Phys. Rev. B* **37** 7443 (1988).
- [70] S. Chakravarty, B.I. Halperin and D.R. Nelson, *Phys. Rev. B* **39** 2344 (1989).
- [71] S. Liang, B. Doucot and P.W. Anderson, *Phys. Rev. Lett.* **61** 365 (1988).
- [72] C.L. Kane, P.A. Lee and N. Read, *Phys. Rev. B* **39** 6880 (1989).
- [73] C. Gros and M.D. Johnson, *Phys. Rev. B* **40** 9423 (1989).
- [74] P.W. Anderson, *Physica B* **318** 28 (2002).
- [75] T.K. Lee and S. Feng, *Phys. Rev. B* **38** 11809 (1988).
- [76] T.C. Hsu, *Phys. Rev. B* **41** 11379 (1990).
- [77] C.-M. Ho, V.N. Muthukumar, M. Ogata and P.W. Anderson, *Phys. Rev. Lett.* **86** 1626 (2001).
- [78] Y. Shimizu, K. Miyagawa, K. Kanoda, M. Maesato and G. Saito, *Phys. Rev. Lett.* **91** 107001 (2003).
- [79] O. Motrunich, *Phys. Rev. B* **72** 045105 (2005).
- [80] Sung-Sik Lee and Patrick A. Lee, *Phys. Rev. Lett.* **95** 036403 (2005).
- [81] M.E. Zhitomirsky and K. Ueda, *Phys. Rev. B* **54** 9007 (1996).
- [82] L. Capriotti and S. Sorella, *Phys. Rev. Lett.* **84** 3173 (2000).

- [83] K. Takano, Y. Kito, Y. Ono and K. Sano, Phys. Rev. Lett. **91** 197202 (2003).
- [84] L. Capriotti, F. Becca, A. Parola and S. Sorella, Phys. Rev. Lett. **87** 097201 (2001).
- [85] M. Mambrini, A. Laeuchli, D. Poilblanc and F. Mila, Phys. Rev. B **74** 144422 (2006).
- [86] C. Weber, A. Laeuchli, F. Mila and T. Giamarchi, Phys. Rev. B **73** 014519 (2006).
- [87] T. Valla, A.V. Fedorov, J. Lee, J.C. Davis and G.D. Gu, Science **314** 1914 (2006).
- [88] G. Baskaran, Phys. Rev. Lett. **91** 097003 (2003).
- [89] B. Kumar and B.S. Shastry, Phys. Rev. B **68** 104508 (2003).
- [90] M. Ogata, J. Phys. Soc. Jpn **72** 1839 (2003).
- [91] M. Imada, A. Fujimori and Y. Tokura, Rev. Mod. Phys. **70** 1039 (1998).
- [92] B.J. Powell and R.H. McKenzie, Phys. Rev. Lett. **94** 047004 (2005).
- [93] J.Y. Gan, Y. Chen, Z.B. Su and F.C. Zhang, Phys. Rev. Lett. **94** 067005 (2005).
- [94] J. Liu, J. Schmalian and N. Trivedi, Phys. Rev. Lett. **94** 127003 (2005).
- [95] G. Baskaran, Z. Zou and P.W. Anderson, Solid State Commun. **63** 973 (1987).
- [96] Y. Suzumura, Y. Hasegawa and H. Fukuyama, J. Phys. Soc. Jpn **57** 2768 (1988).
- [97] H. Yokoyama and H. Shiba, J. Phys. Soc. Jpn **57** 2482 (1988).
- [98] P.W. Anderson, Preprint (2004), cond-mat/0406038.
- [99] H.-X. Huang, Y.-Q. Li and F.-C. Zhang, Phys. Rev. B **71** 184514 (2005).
- [100] D. Poilblanc, Phys. Rev. B **72** 060508(R) (2005).
- [101] C. Li, S. Zhou and Z. Wang, Phys. Rev. B **73** 060501(R) (2006).
- [102] A. Himeda and M. Ogata, Phys. Rev. B **60** R9935 (1999).
- [103] G.J. Chen, R. Joynt, F.C. Zhang and G. Gros, Phys. Rev. B **42** 2662 (1990).
- [104] T. Giamarchi and C. Lhuillier, **43** 12943 (1991).
- [105] D.A. Ivanov, Phys. Rev. B **70** 104503 (2004).
- [106] C.T. Shih, Y.C. Chen, C.P. Chou and T.K. Lee, Phys. Rev. B **70** 220502(R) (2004).
- [107] M. Ogata and A. Himeda, J. Phys. Soc. Jpn **72** 374 (2003).
- [108] H. Tsuchiura, Y. Tanaka, M. Ogata and S. Kashiwaya, J. Phys. Soc. Jpn **68** 2510 (1999).
- [109] H. Tsuchiura, Y. Tanaka, M. Ogata and S. Kashiwaya, Phys. Rev. Lett. **84** 3165 (2000).
- [110] H. Tsuchiura, Y. Tanaka, M. Ogata and S. Kashiwaya, Phys. Rev. B **64** 140501 (2001).
- [111] A. Himeda, M. Ogata, Y. Tanaka and S. Kashiwaya, J. Phys. Soc. Jpn **66** 3367 (1997).
- [112] H. Tsuchiura, M. Ogata, Y. Tanaka and S. Kashiwaya, Phys. Rev. B **68** 012509 (2003).
- [113] P.W. Anderson, Phys. Rev. Lett. **96** 017001 (2005).
- [114] V.J. Emery and S.A. Kivelson, Nature **374** 434 (1995).
- [115] D.-H. Lee, Phys. Rev. Lett. **84** 2694 (2000).
- [116] C. Gros, R. Joynt and T.M. Rice, Phys. Rev. B **36** 381 (1987).
- [117] A. Paramekanti, M. Randeria and N. Trivedi, Phys. Rev. B **70** 054504 (2004).
- [118] M.C. Gutzwiller, Phys. Rev. Lett. **10** 159 (1963).
- [119] W.F. Brinkman and T.M. Rice, Phys. Rev. B **2** 4302 (1970).
- [120] D. Vollhardt, Rev. Mod. Phys. **56** 99 (1984).
- [121] K. Seiler, C. Gros, T.M. Rice, K. Ueda and D. Vollhardt, J. Low. Temp. Phys. **64** 195 (1986).
- [122] T. Ogawa, K. Kanda and T. Matsubara, Prog. Theor. Phys. **53** 614 (1975).
- [123] W. Metzner and D. Vollhardt, Phys. Rev. B **37** 7382 (1988).
- [124] F. Gebhard, Phys. Rev. B **41** 9452 (1990).
- [125] J. Bünemann, F. Gebhard, K. Radnoczi and P. Fazekas, J. Phys.: Condens. Matter **17** 3807 (2005).
- [126] J. Bünemann, F. Gebhard, T. Ohm, S. Weiser and W. Weber, *Frontiers in Magnetic Materials*, edited by A. Narlikar (Springer, 2005).
- [127] S.E. Barnes, J. Phys. F **6** 1375 (1976).
- [128] P. Coleman, Phys. Rev. B **29** 3035 (1984).
- [129] G. Kotliar and A.E. Ruckenstein, Phys. Rev. Lett. **57** 1362 (1986).
- [130] G. Baskaran and P.W. Anderson, Phys. Rev. B **37** 580 (1988).
- [131] X.-G. Wen and P.A. Lee, Phys. Rev. Lett. **76** 503 (1996).
- [132] Z.Y. Weng, D.N. Sheng and C.S. Ting, Phys. Rev. B **59** 8943 (1999).
- [133] V.N. Muthukumar and Z.Y. Weng, Phys. Rev. B **65** 174511 (2002).
- [134] Z.Y. Weng and V.N. Muthukumar, Phys. Rev. B **66** 094509 (2002).
- [135] Yi Zhou, V.N. Muthukumar and Zheng-Yu Weng, Phys. Rev. B **67** 064512 (2003).

- [136] D.A. Ivanov, Phys. Rev. B **74** 024525 (2006).
- [137] M. Capello, F. Becca, M. Fabrizio, S. Sorella and E. Tosatti, Phys. Rev. Lett. **94** 026406 (2005).
- [138] T. Watanabe, H. Yokoyama, Y. Tanaka and J. Inoue, J. Phys. Soc. Jpn **75** 074707 (2006).
- [139] C.S. Hellberg and E.J. Mele, Phys. Rev. Lett. **67** 2080 (1991).
- [140] R. Valenti and C. Gros, Phys. Rev. Lett. **68** 2402 (1992).
- [141] T.K. Lee and L.N. Chang, Phys. Rev. B **42** 8720 (1990).
- [142] D.A. Ivanov and P.A. Lee, Phys. Rev. B **68** 132501 (2003).
- [143] Y. Ran, M. Hermele, P.A. Lee and X.-G. Wen, Phys. Rev. Lett. **98** 117205 (2007).
- [144] R. Jastrow, Phys. Rev. **98** 1479 (1955).
- [145] S. Sorella, G.B. Martins, F. Becca, C. Gazza, L. Capriotti, A. Parola and E. Dagotto, Phys. Rev. Lett. **88** 117002 (2002).
- [146] S. Yunoki, E. Dagotto and S. Sorella, Phys. Rev. Lett. **94** 037001 (2005).
- [147] C. Gros, Ann. Phys. **189** 53 (1989).
- [148] M. Lugas, L. Spanu, F. Becca and S. Sorella, Phys. Rev. B **74** 165122 (2006).
- [149] D. Vollhardt, P. Wölfle and P.W. Anderson, Phys. Rev. B **35** 6703 (1987).
- [150] T.M. Rice and K. Ueda, Phys. Rev. Lett. **55** 995 (1985).
- [151] C.M. Varma, W. Weber and L.J. Randall, Phys. Rev. B **33** 1015 (1986).
- [152] T.C. Hsu, Phys. Rev. B **41** 11379 (1990).
- [153] P.W. Anderson and N.P. Ong, J. Phys. Chem. Solids **67** 1 (2006).
- [154] I. Affleck, Z. Zou, T. Hsu and P.W. Anderson, Phys. Rev. B **38** 745 (1988).
- [155] P.W. Anderson, J. Phys. Chem. Solids **63** 2145 (2002).
- [156] S.V. Borisenko *et al.*, Phys. Rev. Lett. **96** 117004 (2006).
- [157] A.A. Kordyuk, S.V. Borisenko, A. Koitzsch, J. Fink, M. Knupfer, and H. Berger, Phys. Rev. B **71** 214513 (2005); A.A. Kordyuk, private communication.
- [158] P.V. Bogdanov, A. Lanzara, S.A. Kellar, X.J. Zhou, E.D. Lu, W.J. Zheng, G. Gu, J.-I. Shimoyama, K. Kishio, H. Ikeda, R. Yoshizaki, Z. Hussain and Z.X. Shen, Phys. Rev. Lett. **85** 2581 (2000).
- [159] P.D. Johnson, T. Valla, A.V. Fedorov, Z. Yusof, B.O. Wells, Q. Li, A.R. Moodenbaugh, G.D. Gu, N. Koshizuka, C. Kendziora, Sha Jian and D.G. Hinks, Phys. Rev. Lett. **87** 177007 (2001).
- [160] E. Pavarini, I. Dasgupta, T. Saha-Dasgupta, O. Jepsen and O.K. Andersen, Phys. Rev. Lett. **87** 047003 (2001).
- [161] C.T. Shih, T.K. Lee, R. Eder, C.-Y. Mou and Y.C. Chen, Phys. Rev. Lett. **92** 227002 (2004).
- [162] D. Senechal, P.L. Lavertu, M.A. Marois and A.M.S. Tremblay, Phys. Rev. Lett. **94** 156404 (2005).
- [163] M. Aichhorn and E. Arrigoni, Europhys. Lett. **71** 117 (2005).
- [164] Q.-H. Wang, Z.D. Wang, Y. Chen, and F.-C. Zhang, Phys. Rev. B **73** 092507 (2006).
- [165] B. Lake *et al.*, Science **291** 1759 (2001).
- [166] B. Lake *et al.*, Nature **415** 299 (2002).
- [167] B. Khaykovich, Y.S. Lee, R.W. Erwin, S.-H. Lee, S. Wakimoto, K.J. Thomas, M.A. Kastner and R.J. Birgeneau, Phys. Rev. B **66** 014528 (2002).
- [168] R.I. Miller, R.F. Kiefl, J.H. Brewer, J.E. Sonier, J. Chakhalian, S. Dunsiger, G.D. Morris, A.N. Price, D.A. Bonn, W.H. Hardy and R. Liang, Phys. Rev. Lett. **88** 137002 (2002).
- [169] V.F. Mitrovic, E.E. Sigmund, M. Eschrig, H.N. Bachman, W.P. Halperin, A.P. Reyes, P. Kuhns and W.G. Moulton, Nature **413** 501 (2001).
- [170] K. Kakuyanagi, K.I. Kumagai and Y. Matsuda, Phys. Rev. B **65** 060503(R) (2002).
- [171] S.-D. Liang and T.K. Lee, Phys. Rev. B **65** 214529 (2002).
- [172] Y. Tanuma, Y. Tanaka, M. Ogata and S. Kashiwaya, J. Phys. Soc. Jpn **67** 1118 (1998).
- [173] Y. Tanuma, Y. Tanaka, M. Ogata and S. Kashiwaya, Phys. Rev. B **60** 9817 (1999).
- [174] F.-C. Zhang, Phys. Rev. Lett. **90** 207002 (2003).
- [175] R.B. Laughlin, Phil. Mag. **86** 1165 (2006).
- [176] J.Y. Gan, F.C. Zhang, Z.B. Su, Phys. Rev. B **71** 014508 (2005).

- [177] T.K. Kopec, Phys. Rev. B **70** 054518 (2004).
- [178] B. Normand and A.M. Oles, Phys. Rev. B **70** 134407 (2004).
- [179] F. Yuan, Q. Yuan and C.S. Ting, Phys. Rev. B **71** 104505 (2005).
- [180] G. Seibold and J. Lorenzana, Phys. Rev. Lett. **86** 2605 (2001).
- [181] J. Lorenzana and G. Seibold, Phys. Rev. Lett. **90** 066404 (2003).
- [182] G. Seibold, F. Becca, P. Rubin and J. Lorenzana, Phys. Rev. B **69** 155113 (2004).
- [183] G. Seibold and J. Lorenzana, Phys. Rev. Lett. **94** 107006 (2005).
- [184] G. Seibold and J. Lorenzana, Phys. Rev. B **73** 144515 (2006).
- [185] G. Seibold, J. Lorenzana and M. Grilli, Phys. Rev. B **75** 100505 (2007).
- [186] P. Horsch and T.A. Kaplan, J. Phys. C **16** L1203 (1983).
- [187] D. Ceperley, G.V. Chester and M.H. Kalos, Phys. Rev. B **16** 3081 (1977).
- [188] H. Yokoyama and M. Ogata, J. Phys. Soc. Jpn **65** 3615 (1996).
- [189] N. Trivedi and D.M. Ceperly, Phys. Rev. B **41** 4552 (1990).
- [190] M.C. Buonaura and S. Sorella, Phys. Rev. B **57** 11446 (1998).
- [191] D.A. Ivanov, P.A. Lee and X.-G. Wen, Phys. Rev. Lett. **84** 3958 (2000).
- [192] A. Himeda and H. Ogata, Phys. Rev. Lett. **85** 4345 (2000).
- [193] A. Himeda, T. Kato and M. Ogata, Phys. Rev. Lett. **88** 117001 (2002).
- [194] C. Weber, D. Poilblanc, S. Capponi, F. Mila and C. Jaudet, Phys. Rev. B **74** 104506 (2006).
- [195] C.T. Shih, Y.C. Chen, H.Q. Lin and T.K. Lee, Phys. Rev. Lett. **81** 1294 (1998).
- [196] T.K. Lee, C.T. Shih, Y.C. Chen and H.Q. Lin, Phys. Rev. Lett. **89** 279702 (2002).
- [197] S. Sorella, A. Parola, F. Becca, L. Capriotti, C. Gazza, E. Dagotto and G. Martins, Phys. Rev. Lett. **89** 279703 (2002).
- [198] P.W. Anderson, P.A. Lee, M. Randeria, T.M. Rice, N. Trivedi and F.C. Zhang, J. Phys.: Condens. Matter **16** R755 (2004).
- [199] H. Yamase and H. Kohno, J. Phys. Soc. Jpn **69** 2151 (2000).
- [200] H. Yamase and H. Kohno, J. Phys. Soc. Jpn **69** 332 (2000).
- [201] C.J. Halboth and W. Metzner, Phys. Rev. Lett. **85** 5162 (2000).
- [202] D.J. Scalapino, S.R. White and S.-C. Zhang, Phys. Rev. B **47** 7995 (1993).
- [203] K.-Y. Yang *et al.*, Phys. Rev. B **73** 224513 (2006).
- [204] A. Paramekanti, N. Trivedi and M. Randeria, Phys. Rev. B **57** 11639 (1998).
- [205] Y.J. Uemura *et al.*, Phys. Rev. Lett. **62** 2317 (1989).
- [206] M. Randeria, R. Sensarma, N. Trivedi and F.-C. Zhang, Phys. Rev. Lett. **95** 137001 (2005).
- [207] S. Yunoki, Phys. Rev. B **72** 092505 (2005).
- [208] C.P. Nave, D.A. Ivanov and P.A. Lee, Phys. Rev. B **73** 104502 (2006).
- [209] H.-Y. Yang, F. Yang, Y.-J. Jiang and T. Li, J. Phys.: Condens. Matter **19** 016217 (2007).
- [210] C.-P. Chou, T.K. Lee and C.-M. Ho, Phys. Rev. B **74** 092503 (2006).
- [211] S. Bieri and D. Ivanov, Phys. Rev. B **75** 035104 (2007).
- [212] S. Yunoki, Phys. Rev. B **74** 180504(R) (2006).
- [213] A.B. Harris and R.V. Lange, Phys. Rev. **157**, 295 (1967).
- [214] M.B.J. Meinders, H. Eskes and G.A. Sawatzky, Phys. Rev. B **48** 3916 (1993).
- [215] H. Eskes and A.M. Oles, Phys. Rev. Lett. **73**, 1279 (1994).
- [216] H. Eskes, A.M. Oles, M.B.J. Meinders and W. Stephan, Phys. Rev. B **50** 17980 (1994).
- [217] D. Baeriswyl, C. Gros and T.M. Rice, Phys. Rev. B **35** 8391 (1987).
- [218] J. Hubbard, Proc. Roy. Soc. Lond. Ser. A **276** 238 (1963).
- [219] M. Randeria, A. Paramekanti and N. Trivedi, Phys. Rev. B **69** 144509 (2004).
- [220] A. Kaminski, S. Rosenkranz, H.M. Fretwell, M.R. Norman, M. Randeria, J.C. Campuzano, J.-M. Park, Z.Z. Li and H. Raffy, Phys. Rev. B **73** 174511 (2006).
- [221] T. Yoshida, X.J. Zhou, K. Tanaka, W.L. Yang, Z. Hussain, Z.-X. Shen, A. Fujimori, S. Komiya, Y. Ando, H. Eisaki, T. Kakeshita and S. Uchida, Phys. Rev. B **74** 224510 (2006).
- [222] A. Paramekanti and M. Randeria, Phys. Rev. B **66** 214517 (2002).
- [223] P.A. Lee, and X.-G. Wen, Phys. Rev. Lett. **78** 4111 (1997).
- [224] X.-G. Wen and P.A. Lee, Phys. Rev. Lett. **80** 2193 (1998).
- [225] L.B. Ioffe and A.J. Millis, J. Phys. Chem. Solids **63** 2259 (2002).

- [226] D.M. Broun, P.J. Turner, W.A. Huttema, S. Ozcan, B. Morgan, R. Liang, W.N. Hardy and D.A. Bonn, *AIP Conf. Proc.* **850** 441 (2006).
- [227] I.F. Herbut, *Phys. Rev. Lett.* **94** 237001 (2005).
- [228] R. Sensarma, M. Randeria and N. Trivedi, *Phys. Rev. Lett.* **98** 027004 (2007).
- [229] D. Pines and P. Nozières, *The Theory of Quantum Liquids* (Addison-Wesley, Reading, MA, 1966).
- [230] I. Dzyaloshinskii, *Phys. Rev. B* **68** 085113 (2003).
- [231] C. Gros, W. Wenzel, R. Valentí, G. Hülshenbeck and J. Stolze, *Europhys. Lett.* **27** 299 (1994).
- [232] T.D. Stanescu, P.W. Phillips and T.-P. Choy, *Phys. Rev. B* **75** 104503 (2007).
- [233] K.-Y. Yang, T.M. Rice and F.-C. Zhang, *Phys. Rev. B* **73** 174501 (2006).
- [234] K.M. Shen, F. Ronning, D.H. Lu, F. Baumberger, N.J.C. Ingle, W.S. Lee, W. Meevasana, Y. Kohsaka, M. Azuma, M. Takano, H. Takagi and Z.-X. Shen, *Science* **307** 901 (2005).
- [235] Y. Kohsaka, K. Iwaya, S. Satow, T. Hanaguri, M. Azuma, M. Takano and H. Takagi, *Phys. Rev. Lett.* **93** 097004 (2004).
- [236] W.O. Putikka, M.U. Luchini and R.R.P. Singh, *Phys. Rev. Lett.* **81** 2966 (1998).
- [237] T.A. Maier, T. Pruschke and M. Jarrell, *Phys. Rev. B* **66** 075102 (2002).
- [238] J.C. Campuzano, H. Ding, M.R. Norman, M. Randeira, A.F. Bellman, T. Yokoya, T. Takahashi, H. Katayama-Yoshida, T. Mochiku and K. Kadowaki, *Phys. Rev. B* **53** R14737 (1996).
- [239] F. Ronning, C. Kim, D.L. Feng, D.S. Marshall, A.G. Loeser, L.L. Miller, J.N. Eckstein, I. Bozovic and Z.-X. Shen, *Science* **282** 2067 (1998).
- [240] M. Civelli, M. Capone, S.S. Kancharla, O. Parcollet and G. Kotliar, *Phys. Rev. Lett.* **95** 106402 (2005).
- [241] W. Marshall, *Proc. Roy. Soc. Lond. Ser. A* **232** 48 (1955).
- [242] J. Richter, N.B. Ivanov and K. Retzlaff, *Europhys. Lett.* **25** 545 (1994).
- [243] P.W. Anderson, *Nature Physics* **2** 626 (2006).
- [244] M. Drzazga, A. Kampf, E. Müller-Hartmann and H.A. Wischmann, *Z. Phys. B Condens. Matter* **74** 67 (1989).
- [245] P.W. Anderson, *Phys. Rev.* **112** 1900 (1958).